

Institut für Physik  
der Technischen Universität München  
Lehrstuhl Prof. Dr. W. Götze

# Mode Coupling Theory of the Glass Transition in Binary Mixtures

Thomas Voigtmann

Vollständiger Abdruck der von der Fakultät für Physik der  
Technischen Universität München zur Erlangung des akademischen  
Grades eines

**Doktors der Naturwissenschaften (Dr. rer. nat.)**

genehmigten Dissertation.

Vorsitzender: Univ.-Prof. Dr. W. Petry

Prüfer der Dissertation: 1. Univ.-Prof. Dr. W. Götze  
2. Univ.-Prof. Dr. J. L. van Hemmen

Die Dissertation wurde am 16. Dezember 2002 bei der Technischen  
Universität München eingereicht und durch die Fakultät für Physik  
am 29. Januar 2003 angenommen.



## Acknowledgements

I thank all those who have supported me during the creation of this work.

In particular, let me thank Prof. W. Götze for making possible this thesis, and for introducing me into the field of theoretical physics. He has always left me much space to develop own contributions. In the past years in his group, I had the chance to work on a lot of different things, more than finally fitted into this thesis, which is why I have to refer to the publications listed in the back for them.

Special thanks go to Dr. Thomas Franosch, who has helped a lot with his mathematical intuition, and to Dr. Matthias Fuchs, who contributed a lot in the background.

Thanks also to Matthias Sperl for his discussions and for doubling the number of PhD students in our group.

H. Sprzagala deserves a very special acknowledgement – for just making things work on a lot of occasions.

I thank the experimental groups who provided me with their data files, in particular Prof. W. van Meegen and Dr. S. R. Williams from the RMIT Melbourne, and Dr. E. Bartsch and T. Eckert from the Physical Chemistry group at the U Mainz.

At the late stages of this work, I have benefited from discussions at the Summer School of Theoretical Physics in Les Houches, France. Although this has cost me a lot of time finally, I am indebted to those who made the stay there possible.

This work felt financial support from the DFG through grants No. Go.154/12-1, and by the Leonhard-Lorenz-Stiftung der TU München.

Last but not least, thanks go to my parents for bringing me this far.

And to Claudia-Marion.



# Contents

Acknowledgements	iii
Chapter 1. Introduction	1
Chapter 2. Basic Equations	5
2.1. Mode Coupling Theory	5
2.2. Hydrodynamic Equations	15
Chapter 3. Discussion of MCT Equations	21
3.1. Complete Monotonicity	21
3.2. Asymptotic Expansions	29
3.3. Equations of Structural Relaxation	36
Chapter 4. Binary Hard-Sphere Mixtures	39
4.1. Description of the Model	39
4.2. Glass-Transition Diagram	41
4.3. Glass Form Factors	47
4.4. Dynamics: General Features	61
4.5. Asymptotic Description	72
Chapter 5. Comparison With Experiment	81
5.1. Binary Mixtures: Melting of the Glass	82
5.2. Binary Mixture: Small Size Disparity	97
Appendix A. Numerics	103
A.1. Discretisation of the Equations of Motion	103
A.2. Calculation of Memory Kernels	106
A.3. Calculation of Time-Independent Quantities	106
Appendix B. Perron-Frobenius Theorem	109
Appendix C. Percus-Yevick Structure Factor for Hard Spheres	113

Conclusion	117
List of Figures	121
Publications of the Author	123
Bibliography	125

## CHAPTER 1

# Introduction

Glasses are, from a physicist's point of view, just amorphous solids. Typically they form from so-called "supercooled liquids," *i.e.*, upon cooling or densification when crystallisation can somehow be bypassed. Glasses are solids because they can sustain static shear stress, but on the other hand they lack the spatial long-range order that is characteristic for crystalline solids. From looking at a single snapshot of the system, there is no clear telling whether it is in its glassy or fluid state. One observes no divergence of thermodynamic quantities in the vicinity of the glass transition, thus the liquid-glass transition is not a thermodynamic phase transition discussed in usual statistical physics courses.

Dynamical measurements reveal spectra that are much different from what one would expect in a normal liquid, in that they show a nontrivial behavior over many orders of magnitude in frequency. This is what the term 'glassy dynamics', or more precisely, dynamics in glass-forming liquids refers to. Close to the transition, one observes in the relaxation times and connected quantities a sensitive dependence on the control parameters. For example, in molecular glass formers, a slight change of temperature can increase the viscosity by an order of magnitude.

It is the aim of the mode-coupling theory of the glass transition (MCT) [1-4] to capture this nontrivial glassy dynamics. In particular, the emergence of a discontinuous transition in the long-time limit of the density autocorrelation function, *i.e.*, from liquid-like to solid-like behavior upon smooth changes of the input parameters is explained from a mathematical point of view as a bifurcation transition. Upon approaching the transition, the characteristic relaxation times for the structural relaxation increase and diverge at the transition. In the past, many aspects of the theory have been worked out, in particular so-called universal laws that describe certain aspects of the glassy dynamics that are

independent on the peculiarities of the system under study. A universal glass-transition scenario has been established that involves scaling laws and power-law variations of time scales [5, 6].

But MCT is also able to derive detailed results depending on the specific interactions of a system. The quantitative study of model systems allows one to predict general, while nonuniversal, trends that arise in certain classes of glass formers. Such project has already been carried out for molecular liquids, where general differences in the reorientational relaxation for different angular momenta could be explained [A3, 7].

Thus the main objective of this work is easily formulated: What are general, but nonuniversal effects of the structural-relaxation dynamics that occur upon mixing particles of different sizes?

This work is in a large part stimulated by recent experiments [8] on approximate realisations of binary hard-sphere mixtures as colloidal suspensions. Colloidal suspensions, or short colloids,<sup>1</sup> are dispersions of more-or-less compact particles with sizes in a range of typically 1 nm to 1  $\mu$ m, arranged such that the particles experience Brownian motion in reasonable time scales and that the internal structure of the colloidal particles does not matter for the questions being studied [9]. Many products met in everyday life are colloidal suspensions or related systems, ranging from effluences to cosmetic products [10]. On the other hand, systems with well-characterised particles can be made for laboratory experiments. It is possible to adjust the effective interactions between the suspended particles by changing their surface structure and/or solvent, making them versatile experimentally realisable model systems for atomic matter. Among the most prominent of these ‘model colloids’ is a system originally developed for paints, consisting of spherical poly(methyl methacrylate) (PMMA) spheres coated by a stabilising surface layer, that behave like almost perfect hard spheres [11]. In these hard-sphere(-like) systems, density is the relevant control parameter; and indeed these colloids can be densified in such a way as to form a colloidal glass. Thus they have become a paradigmatic example for the study of glass-transition dynamics and comparison with theory.

---

<sup>1</sup>‘colloid’: from the Greek word κόλλα (glue).

Some general mixing effects in binary mixtures of hard spheres have been found in the cited experiment [8], and we will address them specifically in comparison with our results. Indeed, mixing effects in colloids are also discussed in connection with industrial applications. One example comes from ceramic processing, where the higher ease of glass formation in binary mixtures can be used to prevent cracks during sintering [12, 13].

Another motivation to study glassy dynamics in mixtures comes from the quest of quantitatively explaining measured data. In experiment, both computer-simulated and using colloids, one in most cases somehow has to bypass nucleation in order to reveal the glass transition as the latter occurs in the metastable (with respect to crystallisation) fluid regime. While the theory simply does not consider nucleation, experiments have to retreat to systems where it is sufficiently slow. Contrary to the true one-component hard sphere system, a binary mixture can have a metastable fluid [14]. In computer simulation studies, binary mixtures are therefore quite common [15–18]. The model colloids referred to as “hard spheres” are actually ‘polydisperse’, *i.e.* their sizes are distributed around the mean diameter according to some distribution of typically about 5 to 10% standard deviation. This is an inevitable feature of most colloidal suspensions that arises during their synthesis, and that is even necessary in experimental studies of the glass transition. Again one is led to the discussion of mixtures, as a first discrete approximation to a polydisperse particle size distribution.

MCT for mixtures has been applied before to analyse computer simulation data for a binary soft-sphere mixture [19], a binary Lennard-Jones mixture [20, 21], and to a molecular-dynamics model of metallic melts [22], but mixing effects were not yet addressed explicitly. Overall, these investigations have reported close agreement with the computer-simulation results, lending confidence to the discussion of general mixing effects in glass-forming mixtures using MCT as a framework. Interestingly, even silica melts can in certain aspects be modelled quite well as multi-component ionic mixtures [23–27], and the quantitative agreement of the calculated long-time limits in the partial density autocorrelation functions with the MCT calculation [28] is very encouraging.

The properties of binary hard-sphere mixtures in the limit of large size disparity have been discussed within the MCT framework [29–34]. But

in these cases, the dynamics of the small particles in a sense decouples from the one of the ‘matrix’ of large ones; a limit which is not of interest in the present study. Similarly, for the discussion of charged hard sphere mixtures using MCT, particularly in their low-density regime, we refer to the literature [35–37].

MCT equations for the glass transition in mixtures quite different from the ones to be discussed here have been derived within the framework of nonlinear hydrodynamics [38, 39]. They are very different from the ones analysed here, and we will point out some crucial differences of their implications as compared to ours in the course of the discussion. The connection to experiment was not discussed in Refs. [38, 39].

Mixing effects in binary mixtures were addressed recently using a standard liquid-state mode-coupling approximation, for densities so low that glassy dynamics does not occur [40, 41].

In this work, I will discuss mixing effects that arise as general features from the solutions of the MCT equations and present their comparison with recent experimental results. At first, the stage is set by introducing the necessary equations in Sec. 2. Alongside the work of implementing a suitable algorithm for their solution, we have generalised a series of exact mathematical statements about and an asymptotic expansion of these solutions, which will be presented in Sec. 3. The main qualitative discussion of the sought-after mixing effects, exemplified at binary hard sphere mixtures, is to be found in Sec. 4; a quantitative comparison with experiments on colloidal suspensions follows in Sec. 5. After that, I will summarise and conclude in Sec. 11.

## CHAPTER 2

# Basic Equations

### 1. Mode Coupling Theory

The term mode coupling theory originally applies to a framework going back to Kawasaki [42] (see also the references in Refs. [43, 44]) used to describe the low frequency spectra close to second order phase transitions.

However, the abbreviation MCT now commonly refers to a self-consistent current relaxation theory that is today popular under the name mode coupling theory of the glass transition. We will stick to this use of the term MCT for brevity. The starting point of MCT is the projection operator formalism developed by Zwanzig and Mori (*cf.* [43–45]) together with the idea of approximating resulting memory kernels through factorising averages of products into products of averages.

The main physical effect MCT is thought to describe properly is the so-called cage effect. It comes about since in a dense fluid each particle is situated in a cage formed by its neighbors. It is unlikely for a spontaneous density fluctuation large enough, such that the particle can escape this cage, to occur. Thus large-scale spatial motion typical for a fluid can only happen cooperatively, *i.e.* one of the caging particles has to make way, which can only happen if one of its neighbours moves, and so forth.

On the liquid side of the transition, there forms a so-called backflow pattern one might envisage by alluding to the well-known flow pattern caused by the motion of a large sphere through an incompressible fluid. An intuitive picture was suggested by Rahman [46] in early computer simulations of liquid Argon close to the melting point, where the motion of particles was found to happen along ‘one-dimensional strings’.

If, however, the density is high enough to inhibit these cooperative rearrangements, all particles become trapped in their cages because their neighbours are trapped, and so on. It is this dynamical transition MCT explains as the glass transition.

Derivations of the MCT equations have been given before (see *e.g.* Refs. [3, 4]), and the following section just summarises what is needed further on.

**1.1. General Equations.** Let us first briefly sketch the derivation of the Mori-Zwanzig equation of motion for the particle density and current autocorrelation functions. We restrict ourselves to classical nonreactive multicomponent liquids, where the particles are supposed to be fully described by their positions, momenta, and species label. The variables

$$(2.1) \quad n_\alpha(\vec{q}) = \sum_{i=1}^{N_\alpha} \exp(i\vec{q} \cdot \vec{r}_i^\alpha) / \sqrt{N}$$

are the (spatially Fourier transformed) fluctuating number densities of species  $\alpha$  to wave vector  $\vec{q}$ . The sum runs over all particle positions  $\vec{r}_i^\alpha$  of the particles belonging to species  $\alpha$ ;  $N = \sum_{\alpha=1}^m N_\alpha$  is the total particle number in a system with  $m$  species. We denote the number concentrations by  $x_\alpha = N_\alpha/N$ . The time evolution is given by a Liouville equation,

$$(2.2) \quad n_\alpha(\vec{q}, t) = \exp[i\mathcal{L}t]n_\alpha(\vec{q}),$$

with the Liouville operator  $\mathcal{L}$ ,

$$(2.3) \quad \mathcal{L} = -i \sum_{i,\alpha} \left( \frac{\partial H}{\partial \vec{p}_i^\alpha} \frac{\partial}{\partial \vec{r}_i^\alpha} - \frac{\partial H}{\partial \vec{r}_i^\alpha} \frac{\partial}{\partial \vec{p}_i^\alpha} \right),$$

where  $H$  is the Hamiltonian of the system.<sup>1</sup> There holds the continuity equation expressing particle number conservation,

$$(2.4) \quad \mathcal{L} n_\alpha(\vec{q}) = \vec{q} \cdot \vec{j}_\alpha(\vec{q}),$$

---

<sup>1</sup>We ignore the fact that for hard spheres, possessing a singular potential, a pseudo-Liouville operator has to be defined, since for the derivation of the important MCT equations this is just a technical difficulty [M. Sperl, priv. comm.]

where  $\vec{j}_\alpha(\vec{q})$  are the number currents,

$$(2.5) \quad \vec{j}_\alpha(\vec{q}) = \sum_{i=1}^{N_\alpha} \vec{v}_i^\alpha \exp(i\vec{q} \cdot \vec{r}_i^\alpha) / \sqrt{N}.$$

These shall be split into a longitudinal part,  $j_\alpha^L(\vec{q}) = \hat{e}_{\vec{q}} \vec{j}_\alpha(\vec{q})$ , and a transversal part,  $j_\alpha^T(\vec{q}) = \hat{e}_{\vec{q}}^T \vec{j}_\alpha(\vec{q})$ . Here,  $\hat{e}_{\vec{q}} = \vec{q}/q$  is the unit vector parallel to  $\vec{q}$  (with the abbreviation  $q = |\vec{q}|$ ), and  $\hat{e}_{\vec{q}}^T$  is a unit vector perpendicular to it. Because of isotropy, it suffices to consider one of the two linearly independent transversal parts. Only the longitudinal current couples to density fluctuations.

The simplest statistical information on structural relaxation that can be extracted by experiment is given through correlation functions. One defines on the space of dynamical variables the so-called Kubo scalar product,  $\langle \cdot | \cdot \rangle$ , as  $\langle A | B \rangle = \langle \delta A^* \delta B \rangle$ , where  $\delta A = A - \langle A \rangle$ , and  $\langle \dots \rangle$  denotes canonical averages. With this, the matrix of density correlation functions is formed,

$$(2.6) \quad \Phi_{\alpha\beta}(q, t) = \langle n_\alpha(\vec{q}, t) | n_\beta(\vec{q}) \rangle.$$

Since it is the spatial Fourier transform of a function that is real, translational invariant and isotropic, it is itself real and depends on  $\vec{q}$  only through its magnitude  $q$ . We use bold symbols to denote matrices in the species labels, supplied with the usual matrix operators. The matrix  $\Phi(q, t)$  is symmetric in its species indices as a consequence of time-inversion symmetry in Newtonian dynamics. The density correlation functions are important in describing the dynamics of a system since linear combinations of the partial correlators are directly accessible in many scattering experiments, such as neutron scattering or dynamic light-scattering in colloids.

The amorphous solid can be distinguished from the liquid by looking at the long-time limit of the density correlators, denoted by

$$(2.7) \quad \mathbf{F}(q) = \lim_{t \rightarrow \infty} \Phi(q, t).$$

It vanishes in the liquid, while in the glass it is nonvanishing.  $\mathbf{F}(q)$  is called the ‘glass form factor’ or, in the literature, ‘nonergodicity parameter’.<sup>2</sup> It is in the one-component system the Debye-Waller factor and is amenable to experimental determination.

A general idea behind the formalism developed by Zwanzig and Mori is to interpret a correlation function  $C_{AB}(t) = \langle A(t)|B \rangle$  as a projection of  $A(t)$  onto  $B$ . In precise terms, one defines a projection operator  $\mathcal{P} = \sum_{\{A\}} |A\rangle\langle A|A\rangle^{-1}\langle A|$  together with the orthogonal projection  $\mathcal{Q} = 1 - \mathcal{P}$ , satisfying  $\mathcal{P}^2 = \mathcal{P}$  and  $\mathcal{Q}\mathcal{P} = 0$ . Using these operators, one can achieve an exact reformulation of the Liouville equation (*cf.* [43] for a detailed calculation). The choice of the distinguished variables to include in the set  $\{A\}$  used for the projection operator is guided by physical intuition.

The projection operator formalism is conveniently displayed using Laplace transformed quantities. We use the convention  $f(z) = \text{LT}[f(t)](z)$ ,

$$(2.8) \quad f(z) = i \int_0^\infty e^{izt} f(t) dt; \quad z \in \mathbb{C}, \quad \text{Im } z > 0,$$

for complex frequencies  $z$  in the upper half plane, chosen such that the limit of  $z$  approaching the real line defines the spectrum,  $f(z = \omega + i0) = f'(\omega) + i f''(\omega)$ . A nonvanishing long-time limit,  $f(t \rightarrow \infty) = f_\infty$ , leads to a  $1/z$  pole for  $z \rightarrow 0$ ,  $f(z) \rightarrow -f_\infty/z$ .

To get the equation of motion MCT builds upon, one projects onto the number densities and the corresponding currents. Since only the longitudinal parts of the currents couple to the densities, the projectors reads projector reads

$$(2.9) \quad \mathcal{P} = \sum_{\alpha\beta} |n_\alpha(\vec{q})\rangle\langle n(\vec{q})|n(\vec{q})\rangle_{\alpha\beta}^{-1}\langle n_\beta(\vec{q})| + \sum_{\alpha\beta} |j_\alpha^L(\vec{q})\rangle j_\beta^L(\vec{q})_{\alpha\beta}^{-1}\langle j_\beta^L(\vec{q})|.$$

The matrices  $\mathbf{S}(q)$  and  $\mathbf{J}$  are the time-zero normalisations,

$$(2.10a) \quad S_{\alpha\beta}(q) = \langle n_\alpha(\vec{q})|n_\beta(\vec{q})\rangle,$$

$$(2.10b) \quad J_{\alpha\beta} = \langle j_\alpha^L(\vec{q})|j_\beta^L(\vec{q})\rangle = \langle j_\alpha^T(\vec{q})|j_\beta^T(\vec{q})\rangle = \delta_{\alpha\beta} x_\alpha v_{\text{th},\alpha}^2,$$

---

<sup>2</sup>Experiments suggest that indeed the glass is a nonergodic state. Strictly speaking a nonvanishing  $\mathbf{F}(q)$  does not indicate that the system is truly nonergodic, rather it becomes nonmixing [47].

where  $v_{\text{th},\alpha} = \sqrt{k_{\text{B}}T/m_{\alpha}}$  is the thermal velocity of a particle of species  $\alpha$  with mass  $m_{\alpha}$ .  $\mathbf{S}(q)$  is the matrix of partial structure factors [48]. It is connected to the matrix of so-called direct correlation functions,  $\mathbf{c}(q)$  by virtue of the Ornstein-Zernike equation [44],

$$(2.11) \quad S_{\alpha\beta}^{-1}(q) = \delta_{\alpha\beta}/x_{\alpha} - nc_{\alpha\beta}(q).$$

Inserting the above projection into the Liouville equations, one arrives after some straightforward algebra [43] at a matrix equation for the corresponding correlation functions,

$$(2.12) \quad \begin{pmatrix} z\mathbf{1} & q\mathbf{1} \\ q\mathbf{J}\mathbf{S}^{-1}(q) & z\mathbf{1} + \mathbf{K}^{jj,\text{L}}(q, z) \end{pmatrix} \begin{pmatrix} \Phi(q, z) & \mathbf{C}^{nj}(q, z) \\ \mathbf{C}^{jn}(q, z) & \Phi^{\text{L}}(q, z) \end{pmatrix} \\ = - \begin{pmatrix} \mathbf{S}(q) & \\ & \mathbf{J} \end{pmatrix},$$

Here we have introduced the notation  $C_{\alpha\beta}^{jn}(q, z) = C_{\alpha\beta}^{nj}(q, z) = \langle j_{\alpha}(\vec{q}) | \times \mathcal{R}(z) n_{\beta}(\vec{q}) \rangle$  and  $\Phi_{\alpha\beta}^x(q, z) = \langle j_{\alpha}^x(\vec{q}) | \mathcal{R}(z) j_{\beta}^x(\vec{q}) \rangle$  with  $x = \text{L}, \text{T}$ .  $\mathcal{R}(z) = [\mathcal{L} - z]^{-1}$  gives the dynamical evolution in the Laplace domain. The matrix  $\mathbf{K}(q, z)$  appearing in the above expression is the so-called memory kernel of (longitudinal) fluctuating forces, for which one gets by virtue of the projection operator formalism an exact microscopic expressions. This can, however, in general not be evaluated and thus one is forced to introduce approximations.

**1.2. Mode Coupling Approximation.** The so-called fluctuating longitudinal current relaxation kernel reads

$$(2.13) \quad K_{\alpha\beta}^{jj,\text{L}}(q, z) = \langle \mathcal{Q} \mathcal{L} j_{\alpha}^{\text{L}}(\vec{q}) | \mathcal{R}'(z) \mathcal{Q} \mathcal{L} j_{\beta}^{\text{L}}(\vec{q}) \rangle / (x_{\beta} v_{\text{th},\beta}^2),$$

where  $\mathcal{R}'(z) = [\mathcal{Q} \mathcal{L} \mathcal{Q} - z]^{-1}$  is the so-called projected resolvent. MCT provides an approximation for that part of the relaxation kernel which is the dominant one close to the glass transition, *i.e.* the one that develops a  $1/z$  pole. There are other contributions to  $K_{\alpha\beta}^{jj,\text{L}}$  and similar memory kernels that remain regular in the limit  $z \rightarrow 0$ ; they have to be split off before applying the mode-coupling approximation and treated separately. In lack of a microscopic expression for them, we will silently drop them.

The physical picture of dense liquids sketched above suggests that the fluctuating forces governing the density fluctuations in turn arise through

products of density fluctuations (the caging of particles stems from other caged particles). Thus one should be able to find a reasonable approximation of  $\mathbf{K}^{jj}$  in terms of products of  $\Phi$ . Technically, one introduces a projector onto pair modes [3],

$$(2.14) \quad \mathcal{P}_2 = \sum_{\substack{\alpha\beta\alpha'\beta' \\ \vec{k} > \vec{p}, \vec{k}' > \vec{p}'}} |n_\alpha(\vec{k})n_\beta(\vec{p})\rangle g_{\alpha\beta}^{\alpha'\beta'}(\vec{k}\vec{p}, \vec{k}'\vec{p}') \langle n_{\alpha'}(\vec{k}')n_{\beta'}(\vec{p}')|,$$

with some appropriate normalisation  $g$  and some order relation  $\vec{k} > \vec{p}$  to avoid double counting. As a first step, one gets

$$(2.15) \quad K_{\alpha\beta}^{jj,L}(q, z) \approx \sum_{\substack{\alpha'\alpha''\beta'\beta'' \\ \vec{k} > \vec{p}, \vec{k}' > \vec{p}'}} \mathcal{V}_{\alpha\alpha'\alpha''}(\vec{q}, \vec{k}, \vec{p}) \langle \delta n_{\alpha'}(\vec{k})n_{\alpha''}(\vec{p}) \rangle \times \\ \times |\mathcal{R}'(z)\delta n_{\beta'}(\vec{k}')\delta n_{\beta''}(\vec{p}')\rangle \mathcal{V}_{\beta'\beta''}^+(\vec{q}, \vec{k}', \vec{p}') / (x_\beta m_\alpha k_B T),$$

with the ‘vertex’

$$(2.16) \quad \mathcal{V}_{\alpha\beta\gamma}(\vec{q}\vec{k}\vec{p}) = \sum_{\beta'\gamma'\vec{k}'\vec{p}'} \langle \mathcal{Q} f_\alpha(\vec{q})|\delta n_{\beta'}(\vec{k}')\delta n_{\gamma'}(\vec{p}')\rangle g_{\beta'\gamma'}^{\beta\gamma}(\vec{k}'\vec{p}', \vec{k}\vec{p}),$$

with the longitudinal fluctuating force  $f_\alpha(\vec{q}) = m_\alpha \mathcal{L} j_\alpha(\vec{q})$ . The next step in the mode-coupling approximation consists of factorising the four-point correlations in the above expressions into products of two-point correlation functions. For the time-dependent term, the approximation involves replacing the reduced resolvent with the original one in the time domain to get

$$(2.17) \quad \langle \delta n_{\alpha'}(\vec{k})\delta n_{\alpha''}(\vec{p})|\mathcal{R}'(t)\delta n_{\beta'}(\vec{k}')\delta n_{\beta''}(\vec{p}')\rangle / N \\ \approx \langle n_{\alpha'}(\vec{k})|\mathcal{R}(t)n_{\beta'}(\vec{k}')\rangle \langle n_{\alpha''}(\vec{p})|\mathcal{R}(t)n_{\beta''}(\vec{p}')\rangle \\ = \Phi_{\alpha'\beta'}(k, t)\Phi_{\alpha''\beta''}(p, t)\delta_{\vec{k}\vec{k}'}\delta_{\vec{p}\vec{p}'}.$$

From this, the approximated normalisation  $g$  is directly obtained for  $t \rightarrow 0$ , and thus the vertex in Eq. (2.16) can be calculated.

Putting things together, Eq. (2.12) can be solved for the density correlators,

(2.18a)

$$\Phi(q, z) = - \left[ z\mathbf{S}(q)^{-1} - \mathbf{S}(q)^{-1} [z\mathbf{J}(q)^{-1} + \mathbf{M}(q, z)]^{-1} \mathbf{S}(q)^{-1} \right]^{-1},$$

where we have set  $\mathbf{J}(q) = q^2 \mathbf{J}$  and  $\mathbf{M}(q, z) = \mathbf{J}(q)^{-1} \mathbf{K}^{jj, L}(q, z)$ . This exact expression is closed by approximating in the time-domain the memory kernel matrix  $\mathbf{M}(q, t)$  as a bilinear functional of the correlators,

$$(2.18b) \quad \mathbf{M}(q, t) = \mathcal{F}[\Phi(t)](q),$$

given as

$$(2.18c) \quad \mathcal{F}_{\alpha\beta}[\mathbf{F}](q) = \frac{1}{2q^2} \frac{n}{x_\alpha x_\beta} \sum_{\substack{\alpha' \beta' \\ \alpha'' \beta''}} \int \frac{d^3 k}{(2\pi)^3} V_{\alpha\alpha'\alpha''}(\vec{q}\vec{k}\vec{p}) F_{\alpha'\beta'}(k) \times \\ \times F_{\alpha''\beta''}(p) V_{\beta\beta'\beta''}(\vec{q}\vec{k}\vec{p}).$$

Here,  $\vec{p} = \vec{q} - \vec{k}$  throughout, and we have replaced  $\sum_{\vec{k}}$  by  $(V/(2\pi)^3) \int d^3 k$ . The final form of the vertices entering the above expression then is

$$(2.18d) \quad V_{\alpha\beta\gamma}(\vec{q}\vec{k}\vec{p}) = (\hat{e}_{\vec{q}\vec{k}}) c_{\alpha\beta}(k) \delta_{\alpha\gamma} + (\hat{e}_{\vec{q}\vec{p}}) c_{\alpha\gamma}(p) \delta_{\alpha\beta} + qn x_\alpha c_{\alpha\beta\gamma}^{(3)}(\vec{q}, \vec{k}),$$

where  $c^{(3)}$  denotes the static triplet correlation function [19].

The vertices, Eq. (2.18d), are seen to be given in terms of static correlation functions only; thus MCT is able to make quantitative predictions of a glass-forming liquid's dynamics if these static quantities are known. In this way, the static correlation functions serve as input for the theory. Apart from this, the above Eqs. (2.18) are closed. Note that the dependence on the particle mass ratios has dropped out in Eqs. (2.18c) and (2.18d). As a consequence, the calculated glass-transition densities will not depend on the particles' inertia parameters, as one expects for equilibrium properties of a classical system. Computer simulation results for the glass-transition density of binary soft-sphere mixtures are in agreement with this [16]. The MCT equations derived recently by Harbola and Das [38] on the contrary show an explicit mass-ratio dependence of the glass-transition densities.

Literature on structure factor theory is vast (*cf.* Ref. [49] for an overview), but most often concerned with predicting correctly thermodynamic quantities, *i.e.* the  $q \rightarrow 0$  limit. Also, not much is known about the accuracy of the approximations used at high densities. Furthermore, the MCT vertex requires knowledge of static triplet correlations which is

often lacking entirely. On the other hand, the MCT glass-transition scenario is found to be topologically stable,<sup>3</sup> thus the qualitative features we are going to discuss are not affected by the quantitative correctness of the input.

A particular technical approximation we will use throughout this work is to drop the  $c^{(3)}$  term in Eq. (2.18d); this amounts to approximating the static triplet correlations in terms of two-particle quantities using the so-called convolution approximation [50]. Sciortino and Kob [28] have determined  $c^{(3)}$  from molecular dynamics simulations and checked that for the evaluation of Eq. (2.18d) in a binary Lennard-Jones mixture, this term is not important. We thus anticipate the same for binary hard-core mixtures.

**1.3. Colloidal Dynamics.** The above derivation proceeded with  $\mathcal{L}$  denoting the usual Liouville operator for Newtonian dynamics. For colloids, governed by Brownian dynamics, one generally takes the time evolution to be described by the (adjoint) Smoluchowski operator  $\mathcal{S}$  [51, 52],  $n_\alpha(\vec{q}, t) = \exp[i\mathcal{S}t]n_\alpha(\vec{q})$ ,

$$(2.19) \quad \mathcal{S} = -i \sum_{ij} \left[ \frac{\partial}{\partial \vec{r}_i} - \beta \frac{\partial V}{\partial \vec{r}_i} \right] D_{ij}(\{\vec{r}\}) \frac{\partial}{\partial \vec{r}_j}$$

(dropping particle species indices for the moment). Here,  $\mathbf{D}$  is called the many-particle diffusion tensor. It is a highly complicated function of all particle coordinates; its complicated structure comes about due to non-pairwise additive interaction effects between the colloidal particles caused by the suspending medium, the so-called hydrodynamic interactions (HI). We will neglect them in this work, in which case  $\mathbf{D}$  becomes independent on the particle coordinates. Generally,  $\mathbf{D}$  is assumed to be a positive definite matrix (for all possible combinations of particle positions). With this, one finds by direct calculation for any dynamical variables  $A$  and  $B$  [51],

$$(2.20) \quad \langle A | i\mathcal{S} B \rangle = - \left\langle \frac{\partial A}{\partial \vec{r}} \middle| \mathbf{D} \frac{\partial B}{\partial \vec{r}} \right\rangle$$

(to be read in matrix notation). This proves that  $i\mathcal{S}$  is a negative definite operator, a fact that is of central importance for the discussion of

---

<sup>3</sup>This is an implication of the mathematical properties discussed in Sec. 3.

Sec. 3.1. The validity of the Smoluchowski equation for colloidal dynamics can be questioned for short time scales (*cf.* Ref. [51]), but it is generally believed to be correct on long time scales. The crossover is given by the ‘Brownian’ time it takes a colloidal particle to relax its momentum to equilibrium. For typical hard-sphere like colloids, this time is about 5 or more orders of magnitude smaller than the time scale relevant for the diffusional motion. Thus the requirement of separated time scales entering the Smoluchowski description should be well fulfilled. Only for highly charged colloids, doubt has been cast upon the applicability of the Smoluchowski equation [53].

Since we are in this work mainly concerned with colloidal suspensions, let us write down the equations of motion applying to such systems where the short-time dynamics can be regarded as Brownian. It is possible to derive equations analogous to the ones given above [54, 55], but additional care has to be taken not to mistreat the  $1/z$  pole of the glass transition. One gets the analogue of Eq. (2.18a),

$$(2.21) \quad \Phi(q, z) = - \left[ z\mathbf{S}(q)^{-1} - \mathbf{S}(q)^{-1} [i\boldsymbol{\tau}(q) + \mathbf{M}(q, z)]^{-1} \mathbf{S}(q)^{-1} \right]^{-1}.$$

The matrix  $\boldsymbol{\tau}(q)$  characterizes the short-time decay through  $\Phi(q, t) = \mathbf{S}(q) - \boldsymbol{\tau}(q)^{-1}t + \mathcal{O}(t^2)$  and is assumed to be real and positive definite. It is connected to the short-time collective diffusion constants  $D_\alpha^0$  by  $\tau_{\alpha\beta} = 1/(q^2 D_\alpha^0) \delta_{\alpha\beta}$ . The symmetry of the correlation function with respect to interchanging species indices now is no longer obvious from time-inversion parity, but has to be proven separately [51]. For the memory kernel  $\mathbf{M}(q, z)$ , the MCT approximations as above lead to the same result as in the Newtonian case, Eqs. (2.18b–2.18d).

**1.4. Coupled Quantities.** Analogously to the one for  $\mathbf{M}(q, z)$ , one can derive an approximation for the memory kernel of the transverse currents,  $\mathbf{M}^T(q, t) = \mathcal{F}^T[\Phi(t)](q)$ . Similar to above one gets

$$(2.22a) \quad \mathcal{F}_{\alpha\beta}^T[\mathbf{F}](q) = \frac{1}{2q^2} \frac{n}{x_\alpha x_\beta} \sum_{\substack{\alpha'\beta' \\ \alpha''\beta''}} \int \frac{d^3k}{(2\pi)^3} V_{\alpha\alpha'\alpha''}^T(\vec{q}\vec{k}\vec{p}) F_{\alpha'\beta'}(k) \times \\ \times F_{\alpha''\beta''}(p) V_{\beta\beta'\beta''}^T(\vec{q}\vec{k}\vec{p}).$$

the only difference being the orthogonal projection in the vertex,

$$(2.22b) \quad V_{\alpha\beta\gamma}^T(\vec{q}\vec{k}\vec{p}) = (\hat{e}_{\vec{q}}^T \vec{k}) c_{\alpha\beta}(k) \delta_{\alpha\gamma} + (\hat{e}_{\vec{q}}^T \vec{p}) c_{\alpha\gamma}(p) \delta_{\alpha\beta}.$$

Note that in this expression, the triplet correlation function drops out exactly. Given the density correlators  $\Phi(q, t)$  calculated from Eqs. (2.18), Eqs. (2.22) can be readily evaluated.

Another quantity of interest is the self-motion of a tracer particle, quantified by the correlator  $\Phi_s(q, t) = \langle n_s(\vec{q}, t) | n_s(\vec{q}) \rangle$ , where  $n_s(\vec{q}, t) = \exp[i\vec{q}\vec{r}_s(t)]$  is the one-particle density of a tagged particle. Again, the Mori-Zwanzig projector formalism gives a memory equation which reads, for Brownian dynamics,

$$(2.23a) \quad \Phi_s(q, z) = -1 / \left[ z - q^2 / [(i/D_s^0) + q^2 M_s(q, z)] \right],$$

with the short-time diffusion constant  $D_s^0$ . The MCT approximation for  $M_s(q, t)$  can be inferred from Eq. (2.18c) by considering an  $(m+1)$ -component mixture in the limit of one concentration going to zero,  $x_s \rightarrow 0$ . Keeping only the dominant terms in the system size, one gets

$$(2.23b) \quad M_s(q, t) = \frac{n}{q^2} \sum'_{\alpha\beta} \int \frac{d^3k}{(2\pi)^3} V_{s,\alpha\beta}(\vec{q}\vec{k}) \Phi_{\alpha\beta}(k, t) \Phi_s(p, t),$$

with the tagged-particle vertex

$$(2.23c) \quad V_{s,\alpha\beta}(\vec{q}\vec{k}) = (\hat{e}_{\vec{q}}^T \vec{k}) c_{s\alpha}(k) c_{s\beta}(k).$$

The prime at the sum indicates that summation over  $\alpha = s$  and  $\beta = s$  is omitted. The tagged-particle correlator is in the limit  $q \rightarrow 0$  connected to the mean-squared displacement,  $\delta r^2(t) = \langle |\vec{r}(t) - \vec{r}(0)|^2 \rangle$ , by  $\Phi_s(q, t) = 1 - q^2 \delta r^2(t) / 6 + \mathcal{O}(q^4)$  [44]. For a Brownian particle, it is determined through

$$(2.24a) \quad \delta r^2(t) + D_0^s \int_0^t \hat{M}_s(t-t') \delta r^2(t') dt' = 6D_0^s t,$$

with  $\hat{M}_s(t) = \lim_{q \rightarrow 0} q^2 M_s(q, t)$ ,

$$(2.24b) \quad \hat{M}_s(t) = \frac{1}{6\pi^2} \sum'_{\alpha\beta} \int_0^\infty k^4 dk c_{s\alpha}(k) c_{s\beta}(k) c_{s\beta}(k) \Phi_{\alpha\beta}(k, t) \Phi_s(k, t).$$

We will in particular discuss the long-time limit of the above equation, which gives in the glass the localisation length  $r_s$  of a particle,

$$(2.25) \quad r_s = \sqrt{1 / \lim_{t \rightarrow 0} \hat{M}_s(t)}.$$

Since  $M_s(q, t)$  is given as a functional of the  $\Phi(q, t)$ , one calculates  $r_s$  directly from the glass form factors  $F(q)$ .

**1.5. Remarks.** In the derivation of the MCT equations, short-time contributions to the memory kernel arising from binary collisions were neglected. It turns out to be an involved procedure to include them correctly. A subtraction procedure has been proposed [20, 21] since the inclusion of a regular short-time memory kernel in addition to the MCT one results in a double-counting problem. We will refrain from doing so, since a study of the mathematical properties of the MCT equations brings out that the subtraction procedure possibly destroys important features of the memory kernel. The glass-transition scenarios we are interested in happen on much longer time scales and are thus unaffected by the improper treatment of short-time effects.

A few remarks concerning the numerical solution of Eqs. (2.18) or (2.21), (2.22), and (2.23) might be in order.

Strictly speaking, we are discussing wave-vector discretised models of the MCT equations of motion, requiring  $q$  to be elements of some grid with  $M$  points, implying some cutoff wave vector  $q^*$ . A numerical procedure for solving the MCT equations of motion has evolved during the last ten or so years, grounding on the work of Fuchs, Götze, Hofacker and Latz [56]. The resulting method is a straightforward but efficient direct integration of the equations of motion in the time-domain. Since the solutions are required over many decades of variation in the time  $t$ , a specially adapted algorithm is used. Appendix A is devoted to an overview of the numerical methods employed in this work.

## 2. Hydrodynamic Equations

For completeness, some equations from the hydrodynamic theory of mixtures that are needed later on shall be explained in this section. The underlying ideas are of course to be found in standard textbooks

[44, 57], but usually, the discussion is based on phenomenological constitutive equations, and the Green-Kubo relations connecting the transport coefficients to microscopic correlation functions are only mentioned for the one-component case [43, 44].

In the projection-operator formulation of the hydrodynamic equations, one is guided in the choice of the set of variables one wants to single out by the macroscopic conservation laws of the system. As the particle numbers are conserved, one as above chooses  $n_\alpha(\vec{q})$  to be in that set, but due to momentum transfer between the species, it is inconvenient to work with the number currents  $\vec{j}_\alpha(\vec{q})$  here. Instead, one chooses the total momentum current,

$$(2.26) \quad \vec{J}(\vec{q}) = \sum_{\alpha} m_{\alpha} \vec{j}_{\alpha}(\vec{q}).$$

The energy conservation law gives rise to the hydrodynamic heat modes, but we shall not be concerned with them here. Their inclusion requires one to include in the set of variables the enthalpy density  $H(\vec{q})$ , which is the energy density orthogonalised with respect to the particle densities using the Kubo scalar product. For a discussion of the resulting equations, we refer the reader to Ref. [58]. Götze and Latz [59] have argued that for a description of supercooled liquids, a better choice of variable instead of  $H(\vec{q})$  is to take only the kinetic part of the energy density  $\mathcal{E}(\vec{q})$ ; this program has been carried out in Ref. [59] for a one-component system, but the generalisation to mixtures is straightforward (*cf.* [60]). Thus one arrives at the hydrodynamic projection operator

$$(2.27) \quad \mathcal{P}_{\text{HD}} = \mathcal{P}_n + \sum_{x=L,T} |J^x(\vec{q})\rangle \langle J^x(\vec{q})| J^x(\vec{q})^{-1} \langle J^x(\vec{q})| \\ + |T(\vec{q})\rangle \langle T(\vec{q})| T(\vec{q})^{-1} \langle T(\vec{q})|,$$

where, as above,

$$(2.28) \quad \mathcal{P}_n = \sum_{\alpha\beta} |n_{\alpha}(\vec{q})\rangle \langle n(\vec{q})| n_{\alpha\beta}^{-1} \langle n_{\beta}(\vec{q})|$$

is the projector onto the number densities, and the temperature fluctuations are defined as  $T(\vec{q}) = (1 - \mathcal{P}_n)\mathcal{E}(\vec{q})$  [59]. As usual, the vectorial current has been split into a part longitudinal and transversal to  $\vec{q}$ .

The static quantities appearing in the resulting equations can in the limit  $q \rightarrow 0$  be connected to thermodynamic derivatives. Hereby it is

convenient to work in the grand-canonical ensemble. Note that since for any variable  $\hat{a}$ ,  $\partial\langle\hat{a}\rangle/\partial\mu_\alpha = (N/k_B T)\langle\hat{a}|\hat{N}_\alpha\rangle$ , where  $\hat{N}_\alpha = N_\alpha(\vec{q} = 0)$  is the particle number operator and  $\mu_\alpha$  denotes the corresponding chemical potential, we immediately get the connection for the static structure factor by setting  $\hat{a} = \hat{N}_\beta$ :

$$(2.29) \quad \left. \frac{\partial\mu_\alpha}{\partial N_\beta} \right|_{T, V, \{N_{\bar{\beta}}\}} = \frac{k_B T}{N} S_{\alpha\beta}^{-1}(q=0),$$

where  $\{N_{\bar{\beta}}\}$  denotes the set of all  $N_\gamma$  with  $\gamma \neq \beta$ . In particular, one sees that stability of the system with respect to density fluctuations requires the above matrix to be positive definite; in general,  $\mathbf{S}(q) \succeq 0$ , where  $\succeq$  denotes positive definiteness:  $\sum_{\alpha\beta} y_\alpha^* S_{\alpha\beta} y_\beta \geq 0$  for all complex  $y_\alpha$ . Passivity, *i.e.* thermodynamic stability, also requires the long-time limits of the density correlations in the glass to be positive definite,  $\mathbf{F}(q) \succeq 0$ .

The macroscopic mechanical stability of the system is quantified by the elastic moduli. Rewriting the thermodynamic derivative in the above equation to one at fixed pressure  $p$  instead of fixed volume, one gets a relation involving the isothermal compressibility  $\kappa_T = 1/M_L^0$  [44],

$$(2.30) \quad M_L^0 = (nk_B T) \sum_{\alpha\beta} x_{\alpha\beta} x_\alpha S_{\alpha\beta}^{-1}(q=0) x_\beta = nk_B T \left( 1 - n \sum_{\alpha\beta} x_\alpha c_{\alpha\beta}(0) x_\beta \right),$$

the latter due to Eq. (2.11).  $M_L^0$  is the longitudinal elastic modulus the liquid exhibits.

The viscosities of the liquid are given in terms of correlation functions by the Green-Kubo relations involving the total mass current [58]; the longitudinal viscosity is

$$(2.31) \quad \eta_L = \lim_{z \rightarrow 0} \lim_{q \rightarrow 0} \frac{1}{q^2} \frac{n}{k_B T} \langle \mathcal{Q}_{\text{HD}} \mathcal{L} J^L(\vec{q}) | \mathcal{R} \mathcal{Q}_{\text{HD}} \mathcal{L} J^L(\vec{q}) \rangle,$$

with the projector orthogonal to the hydrodynamic variables  $\mathcal{Q}_{\text{HD}} = 1 - \mathcal{P}_{\text{HD}}$ . Similarly, the shear viscosity reads

$$(2.32) \quad \eta = \lim_{z \rightarrow 0} \lim_{q \rightarrow 0} \frac{1}{q^2} \frac{n}{k_B T} \langle \mathcal{Q}_{\text{HD}} \mathcal{L} J^T(\vec{q}) | \mathcal{R} \mathcal{Q}_{\text{HD}} \mathcal{L} J^T(\vec{q}) \rangle.$$

To evaluate these expressions within MCT, we need to reformulate these relations to include the MCT projectors  $\mathcal{P}$  and  $\mathcal{Q}$ . This is easily done by noting that, neglecting temperature fluctuations, the difference does not matter in Eqs. (2.31) and (2.32) since  $\langle \vec{J}(\vec{q}) | \mathcal{L} \vec{J}(\vec{q}) \rangle = 0 =$

$\langle \vec{J}(\vec{q}) | \mathcal{L} \vec{J}(\vec{q}) \rangle$ . Furthermore, in the limit  $q \rightarrow 0$  for a conserved quantity, one can replace  $\mathcal{R}(z)$  by the projected resolvent  $\mathcal{R}'(z)$  [59]. Recalling Eqs. (2.18) and (2.22), one gets

$$(2.33) \quad \eta(z) = (nk_{\text{B}}T) \lim_{q \rightarrow 0} \sum_{\alpha\beta} x_{\alpha} M_{\alpha\beta}^{\text{T}}(q, z) x_{\beta},$$

the generalised frequency-dependent shear viscosity; an analogous expression for the longitudinal viscosity holds.

At the glass transition, the correlation functions coupling to the density develop a nontrivial long-time limit, which implies a  $1/z$  pole for small frequencies also in the frequency-dependent viscosities. Hence, an additional contribution in the longitudinal modulus  $M_{\text{L}}$  coming from the arrest of the structure occurs in the glass,  $M_{\text{L}} = M_{\text{L}}^0 + \delta M_{\text{L}}$ , where second term is given by

$$(2.34) \quad \delta M_{\text{L}} = (nk_{\text{B}}T) \lim_{q \rightarrow 0} \sum_{\alpha\beta} x_{\alpha} \mathcal{F}_{\alpha\beta}[\mathbf{F}, \mathbf{F}](q) x_{\beta}.$$

The glass is also, as opposed to the liquid, characterised by a finite shear modulus

$$(2.35) \quad \delta M_{\text{T}} = (nk_{\text{B}}T) \lim_{q \rightarrow 0} \sum_{\alpha\beta} x_{\alpha} \mathcal{F}_{\alpha\beta}^{\text{T}}[\mathbf{F}, \mathbf{F}](q) x_{\beta}.$$

Inserting Eq. (2.18c) into Eq. (2.34) and Eq. (2.22a) into Eq. (2.35) or (2.33), the  $q \rightarrow 0$  limit can be performed analytically. Each element of  $M_{\alpha\beta}(q, t)$  diverges like  $1/q^2$ , but noting

$$(2.36) \quad \sum_{\alpha} V_{\alpha\beta\gamma}(\vec{q}\vec{k}\vec{p}) = (q/k) \left( kc_{\beta\gamma}(k) + (\hat{e}_{\vec{q}}\vec{k})^2 c'_{\beta\gamma}(k) \right) + \mathcal{O}(q^2)$$

with  $c'_{\alpha\beta}(k) = \partial_k c_{\alpha\beta}(k)$ , one derives  $\sum_{\beta} M_{\alpha\beta}(q, t) x_{\beta} = \mathcal{O}(q^0)$ . Explicitly, the result reads

(2.37a)

$$\delta M_{\text{L}}/(nk_{\text{B}}T) = \sum_{\alpha'\alpha''\beta'\beta''} \int_0^{\infty} dk V_{\alpha'\alpha''\beta'\beta''}(k) F_{\alpha'\beta'}(k, t) F_{\alpha''\beta''}(k, t),$$

with the glass form factor  $\mathbf{F}(q)$  and

$$(2.37b) \quad V_{\alpha'\alpha''\beta'\beta''}(k) = \frac{nk^2}{4\pi^2} \times \\ \times \left( c_{\alpha'\alpha''}(k) c_{\beta'\beta''}(k) + \frac{2}{3} k c'_{\alpha'\alpha''}(k) c_{\beta'\beta''}(k) + \frac{1}{3} k c'_{\alpha'\alpha''}(k) k c'_{\beta'\beta''}(k) \right).$$

The expression for the shear modulus in the glass is quite similar, but involves only a  $(c')^2$  term in the vertex,

$$(2.38) \quad \delta M_T / (nk_B T) = \frac{n}{60\pi^2} \int_0^\infty dk k^4 \text{tr}[(c' \cdot \mathbf{F})^2](k),$$

or, for the shear viscosity discussed later on

$$(2.39) \quad \eta / (nk_B T) = \frac{n}{60\pi^2} \int_0^\infty dt \int_0^\infty dk k^4 \text{tr}[(c' \cdot \Phi)^2](k, t).$$

Equations (2.37), (2.38) and (2.39) are used for the numerical calculation of the moduli and viscosities.

For colloidal suspensions, the viscosities are composed of a part solely due to the colloidal particles, and terms that stem from interaction with the solvent and a ‘background’ solvent viscosity. The latter is usually neglected in theoretical work by considering only ‘osmotic’ compression of the colloidal particles. Neglecting further the hydrodynamic interactions, one arrives at the equivalent Green-Kubo relations as for molecular systems [61]. The quantities are then sometimes referred to as the ‘relative’ viscosities that are independent on effects of the suspending medium. We will in the following use the term ‘viscosity’ to implicitly mean this relative viscosity for colloidal suspensions.



## Discussion of MCT Equations

### 1. Complete Monotonicity

We shall discuss now some mathematical properties of the MCT solutions that could be proven to hold for Brownian short-time dynamics. There, one has a number of properties of correlation functions that are direct consequences of the time-evolution operator  $\mathcal{L}$  of the system, which is here taken to be the Smoluchowski, or, more generally, any negative definite operator  $i\mathcal{S}$ .

In such cases, one has the spectral decomposition  $\exp[i\mathcal{S}t] = \int e^{-\gamma t} dP_\gamma$  with eigenvalues  $\gamma \geq 0$ , and  $P_\gamma$  denoting the projector onto the corresponding linear subspace. In other words, one can represent  $\Phi(q, t)$  as

$$(3.1) \quad \Phi_{\alpha\beta}(q, t) = \int e^{-\gamma t} da_{\alpha\beta, q}(\gamma),$$

where  $a$  is a measure that is concentrated on the nonnegative real axis. It is symmetric in  $\alpha, \beta$ , and positive,  $\mathbf{d}a_q(\gamma) \succeq 0$ , in the sense that for any set of complex numbers  $y_\alpha$ , the measure  $y_\alpha^* da_{\alpha\beta, q}(\gamma) y_\beta$  is positive. A function having this property is called completely monotone. Due to the Bernstein theorem [62, 63], this is equivalent to having  $(-1)^l \partial_t^l \Phi(q, t) \succeq 0$  for all  $l \geq 0$ . In the Laplace domain, we get

$$(3.2) \quad \Phi(q, z) = \int \frac{-1}{z + i\gamma} \mathbf{d}a_q(\gamma).$$

One immediately checks four properties from Eq. (3.2), *viz.*: (i)  $\Phi(q, z)$  is analytic for  $z \in \mathbb{C} \setminus i\mathbb{R}^-$ , obeys (ii)  $\Phi_{\alpha\beta}(q, z)^* = -\Phi_{\alpha\beta}(q, -z^*)$ , (iii)  $\lim_{z \rightarrow i\infty} \Phi_{\alpha\beta}(q, z) = 0$ , and (iv)  $\text{Re } \Phi(q, z) \succeq 0$  for  $\text{Re } z < 0$ . Here, the real and imaginary parts of a matrix have to be defined as usually done in linear algebra, *e.g.*,  $\text{Re } \mathbf{A} = (\mathbf{A} + \mathbf{A}^+)/2$ , where  $\mathbf{A}^+$  is the Hermitean conjugate. For Eq. (3.2), the nontrivial inverse also holds,

i.e. properties (i) to (iv) are sufficient to guarantee a function to be completely monotone ([62], Section 5, Theorem 2.6). The spectrum then  $\Phi''_{\alpha\beta}(q, \omega) = \text{Im } \Phi_{\alpha\beta}(q, z = \omega + i0)$  then is a superposition of Lorentzians,

$$(3.3) \quad \Phi''_{\alpha\beta}(q, \omega) = \int \frac{\gamma}{\omega^2 + \gamma^2} da_{\alpha\beta, q}(\gamma).$$

Passivity of the system already implies the spectrum to be positive, which is readily checked from the above formula. For completely monotone functions, one also has that the long-time limits [*cf.* Eq. (2.7)] of the correlators exist. If this quantity is nonvanishing, the spectrum displays an elastic contribution  $\pi F_{\alpha\beta}(q)\delta(\omega)$ .

It appears nontrivial, that approximations made in the course of solving the equations of motion of the many-particle system will lead to solutions obeying the mentioned properties. Complete monotonicity is a subtle feature, especially for matrices. We believe it is a strong argument for MCT that one can actually prove that it preserves this feature, even no matter what one takes the coupling constants to be. This kind of well-formedness is a fundamental consequence of the mathematical structure of the MCT equations, Eqs. (2.21) and (2.18b)–(2.18d), and has already been known for one-component systems [64]. By and large, the basic ideas of the proof remain the same, but some arguments have to be modified in the case of matrices. We only give a brief overview sketching the important ideas here and refer to Ref. [A8] for details.

A few notational issues are to be added. We denote the  $C^*$  algebra of  $m \times m$  matrices, equipped with standard matrix multiplication and a Hermitean scalar product, by  $\mathcal{A}$ . From elements  $a_q \in \mathcal{A}$ , we form vectors  $a = (a_q)_{q=1, \dots, M} \in \mathcal{A}^M$ . The label  $q$  plays the role of the wave vector on a discretised finite set  $q = 1, \dots, M$ . Then, all matrices appearing in the equations to be discussed are elements of  $\mathcal{A}^M$ . If one defines all matrix operators over  $\mathcal{A}$  to work elementwise in  $q$ , and introduces the maximum norm  $\|a\| = \max_q \|a_q\|$ , again  $\mathcal{A}^M$  is turned into a  $C^*$  algebra. We call elements  $a \in \mathcal{A}_+^M \subset \mathcal{A}^M$  positive, written  $a \succeq 0$ , if  $a_q \succeq 0$  holds for every  $q$ ; similarly we use  $a \succ 0$  or  $a \succeq b$ , the latter meaning  $a - b \succeq 0$ . Note that the norm preserves the ordering thus imposed, i.e. for  $a \succeq b$  we have  $\|a\| \geq \|b\|$ . The subset  $\mathcal{A}_+^M$  is called the positive cone of  $\mathcal{A}^M$ . Many details of the proofs presented below draw upon the fact that the matrices of interest are indeed elements of  $\mathcal{A}_+^M$ .

### 1.1. Existence of a Unique Completely Monotone Solution.

For a discussion of mathematical properties, it is useful to write the MCT memory kernel of Eq. (2.18c) in a more transparent form by introducing super-indices  $a = (\alpha' \alpha'')$ ,  $b = (\beta' \beta'')$ :

$$(3.4) \quad M_{\alpha\beta}(q, t) = \sum_{\vec{k} > \vec{p}} \mathcal{V}_{\alpha a}(\vec{q}, \vec{k}\vec{p}) [\Phi(k, t) \otimes \Phi(p, t)]_{ab} \mathcal{V}_{\beta b}(\vec{q}, \vec{k}\vec{p})^*,$$

where  $\otimes$  denotes a tensor product in the space of species indices. It preserves positive definiteness, i.e. the tensor product of two positive definite matrices again is positive definite, as can easily be seen in the corresponding eigenbasis. Now one sees that the vertices  $\mathcal{V}$  merely play the rôle of arbitrary test “vectors” in the definition of positive definiteness. Therefore,  $\mathbf{M}(q, t)$  is positive definite provided  $\Phi(q, t)$  is positive definite for all  $q$ , and one can easily prove by induction the statement  $(-1)^l \partial_t^l \mathbf{M}(q, t) \succeq 0$ , i.e. that  $\mathbf{M}(q, t)$  is completely monotone. Let us define a symmetric mapping on the space of positive matrices  $\mathcal{A}_+^M$ ,

$$(3.5) \quad \mathcal{F}_{\alpha\beta}[\mathbf{F}, \mathbf{G}] = \frac{1}{2} \sum_{\vec{k} > \vec{p}} \mathcal{V}_{\alpha a} [F \otimes G + G \otimes F]_{ab} \mathcal{V}_{\beta b}^*,$$

which obeys  $\mathcal{F}[\mathbf{F}, \mathbf{F}] \equiv \mathcal{F}[\mathbf{F}]$ . With this, the mapping  $\mathcal{F}[\mathbf{F}]$  is seen to preserve the semi-ordering  $\succeq$ : since  $\mathcal{F}[\mathbf{F}, \mathbf{G}] \succeq 0$  for  $\mathbf{F}, \mathbf{G} \succeq 0$  and  $\mathcal{F}$  is symmetric in  $\mathbf{F}$  and  $\mathbf{G}$ , we have  $\mathcal{F}[\mathbf{F}] - \mathcal{F}[\mathbf{G}] = \mathcal{F}[\mathbf{F} + \mathbf{G}, \mathbf{F} - \mathbf{G}] \succeq 0$  if  $\mathbf{F} - \mathbf{G} \succeq 0$ . In fact,  $\mathcal{F}[\Phi(t)]$  is a so-called absolutely monotone function of  $\Phi$  (basically a polynomial with “positive” coefficients only), and the composition of an absolutely monotone function with a completely monotone one is again completely monotone [63].

Let us mention that in the above line of reasoning, the precise form of the vertices  $\mathcal{V}$  is not even needed. In this sense, all results presented in this section are stable, since they immediately follow from the mathematical structure of the equations, not requiring specification to a certain parameter regime. Recall that the vertices can in most cases not be evaluated exactly, since one has to invoke approximations for the static structure quantities whose errors are of unknown size. The mathematical structure of the MCT equations ensures that nevertheless the results remain physical.

The existence and uniqueness of a completely monotone solution to the MCT equations of motion now is proven through construction of an iteration scheme,  $\Phi^{(n)}(t)$ ,  $n = 0, 1, 2, \dots$ , as follows. Write  $\mathbf{M}^{(n)}(t) =$

$\mathcal{F}[\Phi^{(n)}(t)]$ , and assume  $\Phi^{(n)}$  to be completely monotone. By the above results, the same holds for  $\mathbf{M}^{(n)}$ , and in particular, its Laplace transform has the properties (i) to (iv) of Eq. (3.2). Now define

$$(3.6) \quad \Phi^{(n+1)}(z) = - \left[ z\mathbf{S}^{-1} - \mathbf{S}^{-1} \left[ i\boldsymbol{\tau} + \mathbf{M}^{(n)}(z) \right]^{-1} \mathbf{S}^{-1} \right]^{-1}.$$

Then  $\Phi^{(n+1)}$  again fulfills properties (i) to (iv) of Eq. (3.2). This is easily checked for (i) to (iii). Property (iv) can be shown in two steps. First, define  $\mathbf{K}(z)$  by

$$(3.7) \quad \left[ i\boldsymbol{\tau} + \mathbf{M}^{(n)}(z) \right] \mathbf{K}(z) = -\mathbf{1}.$$

One then has, suppressing superscripts ( $n$ ) for brevity,

$$(3.8a) \quad (\operatorname{Re} \mathbf{M}(z))(\operatorname{Re} \mathbf{K}(z)) - (\boldsymbol{\tau} + \operatorname{Im} \mathbf{M}(z))(\operatorname{Im} \mathbf{K}(z)) = -\mathbf{1},$$

$$(3.8b) \quad (\operatorname{Re} \mathbf{M}(z))(\operatorname{Im} \mathbf{K}(z)) + (\boldsymbol{\tau} + \operatorname{Im} \mathbf{M}(z))(\operatorname{Re} \mathbf{K}(z)) = \mathbf{0}.$$

In general, these standard formula for the real and imaginary parts of products do not hold for matrices, but they apply here since the matrices  $(i\boldsymbol{\tau} + \mathbf{M}(z))$  and  $\mathbf{K}(z)$  in fact commute. Eliminating  $\operatorname{Im} \mathbf{K}(z)$  in the first equation using the second one, one finds for  $\operatorname{Re} z < 0$  that  $\operatorname{Re} \mathbf{K}(z) \preceq \mathbf{0}$ . But we have

$$(3.9) \quad [z\mathbf{S}^{-1} + \mathbf{S}^{-1}\mathbf{K}(z)\mathbf{S}^{-1}] \Phi(z) = -\mathbf{1},$$

and the procedure used to treat Eq. (3.7) can be repeated with Eq. (3.9), eliminating  $\operatorname{Im} \Phi(z)$  to give  $\operatorname{Re} \Phi(z) \succeq \mathbf{0}$  for  $\operatorname{Re} z < 0$ , which is the desired result. Thus we have shown that  $\Phi^{(n)}(t)$  with some completely monotone starting point,  $\Phi^{(0)}(t) = \exp[-(\mathbf{S}\boldsymbol{\tau})^{-1}t] \mathbf{S}$ , say, defines a sequence of completely monotone functions normalised to  $\Phi(t=0) = \mathbf{S}$ .

Equation (2.21) reads in the time domain

$$(3.10) \quad \boldsymbol{\tau} \dot{\Phi}(t) + \mathbf{S}^{-1}\Phi(t) + (\mathbf{M} * \dot{\Phi})(t) = \mathbf{0},$$

where we have introduced the abbreviation for the time-domain convolution,  $(f * g)(t) = \int_0^t f(t-t')g(t')dt'$ . With this, the iteration defined above can be written as

$$(3.11a) \quad \Phi^{(n+1)}(t) = \mathbf{S} + \int_0^t \mathcal{K} \left[ \Phi^{(n)}(t'), \Phi^{(n)}(t-t'), \Phi^{(n+1)}(t') \right] dt',$$

where

$$(3.11b) \quad \mathcal{K}[\mathbf{x}, \mathbf{y}, \mathbf{z}] = \boldsymbol{\tau}^{-1} (\mathcal{F}[\mathbf{x}]\mathbf{S} - (\mathbf{S}^{-1} + \mathcal{F}[\mathbf{y}])\mathbf{z}).$$

Now one constructs a sequence  $X_n(t) = \|\Phi^{(n+1)}(t) - \Phi^{(n)}(t)\|/\|\mathbf{S}\|$  and restricts the time  $t$  and the vertices  $\mathcal{V}$  to some finite closed domain. Assuming a Lipschitz constant for  $\mathcal{K}$ , the sequence  $X_n(t)$  is proven to converge uniformly to zero and thus the sequence  $\Phi^{(n)}(t)$  to converge to the unique solution  $\Phi(t)$  of Eq. (3.10). The solution depends smoothly on all control parameters for any fixed finite time interval  $0 \leq t \leq T < \infty$ . It furthermore is completely monotone, since the corresponding  $\Phi^{(n)}(z)$  by application of the continuity theorem for Laplace transforms [65] converge towards a completely monotone function  $\Phi(z)$  that is the Laplace transform of the limiting function  $\Phi(t)$ . Note that the smoothness does not necessarily hold on infinite time intervals, thus the long-time limit  $\mathbf{F}$  of the solutions needs not depend smoothly on the control parameters. Indeed, MCT brings out discontinuous changes in  $\mathbf{F}$  caused by bifurcation singularities.

In summary, this proves that the MCT solutions  $\Phi(t)$  and  $\mathbf{M}(t)$  uniquely exist and are, for colloidal dynamics, completely monotone functions. In particular, this also ensures that derived quantities such as the viscosities, Eqs. (2.33), are positive.

**1.2. Glass Form Factors.** We shall now look in more detail into the quantity  $\mathbf{F}(q)$ . Since the Laplace transform possibly has a pole at zero frequency,  $\Phi(z) = -\mathbf{F}/z + \{\text{smooth}\}$ , Eq. (2.21) implies that the form factor is a solution of

$$(3.12) \quad \mathbf{S} - \mathbf{F} = [\mathbf{S}^{-1} + \mathcal{F}[\mathbf{F}]]^{-1} .$$

In general this equation has several solutions, *e.g.*  $\mathbf{F} = \mathbf{0}$  trivially satisfies Eq. (3.12). It is also clear that the long-time limit  $\Phi(t \rightarrow \infty)$  must be a positive symmetric solution of this equation. We shall prove it to be the maximal solution with respect to the semi-ordering  $\succeq$  defined on  $\mathcal{A}_+^M$ .

To see this, first recall that the MCT functional preserves this semi-ordering, and that for  $\mathbf{F} \succeq \mathbf{G} \succ 0$ , one finds  $\mathbf{G}^{-1} - \mathbf{F}^{-1} \succeq 0$ . If we introduce a continuous mapping on the set of positive matrices by

$$(3.13) \quad \mathcal{I}[\mathbf{F}] = \mathbf{S} - [\mathbf{S}^{-1} + \mathcal{F}[\mathbf{F}]]^{-1} ,$$

it is clear that again  $\mathcal{I}$  is positive and preserves the semi-ordering. Then by induction the sequence  $\mathbf{F}^{(n+1)} = \mathcal{I}[\mathbf{F}^{(n)}]$ ,  $n = 0, 1, \dots$ , starting with  $\mathbf{F}^{(0)} = \mathbf{S} \succ 0$  is monotone and bounded,  $\mathbf{S} \succ \mathbf{F}^{(n)} \succeq \mathbf{F}^{(n+1)} \succeq 0$ ,

$n = 1, 2, \dots$ , and thus converges to some fixed point  $\mathbf{F}^* \succeq 0$  which is a solution of Eq. (3.12).

Suppose now there is some other positive symmetric fixed point  $\mathbf{F}^{**}$ . With this we introduce the mapping  $\mathbf{F} \rightarrow \tilde{\mathbf{F}}$  defined by  $\mathbf{F} = \mathbf{F}^{**} + \tilde{\mathbf{F}}$ , which maps  $\mathbf{F} = \mathbf{F}^{**}$  to  $\tilde{\mathbf{F}} = \mathbf{0}$ , and  $\mathbf{S} \succ 0$  to  $\tilde{\mathbf{S}} = \mathbf{S} - \mathbf{F}^{**} \succ 0$ . The mapping is covariant in the sense that  $\tilde{\mathbf{F}} = \tilde{\mathcal{I}}[\tilde{\mathbf{F}}]$  holds iff  $\mathbf{F} = \mathcal{I}[\mathbf{F}]$ , provided one defines  $\tilde{\mathcal{I}}$  by Eq. (3.13) with  $\sim$  applied to all quantities, and

$$(3.14) \quad \tilde{\mathcal{F}}[\tilde{\mathbf{F}}] = \mathcal{F}[\mathbf{F}] - \mathcal{F}[\mathbf{F}^{**}].$$

The mapping  $\tilde{\mathcal{I}}$  inherits the properties of  $\mathcal{I}$  noted above. Thus the sequence  $\tilde{\mathbf{F}}^{(n)} = \mathbf{F}^{(n)} - \mathbf{F}^{**}$  defined with the  $\mathbf{F}^{(n)}$  given above converges to some positive fixed point  $\tilde{\mathbf{F}}^*$  that obeys  $\tilde{\mathbf{F}}^* = \mathbf{F}^* - \mathbf{F}^{**} \succeq 0$ , and thus  $\mathbf{F}^* \succeq \mathbf{F}^{**}$  for any given fixed point  $\mathbf{F}^{**}$ . We can summarize that  $\mathbf{F}^*$  is a maximum fixed point in the sense that it is larger than all other positive definite, symmetric solutions of Eq. (3.12) with respect to the semi-ordering  $\succeq$ . The iteration scheme defined by  $\mathcal{I}$  converges to this maximum fixed point, provided the iteration is started with the upper limit  $\mathbf{S}$ . Let for the rest of this section  $\tilde{\mathcal{I}}$  be defined with setting  $\mathbf{F}^{**} = \mathbf{F}^*$ .

Indeed, this maximum fixed point is the correct long-time limit of the correlation function. Since  $\Phi(t)$  is completely monotone,  $\lim_{t \rightarrow \infty} \Phi(t) = \mathbf{G}$  exists. Similarly,  $\tilde{\Phi}(t)$  has a long-time limit  $\tilde{\mathbf{G}}$  obeying  $\mathbf{G} = \mathbf{F}^* + \tilde{\mathbf{G}}$ , thus  $\mathbf{G} \succeq \mathbf{F}^*$ . On the other hand one can integrate the time-domain equations of motion, Eq. (3.10), in order to get  $\mathbf{S}^{-1}\mathbf{G} + \mathcal{F}[\mathbf{G}](\mathbf{G} - \mathbf{S})$  since all time derivatives of completely monotone functions must vanish for long times,  $\partial_t^l \Phi_{\alpha\beta}(t \rightarrow \infty) \rightarrow 0$ . Thus the equation determining  $\mathbf{G}$  is equivalent to Eq. (3.12), and one has  $\mathbf{G} \preceq \mathbf{F}^*$ , from which one concludes  $\mathbf{G} = \mathbf{F}^*$ .

The linearisation of  $\tilde{\mathcal{I}}$  and thus  $\tilde{\mathcal{S}}\tilde{\mathcal{F}}\tilde{\mathcal{S}}$  shall be called  $\mathbf{C}$ , such that  $\mathcal{I}[\mathbf{F} + \mathbf{f}] - \mathcal{I}[\mathbf{F}] = \mathbf{C}[\mathbf{f}] + \mathcal{O}(\mathbf{f}^2)$ , dropping tildes in the remainder. Obviously,  $\mathbf{C}$  is a positive linear map on  $\mathcal{A}^M$  in the sense that  $\mathbf{C}[\mathbf{f}] \succeq 0$  for all  $\mathbf{f} \succeq 0$ . We shall furthermore assume that the mapping  $\mathbf{C}$  has no invariant subspaces. Such an assumption is plausible from the physical picture of the MCT approximation since it states that correlations for all wave vectors are coupled. Then,  $\mathbf{C}$  is a so-called irreducible mapping on

a  $C^*$  algebra, and for it there holds a generalised Perron-Frobenius theorem [66], stating in particular that there exists a non-degenerate maximum eigenvalue  $r$  to which there corresponds a uniquely determined eigenvector  $\mathbf{z} \succ 0$ . For all other eigenvalues  $\lambda$ , there holds  $|\lambda| \leq r$ , and if  $|\lambda| = r$  but  $\lambda \neq r$ , then the corresponding eigenvector  $\mathbf{e}_\lambda \not\geq 0$ . This theorem is better known for the one-component case, where  $\mathbf{C}$  is equivalent to a matrix  $C_{qp}$  all of whose elements are positive [67]. A direct proof for the multi-component case is sketched in Appendix B.

If we suppose  $r = 1 + \delta$  with some  $\delta > 0$ , we have  $\mathcal{F}[\xi\mathbf{z}] \succeq (1 + \delta)\mathbf{S}^{-1}\xi\mathbf{z}\mathbf{S}^{-1}$  with some real  $\xi > 0$ . If we set  $\hat{\mathbf{F}}^{(0)} = \xi\mathbf{z}$  and define a sequence  $\hat{\mathbf{F}}^{(n)} = \mathbf{S}^{-1}\mathbf{F}^{(n)}\mathbf{S}^{-1}$  with  $\mathbf{F}^{(n)} = \mathcal{I}[\mathbf{F}^{(n-1)}]$ ,  $n = 1, 2, \dots$ , we find after some straightforward algebra that  $\hat{\mathbf{F}}^{(1)} \succ \hat{\mathbf{F}}^{(0)} \succ 0$  for  $\xi$  sufficiently small. It follows that the sequence  $\hat{\mathbf{F}}^{(n)}$  is monotone and bounded, thus converges to some fixed point  $\hat{\mathbf{F}}^\# \succ 0$ . But this implies the existence of some fixed point  $\mathbf{F}^\# \succ \mathbf{F}^*$  of the original mapping  $\mathcal{I}$  (without tilde), in contradiction to the maximum principle proven above. We conclude that  $\delta > 0$  cannot hold.

Thus the mapping  $\mathbf{C}$  has a maximum eigenvalue  $r \leq 1$ . Inspection of Eq. (3.13) tells that  $(\mathbf{1} - \mathbf{C})$  plays the rôle of the Jacobian for the implicit equation for  $\mathbf{F}$ . We therefore distinguish regular points  $\mathcal{V}$  for which  $r < 1$  from the ‘critical’ manifold  $\mathcal{V}^c$  for which  $r = 1$ . Quantities evaluated at such critical points will be marked with superscripts  $c$ . Upon smooth changes of the input parameters,  $\mathbf{F} = \mathbf{F}^*(\mathcal{V})$  exhibits bifurcations at these critical points, identified within MCT as the ideal glass transition singularities. These are the common liquid-glass transition points, where typically  $\mathbf{F}$  shows a discontinuous jump from zero to nonzero values, caused by the appearance of new  $\mathcal{A}_+^M$  solutions to Eq. (3.12). In addition,  $r = 1$  also can describe discontinuous transitions from one glassy state to another, so-called glass-glass transitions.

The non-degeneracy of  $r$  implies that MCT glass transitions are always bifurcations of the  $A_\ell$  type, according to the classification of Arnol’d [68]. This fact was previously known for simple one-component systems, and is hereby extended to mixtures and, because of the identical

structure of the resulting equations, also to molecular systems in the site-site description [69].<sup>1</sup>

**1.3. Divergence at the Critical Point.** One can establish the existence of convergent power series of  $\Phi$  both for short times and, at regular points, for small frequencies. The latter follows from the fact that all moments of  $\tilde{\Phi}(t)$ ,

$$(3.15) \quad \Phi_n := \int_0^\infty t^n \tilde{\Phi}(t) dt,$$

and similarly of  $\tilde{M}(t)$ , exist as long as  $r < 1$ . Since the proofs are rather technical, we omit them here and refer to Ref. [A8].

A direct consequence is the relation for the zeroth moments, to be obtained from the equations of motion, Eq. (2.21), as

$$(3.16) \quad \Phi_0 = S\tau S + SM_0S.$$

Suppose now that also at the critical point  $\|\Phi_0^c\| < \infty$ , which directly implies  $\|M_0^c\| < \infty$ . Then the above equation must hold with superscripts  $c$ . But on the other hand, the linearisation  $C^c$  of  $\tilde{S}^c \tilde{M}^c \tilde{S}^c$  has a unique eigenvector  $H = z^c \succ 0$  belonging to the critical eigenvalue  $r = 1$ , and a corresponding left eigenvector  $\hat{H} \succ 0$  obeying

$$(3.17) \quad \text{tr}(\hat{H}C^c[f]) = \text{tr}(\hat{H}f).$$

Here we have defined a trace operator on  $\mathcal{A}_+^M$  by  $\text{tr}(\mathbf{A}\mathbf{B}) = \sum_{q,\alpha\beta} A_{q,\alpha\beta} B_{q,\alpha\beta}$ . It obeys  $\text{tr}(\mathbf{A}\mathbf{B}) \geq 0$  for  $\mathbf{A}, \mathbf{B} \succeq 0$  since two positive definite matrices can be simultaneously diagonalised. Thus we get  $\text{tr}(\hat{H}\tilde{S}^c \tilde{M}^c(t) \tilde{S}^c) = \text{tr}(\hat{H}\tilde{\Phi}^c(t)) + f(t)$  with some  $f(t) \geq 0$ . Integrating both sides with respect to  $t$  and applying to Eq. (3.16) at the critical point, we get the contradiction  $\text{tr}(\hat{H}\Phi_0^c) > \text{tr}(\hat{H}\Phi_0^c)$ . Thus, the zeroth moment at critical points,  $\Phi_0^c$ , cannot exist. Since  $\|\int_0^T \tilde{\Phi}^c(t) dt\|$  is a monotonically increasing function with  $T$ , one concludes that  $\|\Phi_0^c\| = \infty$  as well as  $\|M_0^c\| = \infty$ .

At noncritical points, however, the existence of a convergent power series for small frequencies implies a final exponential relaxation [65],

$$(3.18) \quad \Phi(t) - F^* = \mathcal{O}(e^{-\gamma_0 t}),$$

---

<sup>1</sup>Molecular systems, however, obey Newtonian rather than Smoluchowski dynamics. Given the numerical evidence [70, 71, A1], it seems a safe assumption that the long-time dynamics is identical in both cases.

*i.e.* there exists a minimum relaxation rate  $\gamma_0$ . The above result shows that at the critical point, no such minimum rate exists,  $\gamma_0^c = 0$ , and thus the critical correlators do not decay exponentially. Indeed, asymptotic expansions as presented below suggest that one can identify a time scale that diverges upon approaching a critical point.

## 2. Asymptotic Expansions

In this section, we develop a further extension to mixtures of mathematical results on the MCT equations that have been worked out earlier for the scalar one-component case. It deals with an asymptotic description of the correlators close to the glass transition.

Starting point for an analytic approach to Eq. (3.20) is the observation that the correlation functions  $\Phi(q, t)$  close to the glass transition show a certain time window where they are in some sense close to the plateau given by the long-time limit of the critical correlator,  $F^c(q)$ . One thus splits

$$(3.19) \quad \Phi(q, t) = F^c(q) + \tilde{\Phi}(q, t)$$

and develops an asymptotic expansion of  $\tilde{\Phi}(q, t)$ , identifying  $\|\Phi(q, t) - F^c(q)\|$  as a small quantity.<sup>2</sup> Since the central ideas in obtaining the asymptotic results are not changed with respect to the one-component case, we refer the reader to Ref. [5] for a thorough discussion and stick to a brief description of the key results in order to clarify notation here. To the author's knowledge, the results for mixtures have not been published before.

The programme is to first carry out the procedure for the solution at the critical point, where one obtains the power law of the so-called critical decay. Next, the long-time limit off the critical point is expanded in terms of some small parameter  $\sigma$  that specifies the distance to the critical point, and whose precise form has to be determined along the way. Finally, we give a full asymptotic solution for  $\Phi(q, t)$  valid on a time-scale  $t_\sigma$  that is determined from the obtained results so far.

---

<sup>2</sup>For the one-component normalised  $\phi(q, t)$  with  $\phi(q, t = 0) = 1$ , the differing conventions  $\phi(q, t) = f^c(q) + (1 - f^c(q))^2 \tilde{\phi}(q, t)$  [5] and  $\phi(q, t) = f^c(q) + (1 - f^c(q)) \tilde{\phi}(q, t)$  [72] have been used because of their advantage of resulting in normalised  $\tilde{\phi}(q, t)$ . This results in trivial differences in the definitions of the asymptotic quantities discussed below that hamper comparison.

We assume that the underlying bifurcation in  $\mathbf{F}(q)$  is of type  $A_2$ , which is also the case discussed in Ref. [5]. For other possible singularities of type  $A_\ell$ , a different expansion applies [72], among other things replacing the power laws obtained here by logarithmic decay laws. We furthermore denote all results in a form special to bilinear memory kernels,  $\mathcal{F}[\mathbf{F}] = \mathcal{F}[\mathbf{F}, \mathbf{F}]$ , as this is the relevant case for the microscopic model study in this work. The generalisation to finite polynomials of higher degree is straightforward.

The, for colloidal dynamics rigorous, assumption that the time derivatives of  $\Phi(t)$  vanish at sufficiently long times,  $t \gg t_0$ , leads to a simplification of the equations of motion. We adopt for the most part of this section the notation introduced above and omit explicit mention of the  $q$  dependence in matrix quantities and write

$$(3.20) \quad \Phi(t) = \mathbf{S}\mathbf{M}(t)\mathbf{S} - \frac{d}{dt}\mathbf{S}(\mathbf{M} * \Phi)(t),$$

which serves as the starting point for the development of the asymptotic expansion.

The reader familiar with the results of Refs. [5, 6, 72] may note that we do not absorb the time-zero quantity  $\mathbf{S}(q)$  in some normalisation. Since  $\mathbf{S}(q)$  drifts smoothly across the transition, it changes terms of linear order in  $\sigma$ . Since the asymptotic expansion as a result of the bifurcation start with  $\mathcal{O}(\sqrt{|\sigma|})$ , the leading-order asymptote is not affected by this difference. We also employ different conventions for some quantities, as long as it seems more convenient to do so in the case of matrices.

**2.1. Critical Decay.** Let us start with an expansion of the critical correlator as a power-law series,

$$(3.21) \quad \Phi^c(t) = \mathbf{F}^c + \mathbf{H}(t/t_0)^{-a} + \sum_{n=2}^{\infty} \mathbf{H}^{(n)}(t/t_0)^{-na}.$$

Inserting into Eq. (3.20) and making use of the definition of Euler's Gamma function (ignoring for the moment possible problems associated with its poles),

$$(3.22) \quad \frac{d}{dt} \int_0^t (t-t')^{-x} t'^{-y} dt' = t^{-x-y} \frac{\Gamma(1-x)\Gamma(1-y)}{\Gamma(1-x-y)} =: t^{-x-y} \beta_{x,y},$$

one determines the expansion coefficients by separating terms of equal powers in  $t^{-a}$ . To order  $t^0$ , one regains the Eq. (3.12) for the critical

glass form factor  $\mathbf{F}^c(q)$ . In next order, the coefficient  $\mathbf{H}(q)$  is determined as

$$(3.23a) \quad \mathbf{H} - 2(\mathbf{S}^c - \mathbf{F}^c)\mathcal{F}^c[\mathbf{F}^c, \mathbf{H}](\mathbf{S}^c - \mathbf{F}^c) = \mathbf{0}.$$

This is nothing but the critical Perron-Frobenius eigenvector of the linear map discussed above,  $\mathbf{H} = \mathbf{C}^c[\mathbf{H}]$ , also called the ‘critical amplitude.’ As it turns out to be convenient, let us fix  $\mathbf{H}$  and the corresponding right-eigenvector  $\hat{\mathbf{H}}$  uniquely by requiring the normalisations

$$(3.23b) \quad \text{tr}(\hat{\mathbf{H}}\mathbf{H}) = 1,$$

$$(3.23c) \quad \text{tr}(\hat{\mathbf{H}}\mathbf{H}(\mathbf{S}^c - \mathbf{F}^c)^{-1}\mathbf{H}) = 1.$$

With aid of all previous results, to each subsequent order one can write down an equation for the coefficients of the form  $(\mathbf{1} - \mathbf{C})[\mathbf{H}^{(n)}] = \mathbf{I}^{(n)}$ , with some inhomogeneity  $\mathbf{I}^{(n)}$ . As the calculation is straightforward but increasingly tedious for higher orders, we give only an exemplary result,

$$(3.24) \quad (\mathbf{1} - \mathbf{C})[\mathbf{H}^{(2)}] \\ = (\mathbf{S}^c - \mathbf{F}^c)\mathcal{F}^c[\mathbf{H}, \mathbf{H}](\mathbf{S}^c - \mathbf{F}^c) - 2(\mathbf{S}^c - \mathbf{F}^c)\mathcal{F}^c[\mathbf{F}^c, \mathbf{H}]\mathbf{H}\beta_{a,a}.$$

One now splits  $\mathbf{H}^{(n)}(q)$  into a sum of a homogeneous and a particular solution, for example

$$(3.25) \quad \mathbf{H}^{(2)}(q) = \kappa\mathbf{H}(q) + \mathbf{K}(q),$$

obeying  $\text{tr}(\hat{\mathbf{H}}\mathbf{K}) = 0$ . From this, a solubility condition for the previous order arises by applying the trace operator to get  $0 = \text{tr}(\hat{\mathbf{H}}\mathbf{I}^{(n)})$ . In particular,

$$(3.26) \quad \lambda = \text{tr}\left(\hat{\mathbf{H}}(\mathbf{S}^c - \mathbf{F}^c)\mathcal{F}^c[\mathbf{H}, \mathbf{H}](\mathbf{S}^c - \mathbf{F}^c)\right),$$

where we have introduced  $\lambda = \beta_{a,a}$ . We restrict ourselves in the discussion of  $A_2$  singularities to  $\lambda < 1$ . The power  $a$  of the asymptotic expansion is thus determined as

$$(3.27) \quad \lambda = \frac{\Gamma(1-a)^2}{\Gamma(1-2a)}.$$

To order  $t^{-3a}$ , one gets the solubility condition fixing  $\kappa$  as

$$(3.28) \quad \kappa = \frac{\lambda\zeta\mu - \xi}{\lambda - \mu} = \frac{\zeta\Gamma(1-a)^3 - \xi\Gamma(1-3a)}{\lambda\Gamma(1-3a) - \Gamma(1-a)\Gamma(1-2a)},$$

where we have set  $\mu = \beta_{a,2a} = \beta_{2a,a}$  and

$$(3.29) \quad \zeta = \frac{1}{2\lambda} \operatorname{tr} \left( \hat{\mathbf{H}}(\mathbf{S}^c - \mathbf{F}^c) \{ \mathcal{F}^c[\mathbf{H}, \mathbf{H}]\mathbf{H} \right. \\ \left. + 2\mathcal{F}^c[\mathbf{F}^c, \mathbf{K}]\mathbf{H} + 2\mathcal{F}^c[\mathbf{F}^c, \mathbf{H}]\mathbf{K} \} \right),$$

$$(3.30) \quad \xi = \operatorname{tr} \left( \hat{\mathbf{H}}(\mathbf{S}^c - \mathbf{F}^c) \mathcal{F}^c[\mathbf{H}, \mathbf{K}](\mathbf{S}^c - \mathbf{F}^c) \right).$$

Altogether, we arrive at the result for the critical decay law,

$$(3.31) \quad \Phi^c(q, t) = \mathbf{F}^c(q) + \mathbf{H}(q)(t/t_0)^{-a} (1 + \kappa(t/t_0)^{-a}) \\ + \mathbf{K}(q)(t/t_0)^{-2a} + \mathcal{O}(t/t_0)^{-3a}.$$

Note that the  $\kappa$  defined here is equivalent to the quantity denoted  $\kappa(a)$  in Ref. [5].  $\mathbf{K}(q)$  is the solution of Eq. (3.24) perpendicular to the critical eigenvector, to be evaluated by applying the resolvent of  $\mathbf{1} - \mathbf{C}$  to the left-hand side of that equation.

**2.2. Long-Time Limit.** For coupling constants slightly away from the critical ones, we assume a regular variation in all external quantities and write

$$(3.32) \quad \mathbf{S}(q) = \mathbf{S}^c(q) + \sigma \mathbf{S}^{(1)}(q) + \mathcal{O}(\sigma^2)$$

and similar for  $\mathcal{F}$ , with some small parameter  $\sigma$  used for order counting. The essence of the bifurcation is that the long-time limit of the correlation functions  $\mathbf{F}$  shows a singular variation with  $\sigma$  and can be expanded in powers of  $\sqrt{\sigma}$  for  $\sigma > 0$ , viz.:

$$(3.33) \quad \mathbf{F} = \mathbf{F}^c + \sqrt{\sigma} \bar{\mathbf{H}} + \sum_{n=2}^{\infty} \sigma^{n/2} \bar{\mathbf{H}}^{(n)}.$$

This expression is inserted into Eq. (3.12), conveniently reformulated as  $\mathbf{F} = \mathbf{S}\mathcal{F}[\mathbf{F}](\mathbf{S} - \mathbf{F})$ .

Again, the zeroth order is the correct equation for  $\mathbf{F}(q)$ , and in first order in  $\sqrt{\sigma}$  one finds that  $\bar{\mathbf{H}}$  is proportional to the critical eigenvector of the stability matrix,  $\bar{\mathbf{H}} = h \cdot \mathbf{H}$ . To order  $\sigma$ , one gets

$$(3.34) \quad (\mathbf{1} - \mathbf{C})[\bar{\mathbf{H}}^{(2)}] = (\mathbf{S}^c - \mathbf{F}^c) \mathcal{F}^c[\bar{\mathbf{H}}, \bar{\mathbf{H}}(\mathbf{S}^c - \mathbf{F}^c) - 2(\mathbf{S}^c - \mathbf{F}^c) \mathcal{F}^c[\mathbf{F}^c, \bar{\mathbf{H}}]\bar{\mathbf{H}} \\ + (\mathbf{S}^c - \mathbf{F}^c) \mathbf{S}^{c-1} \{ \mathbf{S}\mathcal{F}[\mathbf{F}^c, \mathbf{F}^c](\mathbf{S} - \mathbf{F}^c) \}_{\mathcal{O}(\sigma)},$$

where we have  $\{\mathbf{AB}\}_{\mathcal{O}(\sigma)} = (\mathbf{AB} - \mathbf{A}^c \mathbf{B}^c)/\sigma$  to linear order in  $\sigma$ . In this case, a splitting of homogeneous and particular solutions of the form

$$(3.35) \quad \bar{\mathbf{H}}^{(2)}(q) = \bar{\kappa} \mathbf{H}(q) + \bar{\mathbf{K}}(q)/(1 - \lambda)$$

with  $\text{tr}(\bar{\mathbf{H}}\bar{\mathbf{K}}) = 0$  is convenient. Furthermore, we set  $h = 1/\sqrt{1 - \lambda}$  to get the equation for  $\sigma$ ,

$$(3.36) \quad \sigma = \text{tr} \left( \hat{\mathbf{H}}(\mathbf{S}^c - \mathbf{F}^c) \mathbf{S}^{c-1} \times \right. \\ \left. \{ \mathcal{S}\mathcal{F}[\mathbf{F}^c, \mathbf{F}^c](\mathbf{S} - \mathbf{F}^c) - \mathbf{S}^c \mathcal{F}^c[\mathbf{F}^c, \mathbf{F}^c](\mathbf{S}^c - \mathbf{F}^c) \} \right).$$

The quantity  $\bar{\kappa}$  is fixed evaluating the third order, which gives with the definitions

$$(3.37)$$

$$\bar{\zeta} = \text{tr} \left( \hat{\mathbf{H}}(\mathbf{S}^c - \mathbf{F}^c) \{ \mathcal{F}^c[\mathbf{H}, \mathbf{H}]\mathbf{H} + 2\mathcal{F}^c[\mathbf{F}^c, \bar{\mathbf{K}}] + 2\mathcal{F}^c[\mathbf{F}^c, \mathbf{H}]\bar{\mathbf{K}} \} \right),$$

$$(3.38)$$

$$\bar{\xi} = \text{tr} \left( \hat{\mathbf{H}}(\mathbf{S}^c - \mathbf{F}^c) \mathcal{F}^c[\mathbf{H}, \bar{\mathbf{K}}](\mathbf{S}^c - \mathbf{F}^c) \right),$$

the solubility condition

$$(3.39) \quad (1 - \lambda)\bar{\kappa} = \frac{2\bar{\xi} - \bar{\zeta}}{2(1 - \lambda)} + \frac{1}{\sigma} \text{tr} \left( \hat{\mathbf{H}}(\mathbf{S}^c - \mathbf{F}^c) \mathbf{S}^{c-1} \times \right. \\ \left. \{ \mathcal{S}\mathcal{F}[\mathbf{F}^c, \mathbf{H}](\mathbf{S} - \mathbf{F}^c) - \mathbf{S}^c \mathcal{F}^c[\mathbf{F}^c, \mathbf{H}](\mathbf{S}^c - \mathbf{F}^c) \} \right) \\ - \frac{1}{2\sigma} \text{tr} \left( \hat{\mathbf{H}}(\mathbf{S}^c - \mathbf{F}^c) \mathbf{S}^{c-1} \{ \mathcal{S}\mathcal{F}[\mathbf{F}^c, \mathbf{F}^c]\mathbf{H} - \mathbf{S}^c \mathcal{F}^c[\mathbf{F}^c, \mathbf{F}^c]\mathbf{H} \} \right).$$

Combining the above results yields the final expression for the asymptotic behavior of the glass form factor,

$$(3.40) \quad \mathbf{F}(q) = \mathbf{F}^c(q) + \mathbf{H}(q) \sqrt{\frac{\sigma}{1 - \lambda}} \left( 1 + \sqrt{\frac{\sigma}{1 - \lambda}} \bar{\kappa} \right) \\ + \frac{\sigma}{1 - \lambda} \bar{\mathbf{K}}(q) + \mathcal{O}(\sigma^{3/2}).$$

Again we note the connection to Ref. [5]; there,  $\bar{\kappa}\sqrt{1 - \lambda}$  was denoted  $\kappa$ , and the  $\bar{\mathbf{K}}_q$  defined there is equivalent to our  $\bar{\mathbf{K}}(q)/H(q)/(1 - \lambda)$  in the one-component case.

**2.3.  $\beta$  Scaling Regime.** With some at first undetermined time scale  $t_\sigma$  that marks the window where  $\Phi(q, t)$  is close to  $F^c(q)$ , we now write for rescaled times  $\hat{t} = t/t_\sigma$ ,

$$(3.41) \quad \Phi(\hat{t}t_\sigma) = F^c + \sqrt{|\sigma|}G^{(1)}(\hat{t}) + \sum_{n=2}^{\infty} |\sigma|^{n/2} G^{(n)}(\hat{t}).$$

Similar to above, the first order leaves us with the condition that  $G^{(1)}(\hat{t})$  be parallel to  $H$ , thus

$$(3.42) \quad G^{(1)}(q, \hat{t}) = H(q)g(\hat{t}).$$

This is the celebrated factorisation theorem of MCT, which predicts that in leading order close to the glass transition, all correlation functions, when properly rescaled, collapse onto the same master curve,  $g(\hat{t})$ , for times of order  $t_\sigma$ ; the  $\beta$  scaling regime.

From the next order in  $\sigma^{n/2}$  we get as a solubility condition the equation determining  $g(\hat{t})$ . In detail, using the above result,

$$(3.43) \quad (\mathbf{1} - \mathbf{C})[G^{(2)}(\hat{t})] = \\ (\mathbf{S}^c - \mathbf{F}^c)\mathcal{F}^c[\mathbf{H}, \mathbf{H}](\mathbf{S}^c - \mathbf{F}^c)(g(\hat{t}))^2 - 2(\mathbf{S}^c - \mathbf{F}^c)\mathcal{F}^c[\mathbf{F}^c, \mathbf{H}]\mathbf{H} \frac{d}{d\hat{t}}(g * g)(\hat{t}) \\ + (\mathbf{S}^c - \mathbf{F}^c)\mathbf{S}^{c-1} \{ \mathbf{S}\mathcal{F}[\mathbf{F}^c, \mathbf{F}^c](\mathbf{S} - \mathbf{F}^c) \}_{\mathcal{O}(\sigma)} / |\sigma|.$$

Thus we get

$$(3.44) \quad \frac{d}{d\hat{t}}(g * g)(\hat{t}) = \lambda(g(\hat{t}))^2 + \text{sgn } \sigma,$$

the well-known  $\beta$  scaling equation of MCT [73]. Comparing with the expansion for the critical correlator, the initial condition is fixed to  $g(\hat{t}) \sim \hat{t}^{-a}$ ,  $\hat{t} \rightarrow 0$ . Since on the other hand,  $(t/t_\sigma)^{-a}$  must be regular in  $\sigma$ , due to the general properties of the solutions, we find  $t_\sigma^a \sim 1/\sqrt{|\sigma|}$ . Absorbing prefactors into the time scale  $t_0$ , we set  $t_\sigma = t_0|\sigma|^{-1/2a}$ . Thus the time scale diverges on both sides of the transition. As a further nontrivial result is the emergence of a second power law from Eq. (3.44) for  $\sigma < 0$ . There, the solution at long times varies as  $-B(t/t_\sigma)^b$  for  $t \gg t_\sigma$ , the so-called von Schweidler law. The exponent  $b$  is given again by Eq. (3.27), replacing  $a$  by  $-b$ . Together with this, a second time scale  $t'_\sigma$  emerges, the ‘ $\alpha$ ’ scaling time. Considering the MCT solutions as functions of  $t/t'_\sigma$ , one can derive the scaling law for the ‘ $\alpha$ ’ relaxation

process [4, 55].  $t'_\sigma$  is fixed by requiring  $\mathbf{H}\sqrt{|\sigma|}B(t/t_\sigma)^b = \mathbf{H}(t/t'_\sigma)^b$ , and thus one gets

$$(3.45) \quad t'_\sigma = (t_0/B)|\sigma|^{-\gamma}, \quad \text{with } \gamma = 1/(2a) + 1/(2b).$$

The constant  $B$  has to be determined from matching the asymptotic solutions and depends only on  $\lambda$ ; its values have been tabulated [73]. For practical purposes and to discuss the  $q$ -dependence of the relaxation, one can introduce an ‘ $\alpha$ ’ time scale  $\tau_{\phi, \alpha\beta}(q)$  for a correlation function  $\phi_{\alpha\beta}(q, t)$  as specifying 90% of the decay from its plateau value  $f_{\alpha\beta}(q)$ , *i.e.*  $\phi_{\alpha\beta}(q, \tau_{\phi, \alpha\beta}(q)) = 0.1f_{\alpha\beta}(q)$ . Upon approaching the glass transition, all these ‘ $\alpha$ ’ relaxation times will diverge according to the same power law with exponent  $\gamma$ , Eq. (3.45)

Let us proceed with the higher orders of Eq. (3.41).  $\mathbf{G}^{(2)}(\hat{t})$  can be split into homogeneous and particular solutions in the same spirit as above. Straightforward calculation brings out the solution to be of the form

$$(3.46) \quad \mathbf{G}^{(2)}(\hat{t}) = \mathbf{H}(h(\hat{t}) + (\text{sgn } \sigma)\nu) \\ + \mathbf{K}((g(\hat{t}))^2 - (\text{sgn } \sigma)/(1 - \lambda)) + \bar{\mathbf{K}}(\text{sgn } \sigma)/(1 - \lambda).$$

Here,  $h(\hat{t})$  is the correction-to-scaling master function [74, 75], determined from the next order in  $\mathbf{G}^{(n)}(\hat{t})$ ,

$$(3.47) \quad \lambda g(\hat{t})h(\hat{t}) - \frac{d}{d\hat{t}}(g * h)(\hat{t}) = \lambda\zeta \frac{d}{d\hat{t}}(g^2 * g)(\hat{t}) - \xi(g(\hat{t}))^3,$$

which is complemented by the initial condition  $h(\hat{t}) \sim \kappa\hat{t}^{-2a}$  as  $\hat{t} \rightarrow 0$ . In principle,  $\nu$  is also fixed through a solubility condition in next order, but it can be determined easier by requiring that all asymptotic expansions discussed up to now match. Using  $g(\hat{t} \rightarrow \infty) = 1/\sqrt{1 - \lambda}$  and  $h(\hat{t} \rightarrow \infty) = -(\lambda\zeta - \xi)/(1 - \lambda)^2$  for  $\sigma > 0$ , one gets

$$(3.48) \quad \nu = \frac{\bar{\kappa}}{1 - \lambda} + \frac{\lambda\zeta - \xi}{(1 - \lambda)^2},$$

and the  $\beta$  scaling expression for  $\Phi(q, t)$  including next-to-leading order corrections is

(3.49a)

$$(3.49b) \quad \Phi(q, t) = \mathbf{F}^c(q) + \mathbf{H}(q) \left( \sqrt{|\sigma|}g(\hat{t}) + |\sigma|h(\hat{t}) + \sigma\nu \right) \\ + \mathbf{K}(q) \left( |\sigma|(g(\hat{t}))^2 - \frac{\sigma}{1 - \lambda} \right) + \frac{\sigma}{1 - \lambda} \bar{\mathbf{K}}(q) + \mathcal{O}(|\sigma|^{3/2}).$$

The asymptotic description presented above is parameter-free in the sense that for all quantities appearing in Eqs. (3.31), (3.40), and (3.49) are given by microscopic expressions. The only exception is the time scale  $t_0$  marking the crossover from the ‘microscopic’ to the structural relaxation regime. For  $t_0$ , in general no analytic expression in terms of the microscopic parameters is known. It has to be determined from matching the long-time limit of the asymptotic solution at the critical point, Eq. (3.31), to the numerical solution at long times.

It is convenient for numerical calculations to chose microscopic parameters such that the time scale  $t_0$  marking the crossover from the “microscopic” to the structural relaxation regime falls into the range  $10^{-2} < t_0 < 1$ .

### 3. Equations of Structural Relaxation

The term structural relaxation is commonly applied to the long-time dynamics close to a glass transition. As numerical evidence from the solutions of the MCT equations and, independently of MCT, computer simulation results [70] suggest, the short-time dynamics enters in this regime merely by setting the global time scale  $t_0$ . The results of Sec. 3.1 lend justification to the term “structural relaxation” since one expects the correlation functions in this regime to be superpositions of decaying exponentials only.

To separate more clearly the effects of structural relaxation from those of short-time dynamics, one can invent modifications of the MCT equations of motion that replace the transient short-time dynamics with some simpler model; although this procedure is not free from ambiguity. One approach is to drop small- $z$  terms in the Laplace domain [71], but one can also drop derivatives in the time-domain and specify (divergent) initial conditions [A1]. We briefly give an extension of the approach followed in Ref. [A1] to matrices. It will be useful when later studying the effect of composition change on the relaxation towards the plateau value.

Introducing normalised correlation functions  $\phi(q, t) = \mathbf{S}^{-1/2}(q)\Phi(q, t) \times \mathbf{S}^{-1/2}(q)$  and memory kernels  $\mathbf{m}(q, t) = \mathbf{S}^{1/2}(q)\mathbf{M}(q, t)\mathbf{S}^{1/2}(q)$ , the

equations of structural relaxation, Eq. (3.20), are written as

$$(3.50a) \quad \phi(q, t) = \mathbf{m}(q, t) - \frac{d}{dt}(\mathbf{m}(q) * \phi(q))(t).$$

This set of integro-differential equations is complemented by specifying initial conditions in the form

$$(3.50b) \quad \phi(q, t \rightarrow 0) \sim \mathbf{x}(q)(t/t_*)^{-x},$$

extending Eq. (3.20) to all times  $t$ . The exponent is connected to the maximum power  $n$  of  $\Phi$  occurring in the memory kernel by  $x = 1/(n+1)$ . This form of the initial variation is motivated by the observation that this way, the highest-order term in  $t^{-x}$  exactly cancels, since  $\frac{d}{dt} \int_0^t (t - \tau)^{-nx} \tau^{-x} d\tau = 0$ . There exists then a special case of a  $q$ -independent one-component (but nontrivial) MCT model, where an exact solution of Eq. (3.50) for all  $t$  can be given in closed form [A1]. The time scale  $t_*$  as well as a set of initial amplitudes,  $\mathbf{x}(q)$ , remain undetermined in this approach. Since we intend to use this structural relaxation model in order to disentangle influences of external parameters, *i.e.* of  $\mathbf{S}(q)$ , on the structural and on the short-time part of the MCT solutions, let us specify  $\mathbf{x}(q) = \mathbf{1}$  and  $t_* = 1$  as the simplest choice independent of  $\mathbf{S}(q)$ .



## Binary Hard-Sphere Mixtures

In this chapter, the MCT results for statical and dynamical quantities of binary hard-sphere mixtures (HSM) close to the glass transition shall be discussed. Much of the discussion is in fact stimulated by recent experiments [8] which will be discussed in more detail in Sec. 5. These guide us in selecting the specific part of the parameter regime to investigate. In particular, we will provide explanations for the three mixing effects found in Ref. [8] to occur when going over from a one-component to a binary system containing up to 20% smaller spheres by volume: (i) a shift of the glass transition to higher packing fractions, (ii) an increase in the plateau values of the correlation functions at intermediate times, connected to an increase in the glass form factors, and (iii) a slowing down of the initial part of the relaxation towards this plateau.

### 1. Description of the Model

Let  $d_\alpha$ ,  $\alpha = A, B$ , denote the particle diameters. For hard-sphere systems, it is convenient to express the number density  $n$  as the fraction of the system's volume occupied by the spheres, the so-called packing fraction  $\varphi$ . For each species,  $\varphi_\alpha = (\pi/6)(x_\alpha n)d_\alpha^3$ , with  $\varphi = \sum_\alpha \varphi_\alpha$ . The thermodynamic state of a binary hard-sphere mixture is characterised by three control parameters, which we choose to be the total packing fraction  $\varphi$ , the size ratio  $\delta = d_B/d_A \leq 1$ , and the packing contribution of the smaller (B) species  $\hat{x}_B = \varphi_B/\varphi$ . We will in the following use the word 'composition change' (or 'mixing') to mean a variation (an increase) of  $\hat{x}_B$  for fixed  $\varphi$  and  $\delta$ . This choice parallels the presentation of many experimental data; it implies the number concentration of the

B particles to vary as

$$(4.1) \quad x_B = \frac{\hat{x}_B/\delta^3}{1 + \hat{x}_B(1/\delta^3 - 1)}.$$

As mentioned in the introduction, in the case of extreme size ratios there appears a percolation threshold for the motion of the small particles in the glass formed by the large ones. This transition and its precursor phenomena shall not be considered here. The MCT calculations by Bosse and coworkers found a critical size ratio  $\delta^c \approx 0.15$  [29], indeed close to the result expected from purely geometrical arguments,  $\delta^c \approx 0.154$  [76]. Our discussion focuses on size ratios  $0.6 \leq \delta \leq 1$ , which avoids this case of extreme size ratios.

Required as input for a calculation of the MCT vertices, Eqs. (2.18d) and (2.22b), are the matrices of direct correlation functions,  $c_{\alpha\beta}(q)$ , and static triplet correlation functions,  $c_{\alpha\beta\gamma}^{(3)}(\vec{q}, \vec{k})$ . Since MCT does not aim to build a theory for these quantities, they have to be taken from another source. For a discussion of the hard-sphere mixtures, static structure input shall be taken from the Percus-Yevick (PY) closure to the solution of the Ornstein-Zernike (OZ) integral equations. It has the advantage of yielding simple analytical formulæ for the direct correlation functions in an arbitrary  $N$ -component mixture of hard spheres (*cf.* Refs. [77, 78]; explicit expressions for  $c_{\alpha\beta}(q)$  are given in Appendix C). More accurate closures to the OZ equations are known, most aiming at better thermodynamic consistency, at the cost of introducing adjustable *ad hoc* parameters that have to be taken from simulation data. A notable exception for hard spheres is the Martynov-Sarkisov closure [79], generalised to mixtures by Ballone *et al.* [80], which also proceeds without adjustable parameters. It is found to be more accurate than the PY one, at the expense of breaking down at high densities. Yet, one knows from the one-component MCT that improvements aiming at thermodynamic consistency have little influence on the glassy dynamics [5]. In addition, the quality of any of these approximations at the desired high packing fractions is, unfortunately, unknown. For PY, one can say that the agreement with simulation data is fair for binary mixtures, at least about as good as in the one-component case, albeit larger errors can occur for smaller values of  $\delta$  than studied here [80, 81].

Numerical solutions for the HSM have, unless stated otherwise, been obtained setting the number of wave vectors to  $M = 200$ , on a grid

given by  $qd_A = \hat{q} \cdot \Delta q + q_0$ ,  $\hat{q} = 0, \dots, M - 1$ , and with  $\Delta q = 0.4$  and  $q_0 = 0.2$ . With  $M = 100$ , this is the discretisation used earlier for the one-component hard-sphere system [5]. The implied cutoff wave vector  $q^*d_A = 39.8$  was found there to be sufficiently large as to avoid qualitative cutoff dependencies of the solutions in the structural relaxation regime. To ensure the same for  $\delta \geq 0.5$ , the number  $M$  had to be doubled in this work.

Short-time diffusion coefficients were chosen to obey the Stokes-Einstein law,  $D_\alpha^0 \propto d_\alpha^{-1}$ . Since it is convenient for numerical calculations to have the microscopic time scale  $t_0$  in the range  $10^{-2} < t_0 < 1$ , we fix the unit of time by  $D_\alpha^0 = 0.01/d_\alpha$ .

## 2. Glass-Transition Diagram

Cuts through the liquid-glass transition manifold for different fixed size ratios  $\delta$  are depicted in Fig. 4.1. To assure that the results do not qualitatively depend on the discretisation used, we show as well the glass transition points calculated with  $M = 600$ ,  $\Delta q = 0.4/3$ ,  $q_0 = 0.2/3$ . Also included for  $\delta = 0.6$  is the result of a calculation with  $M = 100$  (implying halved cutoff wave vector; the parameters of Ref. [5]); one infers that for  $\hat{x}_B \lesssim 0.3$  this discretisation would be sufficient to produce reasonable results.

For fixed size ratio  $\delta \lesssim 0.65$ , the critical packing fraction first increases upon increasing  $\hat{x}_B$ . Since  $\hat{x}_B = 0$  and  $\hat{x}_B = 1$  both represent monodisperse hard-sphere systems, one gets  $\varphi^c(\hat{x}_B=0) = \varphi^c(\hat{x}_B=1)$ . Thus the liquid-glass transition lines for  $\delta \lesssim 0.65$  exhibit a maximum at some intermediate value of  $\hat{x}_B$ . This effect can be regarded as a direct analogue of the well-known depletion-attraction effect that is present in the system at small  $\delta$  [82]. The presence of the small particles introduces an effective attraction between the large ones that is of entirely entropic origin. Previous MCT studies have shown that such short-ranged attraction stabilises the liquid phase with respect to glass formation [83, 84, A5] (and also compared to the solid state, as found by perturbation techniques [85]). Thus we have identified effect (i) of Ref. [8] as a general mixing effect. It is a commonplace in engineering literature that the introduction of smaller components into a system typically drives the system further into the liquid phase; an effect sometimes called ‘plasticising.’ Therefore let us call the effect found here

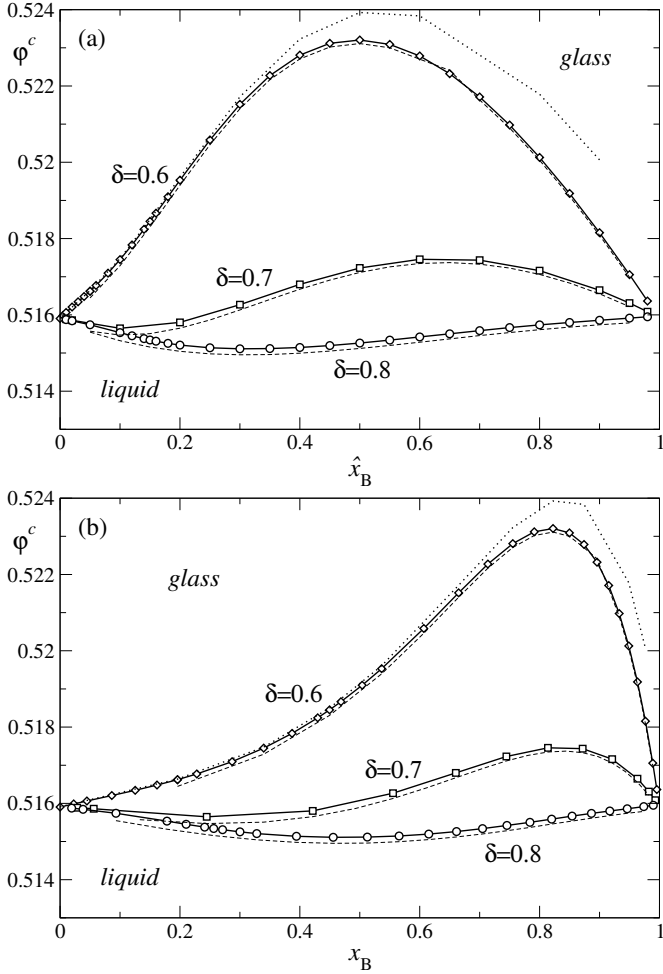


FIGURE 4.1. (a) Liquid-glass transition diagram of a binary hard sphere mixture for size ratios  $\delta = 0.6$  (diamonds),  $0.7$  (squares), and  $0.8$  (circles), plotted as critical total packing fraction  $\phi^c$  versus packing contribution of the smaller species,  $\hat{x}_B = \phi_B/\phi$ . Full lines are guides to the eyes. The dashed (dotted) lines indicate results obtained by tripling the number of grid points (halving the cutoff wave vector); see text for details. (b) Transition diagram as in (a), but plotted versus the number concentration of the smaller species,  $x_B = N_B/N$ , related to  $\hat{x}_B$  by Eq. (4.1).

an entropically induced plasticisation effect. (Justification for the use of the word plasticising shall become clearer when discussing viscosity data below.)

For less-disparate-sized mixtures, the theory predicts an inversion of this plasticisation effect. An example is shown in Fig. 4.1 for  $\delta = 0.8$ , where a decrease of  $\varphi^c$  with increasing  $\hat{x}_B$  up to some minimum point is observed. Similar MCT results for a binary soft-sphere mixture [19] are in accordance with this finding. It means that the introduction of disorder due to a small size polydispersity of the particles stabilizes the glass state. This finding can be compared to experimental results of Henderson and van Meegen [86]. These authors investigated hard-sphere like colloidal suspensions in order to discuss polydispersity effects. Their systems show bimodal particle size distributions that can be approximated by binary hard-sphere mixtures with  $\delta \approx 0.8$  and  $x_B \approx 0.2$ . The glass transition was found to occur at  $0.566 < \varphi_g < 0.577$  in the mixture, while for the less polydisperse ('one-component') system the boundaries determined from the (non)decay of the correlation functions were  $0.574 < \varphi_g < 0.581$  (*cf.* Table I of Ref. [86]). Given the known underestimation of the one-component system's critical packing fraction within MCT, this observed trend is compatible with our result. Since the liquid-glass transition diagram is not symmetric with respect to  $\hat{x}_B \leftrightarrow (1 - \hat{x}_B)$ , there even occur cases  $0.65 \lesssim \delta \lesssim 0.8$  for which one gets 'S'-shaped transition lines, in the figure exemplified by  $\delta = 0.7$ .

The magnitude of the (anti-)plasticisation effect can be quantified by the relative change of  $\varphi^c$  with respect to the one-component case,

$$(4.2) \quad \Delta\varphi^c(\delta) = (\varphi^c(\delta, x_B^\pm) - \varphi_0^c) / \varphi_0^c,$$

where  $\varphi_0^c \approx 0.5159$  is the critical packing fraction of the one-component system, and  $x_B^\pm$  are the points at which a maximum or a minimum occurs in  $\varphi^c(x_B)$  for fixed  $\delta$ . The resulting values are plotted in Fig. 4.2. We have checked that the results for  $\delta < 0.5$  do not change significantly if the cutoff wave vector is doubled to  $q^*d_A = 158.8$ . Also shown in Fig. 4.2 are data taken from Ref. [87]. There, the results of several experiments for random-loose packings (RLP) in two-component steel-ball mixtures have been presented in the same way. Random-loose packing is operationally defined as the packing fraction of the random packing obtained when pouring spheres into a container. Typically, subsequent

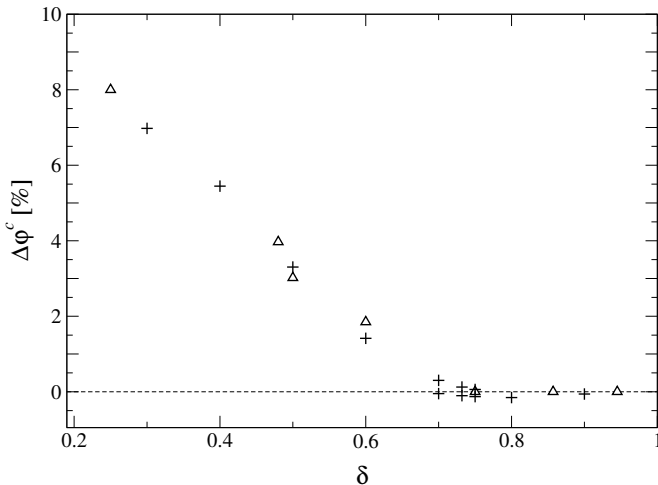


FIGURE 4.2. Maximum relative increase and decrease of the critical packing fraction,  $\Delta\varphi^c(\delta)$ , according to Eq. (4.2), as a function of the size ratio  $\delta$  (crosses), together with experimental data for random loose packing (triangles, reproduced from Ref. [87], *cf.* text). For the MCT critical packing fraction values, two symbols are noted for those  $\delta$ , where a maximum and a minimum different from the  $\delta = 1$  value could be identified.

shaking densifies the packing further, while still maintaining its randomness, until the so-called random-close packing (RCP) is reached. Such random structures are since long believed to be of relevance for the understanding of liquid structure (see *e.g.* [88]), although precise theoretical definitions exist neither of RLP nor of RCP (*cf.* [89]). Nevertheless, the reported values can be taken as a quantisation of a geometrical mixing effect, *i.e.* of modifications of the random cage structure. The fact that the variation of  $\Delta\varphi^c$  with  $\delta$  agrees with the experimental findings on a similar quantity support the conclusion that MCT is able to capture the change in the average cage structure induced by the presence of a second component.

Note that we get, as is anticipated from Fig. 4.1, negative values for  $0.65 \lesssim \delta < 1$ . Interestingly, a study of RCP in a mixture with  $\delta \approx$

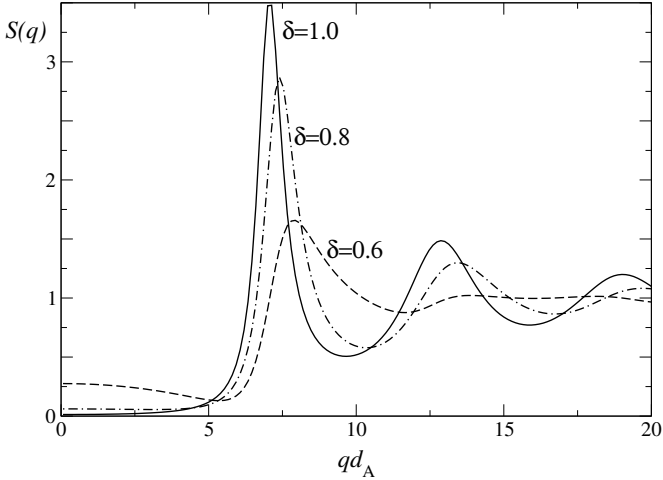


FIGURE 4.3. Total structure factor,  $S(q) = \sum_{\alpha\beta} S_{\alpha\beta}(q)$ , in Percus-Yevick approximation for binary mixtures with  $\varphi = 0.515$  and  $\hat{x}_B = 0.2$ ; at  $\delta = 1.0$  (solid line),  $0.8$  (chain-dotted line), and  $0.6$  (dashed line).

0.91 found a minute decrease in RCP when compared with the one-component system [90]. In Ref. [87], no such effect is discussed, but it is noted that there seems to be no observable change on the random packing in this region of  $\delta$ . The cited work also reports  $x_B$ -dependent data for  $\varphi_{\text{RLP}}$ , where one can identify a maximum at about  $x_B \approx 0.8$  for  $\delta = 0.6$  and  $\delta = 0.5$ . This coincides well with the maximum position found in our glass-transition diagram, Fig. 4.1(b).

Above said suggests that the change of the glass-transition point with composition can in principle be understood by looking at the geometrical structure of the system. This information is reflected by the static structure factors, which comprise the relevant input for the MCT vertex in Eq. (2.18d). In particular, it is understood that the  $q$ -vector region around the first sharp peak in  $S(q)$  is important for explaining the MCT glass transition in hard-sphere systems [1]. Fig. 4.3 shows this region for the total structure factor,  $S(q) = \sum_{\alpha\beta} S_{\alpha\beta}(q)$ , at fixed packing fraction  $\varphi = 0.515$  and composition  $\hat{x}_B = 0.2$ , and different  $\delta$ . One notices, besides a well known mixing effect for  $q \rightarrow 0$ , two trends, *viz.*: a decrease

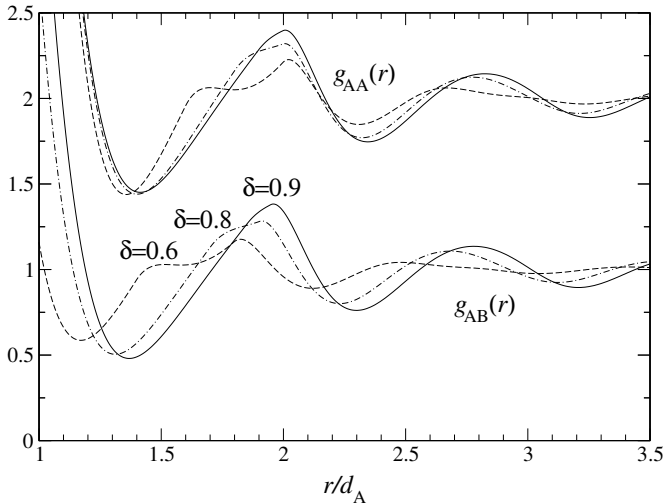


FIGURE 4.4. Partial pair correlation functions  $g_{AA}(r)$  and  $g_{AB}(r)$  of binary hard-sphere mixtures at  $\varphi = 0.516$ ,  $\hat{x}_B = 0.2$ , and different  $\delta$  within the Percus-Yevick approximation:  $\delta = 0.9$  (solid lines),  $0.8$  (chain-dotted lines), and  $0.6$  (dashed lines). Curves for  $g_{AA}(r)$  have been shifted up by  $1.0$  for clarity.

in the peak height and an increase in its wings with decreasing  $\delta$ . The interplay between these two trends is responsible for the shift in  $\varphi^c$ . At larger  $\delta$ , the increase in the wing is dominant and stabilizes the glass, *i.e.* it reduces  $\varphi^c$  with respect to the one-component system. But at  $\delta \lesssim 0.65$ , the reduction in peak height, equivalent to a weakening of the intermediate-range order, overwhelms this trend. This effect stabilises the liquid, *i.e.* increases  $\varphi^c$ . In all cases, the peak position shifts to higher  $q$ , indicating that, on average, particles are closer together in the mixture than in the one-component system. This is typical for the introduction of effective attractive interactions [A5].

Another way of looking at the local structure of the HSM is provided by the partial pair distribution functions,  $g_{\alpha\beta}(r)$ . These have been obtained numerically within the Percus-Yevick approximation as indicated in Appendix C, and results are shown in Fig. 4.4 for  $g_{AA}(r)$  and  $g_{AB}(r)$ , again at fixed  $\varphi$  and  $\hat{x}_B$  for various  $\delta$ . Here, both quantities vary more or less in phase for  $\delta \gtrsim 0.7$ , indicating that the local ordering

of the one-component system is only slightly disturbed. For smaller  $\delta$ , the one-component system's structure is modified more severely, since  $g_{AA}(r)$  and  $g_{AB}(r)$  no longer vary in phase. This can particularly be seen in the region  $1.2 \leq r/d_A \leq 2$ . One can speak of the emerging anti-phase variation of  $g_{AA}(r)$  and  $g_{AB}(r)$  as a ‘chemical ordering’ effect, responsible for the shift of the glass transition to higher packing fractions. Only for sufficiently small  $\delta$  do the small particles start to fill the ‘holes’ left by the packing of the larger ones; a picture that is commonly alluded to in the discussion of plasticising effects (based on early calculations for extreme size disparities [76, 91]). Note that however this “hole-filling” starts to occur at values of  $\delta$  still much higher than the  $\delta^c \approx 0.15$  calculated from a closest packing of the large spheres since the glass transition occurs at packing fractions considerably lower than the close-packing values.

Let us stress that the variation of  $\varphi^c$  with concentration, while being small in total, nevertheless has a large impact on the dynamics close to the glass transition. This holds since relaxation times of the liquid in this region depend strongly on the distance to the critical packing fraction, *cf.* Sec. 3.2. We shall recur to this point later on.

### 3. Glass Form Factors

The spontaneous arrest of density fluctuations within the glass state is quantified by the glass form factors  $F_{\alpha\beta}(q)$ . As explained in Sec. 3.2, their critical values  $F_{\alpha\beta}^c(q)$  are of particular importance since they specify the so-called plateau values of the correlation functions in the liquid near the liquid-glass transition.

The diagonal elements  $\hat{f}_{\alpha\alpha}(q)$  of the normalised quantities

$$(4.3) \quad \hat{f}_{\alpha\beta}(q) = F_{\alpha\beta}(q) / \sqrt{S_{\alpha\alpha}(q)S_{\beta\beta}(q)}$$

are the Debye-Waller factors for the distribution of species  $\alpha$ . In the limit  $\hat{x}_B \rightarrow 0$ ,  $\hat{f}_{BB}(q)$  approaches the spatial Fourier transform of the density distribution of a single localised B particle; it is the Lamb-Möbbaauer factor  $f_B^s(q)$  of a B particle in a hard-sphere system of A particles, *i.e.* of a tagged particle with diameter  $\delta$  in units of the surrounding spheres’ diameter. Similarly, for  $\hat{x}_B \rightarrow 1$ ,  $\hat{f}_{AA}(q)$  goes over to the Lamb-Möbbaauer factor of an A particle immersed in a hard-sphere

system of B particles, *i.e.* of a tagged particle with diameter  $1/\delta$  in units of the surrounding spheres' diameter.

Let us discuss the results for these quantities in the binary HSM by looking at two representative cases, *viz.*:  $\delta = 0.8$  (small size disparity) and  $\delta = 0.6$  (large size disparity), that show anti-plasticising and plasticising behaviour in Fig. 4.1, respectively.

Fig. 4.5 shows the critical Debye-Waller factors for small size disparity,  $\delta = 0.8$ , and various  $\hat{x}_B$ . One notices an increase of the values with increasing  $\hat{x}_B$  for almost all  $q$ . This result can be rationalised in a simple manner. With no second species present,  $\hat{f}_{AA}^c(q)$  matches the Debye-Waller factor of the one-component system,  $f^c(q)$ , shown by the full line in the upper panel of Fig. 4.5. As explained above,  $\hat{f}_{AA}^c(q)$  crosses over to the tagged-particle quantity  $f_A^{s,c}(q)$  of a bigger sphere in a surrounding fluid of smaller ones as  $\hat{x}_B \rightarrow 1$ . At  $q \rightarrow 0$ , particle conservation and momentum relaxation for the tagged particle require  $f_A^s(q \rightarrow 0) = 1$  [4]. By interpolation, one gets an increase in  $\hat{f}_{AA}^c(q)$  at small  $q$  with increasing  $\hat{x}_B$ . For large  $q$ , on the other hand, the Debye-Waller factor in a one-component system is closely oscillating around the Lamb-Möbbsauer factor of a tagged particle with equal diameter; the Lamb-Möbbsauer factor in turn is reasonably well approximated by a Gaussian,  $f^s(q) = \exp[-(qr_s)^2]$ , where  $r_s$  is the particle's localisation length [6]. The localisation length becomes the smaller the bigger the radius  $d^s$  of the tagged particle is with respect to the radius  $d$  of the surrounding spheres [6]; in particular one gets for a tagged particle of diameter  $d^s/d = 1/0.6$  (1/0.8, 1, 0.8, 0.6) the value  $r_s^c/d = 0.041$  (0.056, 0.075, 0.095, 0.136). This implies that the distribution of the  $\hat{f}_{AA}^c(q)$  is broader in the limit  $\hat{x}_B \rightarrow 1$  than in the limit  $\hat{x}_B \rightarrow 0$  as long as  $\delta < 1$ . Indeed, one infers from Fig. 4.5 that the distribution monotonically broadens with increasing  $\hat{x}_B$ . The curves for intermediate  $\hat{x}_B$  can at large  $q$  be approximated fairly well by a simple interpolation between the bordering one-component cases. We demonstrate this in the upper panel of Fig. 4.5, where the chain-dotted line represents such an interpolation,

$$(4.4) \quad \hat{f}_{AA}^c(q) \approx f^c(q) + (f_A^{s,c}(q) - f^c(q))\hat{x}_B,$$

for  $\hat{x}_B = 0.6$  and  $q > 6/d_A$ . The interpolation works even better for smaller  $\hat{x}_B$  (not shown).

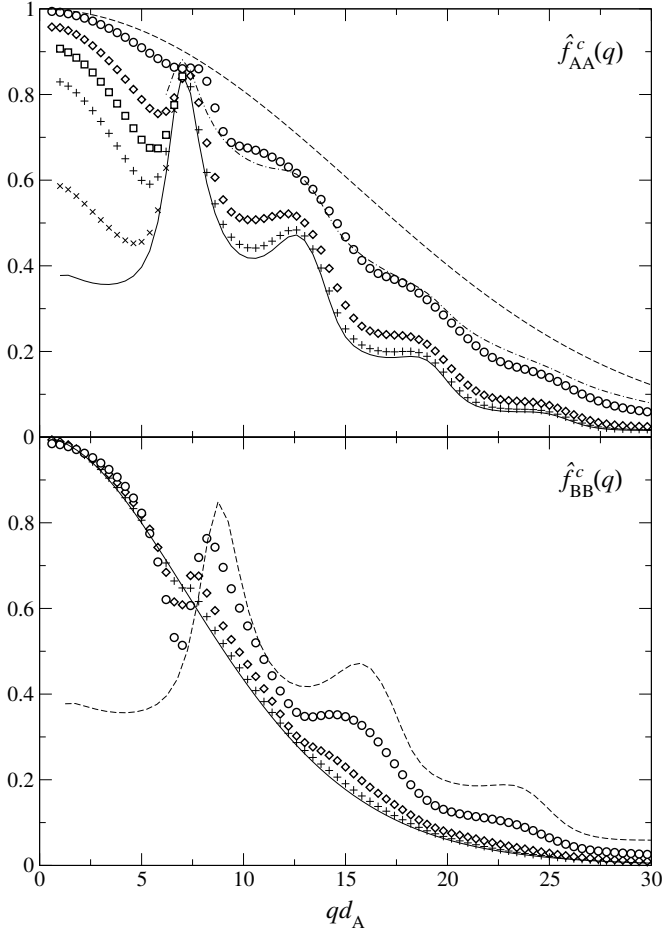


FIGURE 4.5. Critical glass form factors  $\hat{f}_{\alpha\alpha}^c(q) = F_{\alpha\alpha}^c(q)/S_{\alpha\alpha}(q)$  of a binary hard-sphere mixture with size ratio  $\delta = 0.8$ , for the large particles ( $\alpha = A$ , upper panel) and for the small particles ( $\alpha = B$ , lower panel). The packing contributions of the small spheres are  $\hat{x}_B = 0$  (solid lines), 0.05 (plus symbols), 0.2 (diamonds), 0.6 (circles), and 1.0 (dashed lines). In the upper panel, also results for  $\hat{x}_B = 0.01$  (crosses) and 0.1 (squares) are shown at small  $q$ . The chain-dotted line in the upper panel demonstrates the linear interpolation between the cases  $\hat{x}_B = 0$  and  $\hat{x}_B = 1$ , Eq. (4.4), for  $qd_A \gtrsim 6$ .

The change of  $\hat{f}_{\text{BB}}^c(q)$  can be understood along the same lines. In this case, it is the localisation length of a smaller sphere in a surrounding of big ones that matters. This yields a width of this distribution,  $f_{\text{B}}^{s,c}(q)$ , approached for  $\hat{x}_{\text{B}} \rightarrow 0$ , smaller than the one of the  $\hat{x}_{\text{B}} \rightarrow 1$  case,  $f^c(q)$ . Such an effect can be seen in the lower panel of Fig. 4.5 for  $q \gtrsim 7/d_{\text{A}}$ , where the  $\hat{f}_{\text{BB}}^c(q)$  decrease with decreasing  $\hat{x}_{\text{B}}$ . Altogether, the same rise in  $\hat{f}_{\text{BB}}(q)$  results for large  $q$  as found in the AA case. A crossover is naturally given by the size of the A particles,  $qd_{\text{A}} \approx 2\pi$ . Based on the above argument, one expects at smaller  $q$  the inverse trend, namely an increase of  $\hat{f}_{\text{BB}}^c(q)$  with decreasing  $\hat{x}_{\text{B}}$ . Yet, this is only found for  $5 \lesssim qd_{\text{A}} \lesssim 7$ . Instead one notices that for  $q \rightarrow 0$ , the  $\hat{f}_{\text{BB}}^c(q)$  for all  $\hat{x}_{\text{B}} \leq 0.6$  follow closely the result for  $\hat{x}_{\text{B}} = 0$ , *i.e.* they are still close to unity at small  $q$ . But this effect is merely a consequence of the normalisation chosen here, since it is dominated by changes in  $S_{\text{B}}(q)$  at small  $q$ .

To corroborate this, we show in Fig. 4.6 the diagonal elements of the matrix-normalised glass form factors at the transition, with the normalisation given by

$$(4.5) \quad \mathbf{f}(q) = \mathbf{S}(q)^{-1/2} \mathbf{F}(q) \mathbf{S}(q)^{-1/2}.$$

This normalisation properly takes into account the changes in the normalisation matrix  $\mathbf{S}(q)$  upon composition change; furthermore it ensures  $\mathbf{f}(q)$  to be a symmetric, positive definite matrix. Indeed one identifies for its diagonal elements  $f_{\alpha\alpha}^c(q)$  the same general trends as discussed above for the  $\hat{f}_{\alpha\alpha}^c(q)$ . Especially at small  $q$ , the behaviour expected from the above reasoning more clearly shows.  $f_{\text{BB}}^c(q)$  nicely displays the reversion of decrease *vs.* increase with increasing  $\hat{x}_{\text{B}}$ , with crossover  $qd_{\text{A}} \approx 2\pi$ .

The above argument only makes use of the fact that  $\delta < 1$ , but not of the precise ratio of localisation lengths. Since  $\delta > 1$  can be mapped to  $\delta \mapsto 1/\delta < 1$  with interchange of particle labels,  $\text{A} \leftrightarrow \text{B}$ , it is thus quite general in binary HSM. Fig. 4.7 shows the scenario for  $\delta = 0.6$ , *i.e.* for a larger size disparity, and indeed one recognizes the same trends as above. Here, the deviations of  $\hat{f}_{\text{BB}}^c(q)$  from the tagged particle's  $f_{\text{B}}^{s,c}(q)$  set in faster with increasing  $\hat{x}_{\text{B}}$  than it was the case for  $\delta = 0.8$ . But one has to keep in mind that for smaller  $\delta$ , equal changes in  $\hat{x}_{\text{B}}$  induce larger changes in the number concentration  $x_{\text{B}}$ , *cf.* Eq. (4.1). The description of  $f_{\text{AA}}^c(q)$  as a simple interpolation between  $f_{\text{A}}^{s,c}(q)$  and

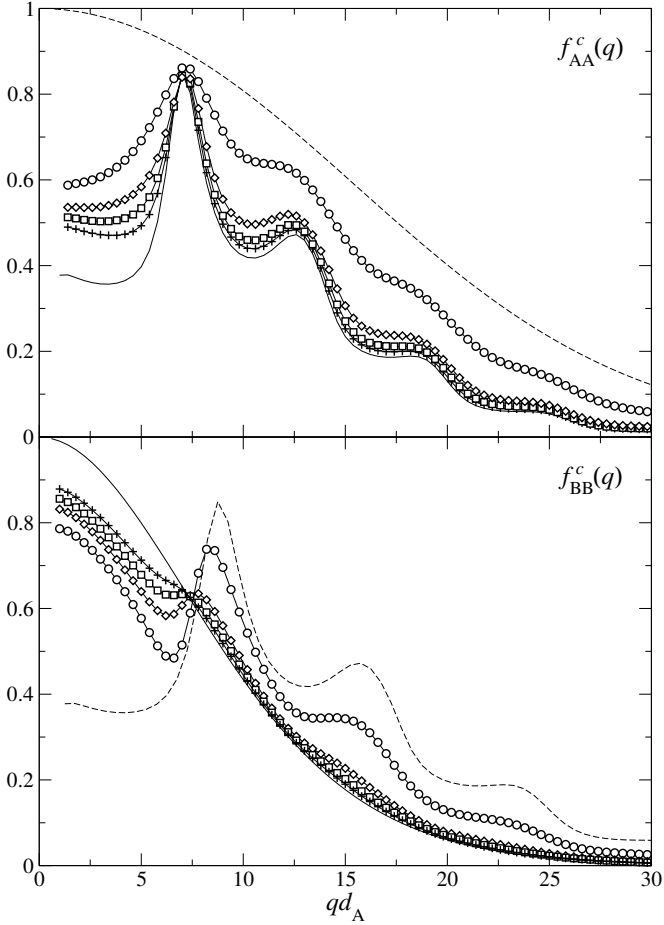


FIGURE 4.6. Matrix-normalised critical glass form factors  $f_{AA}^c(q)$  (upper) and  $f_{BB}^c(q)$  (lower panel) from Eq. (4.5) for size ratio  $\delta = 0.8$ . Symbols as in Fig. 4.5; the  $\hat{x}_B = 0.01$  curve has been omitted for clarity.

$f^c(q)$ , Eq. (4.4), as explained above is not as good as it was above (not shown), indicating that this simple picture quantitatively only works for  $\delta$  not too different from unity. The normalisation-induced behaviour at small  $q$  in  $\hat{f}_{BB}^c(q)$  is much more pronounced due to the fact that

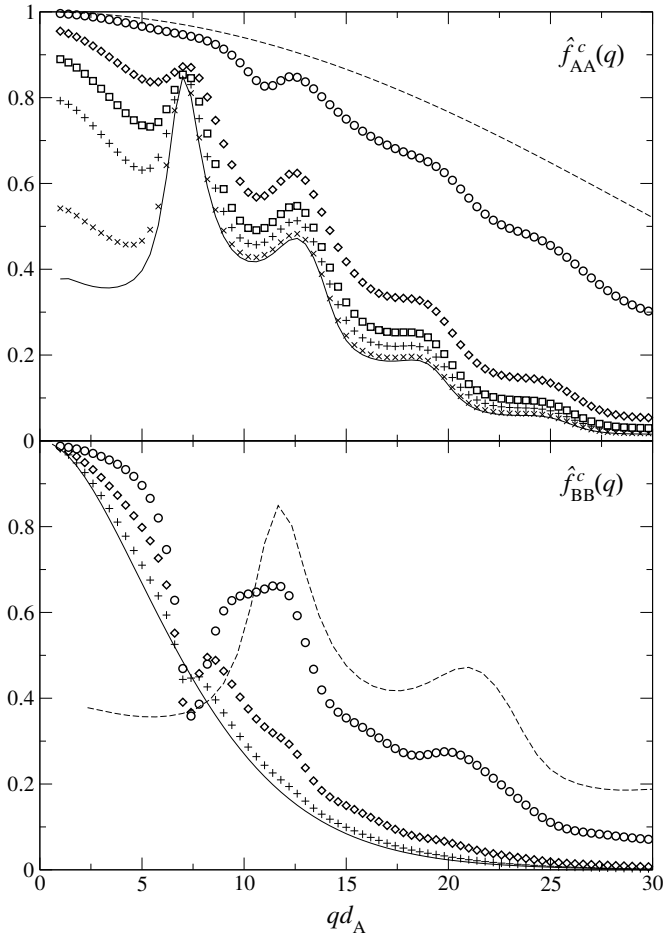


FIGURE 4.7. Critical glass form factors  $\hat{f}_{AA}^c(q)$  and  $\hat{f}_{BB}^c(q)$  of a hard-sphere mixture with size ratio  $\delta = 0.6$ ; other parameters and symbols as in Fig. 4.5.

the structure factor undergoes more severe changes at  $\delta = 0.6$  than at  $\delta = 0.8$ , *cf.* Fig. 4.3.

Let us mention in addition that for both  $\delta$ , the trend noticed for the diagonal elements is also found for  $\tilde{f}_{AB}(q) = F_{AB}(q)/S_{AB}(q)$ , a quantity

that has sometimes been discussed in the literature [8, 20]. This holds, provided one is sufficiently far away from those  $q$  where a divergence due to vanishing  $S_{AB}(q)$  occurs.

Such an increase of the glass form factors  $\hat{f}_{\alpha\beta}^c(q)$  for all  $\alpha\beta$  and several  $q$  upon mixing has also been observed by Williams and van Meegen in a dynamic light scattering experiment for  $\delta = 0.6$  and values  $qd_A < 7$  [8]. There, the  $\hat{f}_{\alpha\beta}^c(q)$  can be read off from the partial dynamical scattering functions on the liquid side close to the glass transition. Since these plateau heights are, sufficiently close to  $\varphi^c$ , independently of  $\varphi$  given by  $\hat{f}_{\alpha\beta}^c(q)$ , one expects the effect of increasing  $\hat{f}_{\alpha\beta}^c(q)$  to be largely independent of the precise procedure of ‘mixing’. This identifies the effect (ii) mentioned at the beginning of this chapter as a second general mixing effect in binary HSM. Especially at small  $q$ , the increase of  $\hat{f}_{AA}^c(q)$  in a binary mixture can be quite pronounced. In a molecular dynamics computer-simulation study, Zaccarelli *et al.* [92], studied a mixture of hard-sphere particles that were supplemented by a short-ranged square-well attraction each. In the limit of small attraction strength, a hard-sphere mixture is approached, and also in this case, the normalised glass form factors are significantly higher than expected for a one-component system. The quantity studied there (Fig. 14 of Ref. [92]) corresponds to the  $\hat{f}_{AA}(q)$  discussed here.

Typical scattering experiments, however, do not measure the partial correlation functions  $\Phi_{\alpha\beta}(q, t)$ . Rather, one measures a sum weighted with the scattering amplitudes  $b_\alpha(q)$  [52, 93],

$$(4.6) \quad \phi^m(q, t) = \frac{1}{\mathcal{N}_q} \sum_{\alpha\beta} b_\alpha(q) \Phi_{\alpha\beta}(q, t) b_\beta(q),$$

where  $\mathcal{N}_q$  is some normalisation constant we choose to satisfy  $\phi^m(q, t = 0) = 1$ . From this, we get the corresponding normalised form factor,

$$(4.7) \quad f^m(q) = \left[ \sum_{\alpha\beta} b_\alpha(q) b_\beta(q) F_{\alpha\beta}(q) \right] / \left[ \sum_{\gamma\delta} b_\gamma(q) b_\delta(q) S_{\gamma\delta}(q) \right].$$

If one assumes colloidal particles that are ideal uniform spheres with a difference in refractive index  $\Delta n = n_0 - n$  with respect to that of the solvent,  $n$ , one gets for the single-particle form factors [52],

$$(4.8) \quad b_\alpha(q) \propto \frac{d_\alpha^3}{(qd_\alpha)^3} \left( \sin(qd_\alpha/2) - \frac{qd_\alpha}{2} \cos(qd_\alpha/2) \right),$$

omitting uninteresting prefactors. In particular,  $\Delta n$  is absorbed in the normalisation. This expression for  $b_\alpha(q)$  shall be taken in the following as a generic choice for simplicity. In fact, most colloidal particles, especially those with hard-sphere like interactions, have a core-shell structure that could better be described by two concentric homogeneous spheres with different indices of refraction [94]. The  $b_\alpha(q)$  in this case read

$$(4.9) \quad b_\alpha(q) \propto \frac{d_\alpha^3}{(qd_\alpha)^3} \left[ \Delta n \cdot \left( \sin(qd_\alpha/2) - \frac{qd_\alpha}{2} \cos(qd_\alpha/2) \right) \right. \\ \left. + \Delta n_s \cdot \left( \sin(qd_\alpha/2) - \frac{qd_\alpha}{2} \cos(qd_\alpha/2) \right. \right. \\ \left. \left. - \sin(qd_\alpha/2 - ql) + \frac{q(d_\alpha - 2l)}{2} \cos(qd_\alpha/2 - ql) \right) \right],$$

where  $\Delta n_s = n_s - n_0$  is the difference of the shell's refractive index  $n_s$  to the one of the particle's core, and the shell thickness is  $l$ . The above expression sensitively depends on the three refractive indices occurring [95], thus it is less amenable to a discussion of general trends. Let us therefore evaluate Eqs. (4.6) and (4.7) with Eq. (4.8) inserted to be able to proceed without making further assumptions about the relation of refractive indices within the particles and the solvent.

Fig. 4.8 shows a plot of the thus obtained  $f^{m,c}(q)$  as a function of composition at fixed wave vector  $q = 3.4/d_A$  for different  $\delta$ . This demonstrates that both the addition to a monodisperse system of a small amount of smaller spheres as well as of a small amount of larger spheres (represented by the right part of the plot) gives rise to an increase in  $f^{m,c}(q)$  upon mixing. The increase remains as well for other, in particular smaller  $q$  (not shown). The wave vector chosen for the plot in Fig. 4.8 roughly corresponds to the minimum of  $f^c(q)$  in the one-component system; here the increase is most pronounced. Such an effect is apparent in the above mentioned study of Henderson and van Megen [86]. Among the hard-sphere like suspensions studied in this reference, there are two bimodal systems that can be approximated by hard-sphere mixtures with  $\delta \approx 0.83$  and  $\hat{x}_B = 0.1$ , and  $\delta \approx 0.73$  and  $\hat{x}_B = 0.9$ . In both cases, the obtained experimental dynamical data (Fig. 1 of Ref. [86]) shows an increase in the measured plateau value.

As stated above (Sec. 2.2), the macroscopic mechanic stability of the mixture is quantified by the elastic moduli. Figure 4.9 shows the results

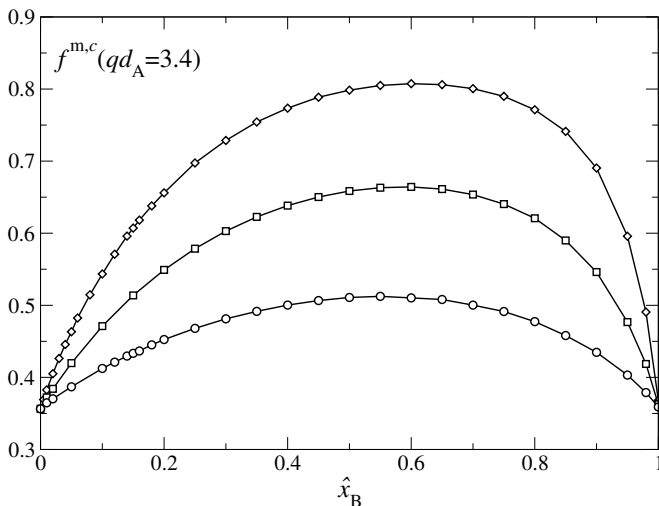


FIGURE 4.8. Normalised weighted form factor  $f^{\text{m},c}(q)$  evaluated at the glass-transition points using Eqs. (4.7) and (4.8) for different  $\delta$  as a function of  $\hat{x}_B$  at fixed  $q = 3.4/d_A$ .

for the jumps of the longitudinal and shear moduli at the critical points of the binary HSM, together with the variation of the liquid longitudinal modulus  $M_L^0$  at the transition points. All quantities are shown in units of  $(nk_B T)$  in order to more clearly reveal the effect of composition change. Note that the total density  $n$  of the system increases with increasing  $\hat{x}_B$  and superimposes a rise in the moduli one could call an ‘ideal mixing’ contribution. This ideal mixing value is given by the values of the one-component system,  $\delta M_L^c \approx 56.9$  and  $M_T^c \approx 18.3$ , shown as dashed lines in Fig. 4.9.

At intermediate  $\hat{x}_B$ , strong deviations from ideal mixing occur. For all  $\delta$  investigated here, the moduli decrease below their one-component values, indicating that the system becomes softer upon addition of smaller spheres. The effect increases with decreasing  $\delta$  and is of the order of 40% for  $\delta = 0.6$ . It is partly connected with a corresponding increase in compressibility,  $\kappa = 1/M_L^0$ . Indeed, one observes for given  $\delta$  minima in all three quantities at roughly the same  $\hat{x}_B$  (not corresponding to the minima or maxima in the glass transition diagram, Fig. 4.1). Since the compressibility is evaluated from the  $q \rightarrow 0$  zero limit of the structure

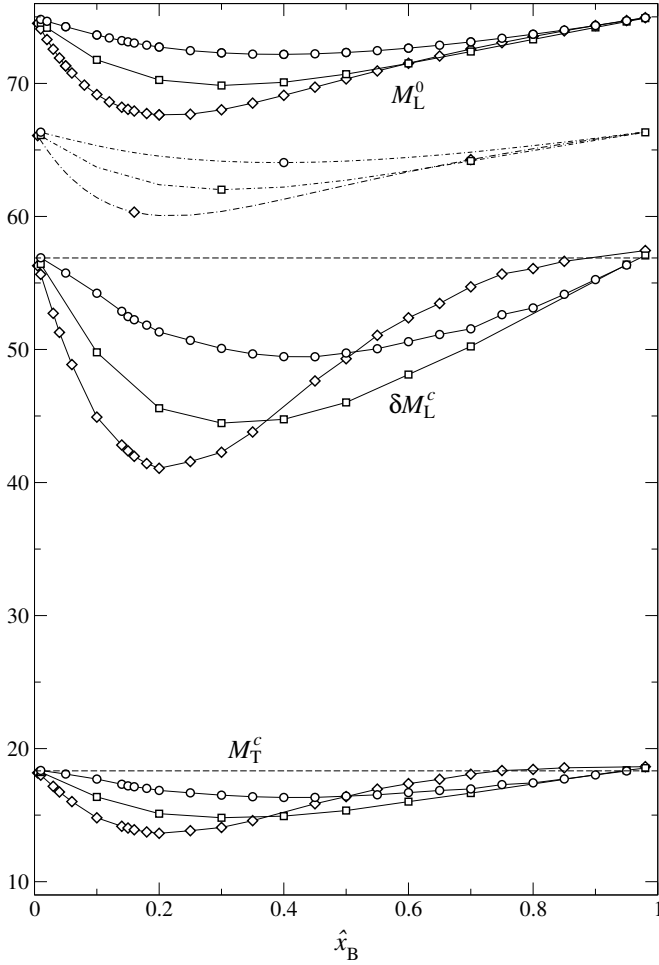


FIGURE 4.9. Isothermal longitudinal elastic modulus  $M_L^0$ , and the increase of the longitudinal and transversal elastic moduli,  $\delta M_L^c$  and  $M_T^c$ , respectively, at the liquid-glass transition points in units of  $nk_B T$  as functions of the packing contribution  $\hat{x}_B$  of the B particles. Size ratios are  $\delta = 0.8$  (circles),  $0.7$  (squares), and  $0.6$  (diamonds). Chain-dotted lines marked with corresponding symbols represent the longitudinal elastic modulus calculated from the BMCSL equation of state, see text for details. The dashed lines indicate the ideal mixing values evaluated from the one-component system.

factor in Percus-Yevick approximation, *cf.* Eq. (C.12), one has to be concerned about the thermodynamic inconsistency of the PY approximation. To ensure that the minima in the moduli are not implications of an artifact of PY, we also show in Fig. 4.9 as chain-dotted lines the thermodynamic contribution calculated from the so-called BMCSL equation of state for hard-sphere mixtures [96, 97], Eq. (C.13), explained in Appendix C. Reassuringly, the shapes of the curves are found to be very similar to the ones obtained from PY, in agreement with similar comparisons [80]. The minima in the BMCSL compressibilities are in good agreement with computer simulation data [98]. Apart from this thermodynamic contribution to the softening of the glass, mode-coupling effects still are necessary to explain the moduli for  $\delta = 0.6$ . This can be inferred from the crossing of the  $M_T^c$ - and  $\delta M_L^c$ -versus- $\hat{x}_B$  curves for different  $\delta$  that is absent in the  $M_L^0$ -versus- $\hat{x}_B$  curves.

Note that for a one-component system, a direct connection between the measured critical glass form factor at vanishing wave vector,  $f^c(q \rightarrow 0)$ , and the jump of the longitudinal elastic modulus at the glass transition exists: the larger  $f^c(q \rightarrow 0)$ , the larger the jump in the mechanical modulus, assuming prefactors to be constant. This is in general not the case for mixtures, since here the measured quantities involve a different weighted sum over the partial correlation functions, *e.g.* Eq. (4.7), than the expressions for the mechanical moduli, *e.g.* Eq. (2.34). In fact, a typical measurement can likely find increasing  $f^{\text{m},c}(q)$  due to mixing, as was demonstrated in Fig. 4.8 and found in Ref. [86]. Nevertheless, this is no indication of increasing mechanical stiffness, as can be inferred from Fig. 4.9. Similarly, the  $q \rightarrow 0$  limit of the measured structure factor loses its meaning of being proportional to the (isothermal) compressibility [99].

A few remarks concerning the mathematically rather different MCT equations used by Harbola and Das [38] are appropriate here: The equations of motion used in the cited work differ from the ones we use here, since Harbola and Das take the mass densities of the single species and the total momentum current as the distinguished variables. As a result, the matrix structure of the corresponding memory kernel  $\mathbf{M}(q, z)$  is trivial as it is determined from normalisation matrices alone. This memory kernel is closed by an expression which resembles Eq. (2.18c) with external indices  $\alpha, \beta$  summed over. Furthermore, by choice of the momentum instead of the velocity densities, the equations for the glass

form factors of Ref. [38] keep an explicit mass-ratio dependence that is absent in the theory discussed here, as was already stated above. The numerical solutions shown in Ref. [38] display some striking differences to the ones shown in Fig. 4.5 and 4.7, *viz.*: (i) they exhibit almost-zeroes in the diagonal elements that are a direct consequence of the oversimplified matrix structure of the equations used in Ref. [38] and whose physical significance is unclear; (ii) the approach of  $\hat{f}_{AA}(q)$  to the Debye-Waller factor  $f(q)$  for  $\hat{x}_B \rightarrow 0$  and to the Lamb-Möbbsauer factor  $f^s(q)$  for  $\hat{x}_B \rightarrow 1$  cannot be made out and is indeed not contained in the equations presented in Ref. [38]; (iii) the glass transition loci shift to higher  $\varphi$  for all  $\delta$ , and for certain composition ranges at  $\delta \leq 0.75$ , Harbola and Das fail to find a glass transition. The latter point seems unintelligible since one expects for any size ratio at least an arrest of the large particles for some packing fraction. In addition, a glass transition is found in experiment at  $\delta = 0.6$  and different compositions [8], which includes the parameter regime where no glass transition is predicted by the theory of Ref. [38].

Let us conclude this section with some results on the dynamics of a tagged particle in the binary HSM. We introduce tagged particles of species A and B. Since  $\delta$  is above the percolation threshold, these tagged particles become arrested at the glass transition of the host mixture. Their localisation is characterised by the long-time limit of their mean-squared displacement, Eq. (2.25).

The critical localisation lengths at the glass transition for binary HSM with  $\delta = 0.8$  and  $\delta = 0.6$  are shown in Fig. 4.10. Note that they are generally of the order of 10% of a particle's diameter, in agreement with the Lindemann criterion of melting [1, 44, 100]. The limiting values for  $\hat{x}_B = 0$  are the ones cited above, as are the ones for  $\hat{x}_B = 1$ , though shown in the figure in units of  $d_A$  and not of the surrounding spheres' diameter. Due to this, one expects a decrease in  $r_s^c(\hat{x}_B)$  with increasing  $\hat{x}_B$  in all quantities shown. In the case of small size disparity,  $\delta = 0.8$ , the decrease is almost linear in  $\hat{x}_B$ , as is demonstrated through the dashed lines in the upper panel of Fig. 4.10. These lines represent the simple interpolation based on the relative packing contributions,  $r_s^c(\alpha, \hat{x}_B) \approx r_s^c(\alpha, 0) + (r_s^c(\alpha, 1) - r_s^c(\alpha, 0))\hat{x}_B$ . It being close to the numerical results for  $\delta = 0.8$  explains why the analogous interpolation for the glass form factors, Eq.(4.4), shown in Fig. 4.5 works rather well in this case: remember that the localisation lengths set the width of

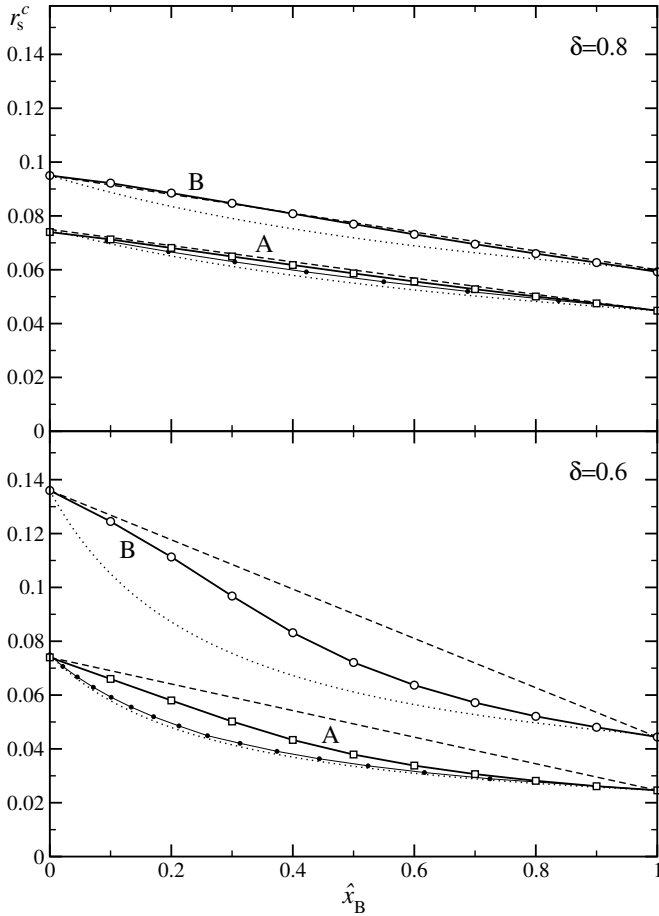


FIGURE 4.10. Critical localisation lengths  $r_s^c$  of tagged particles of species A (open squares) and B (open circles) in a binary hard-sphere mixture with size ratio  $\delta = 0.8$  (upper panel) and  $\delta = 0.6$  (lower panel) as function of the packing contribution of B particles,  $\hat{x}_B$ . The dashed and dotted lines indicate “ideal mixing” predictions, see text for details. Approximations in the spirit of the van der Waals one-fluid approximation (*cf.* text) are shown as small filled circles. Solid lines are guide to the eye.

the corresponding  $\hat{f}_{\alpha\alpha}^c(q)$  distributions. For the larger size disparity,  $\delta = 0.6$ , deviations from this “ideal mixing” arise. A tagged particle of either species is localised better than would be expected from the interpolation. Note that this is the case while at the same time the overall compressibility of the mixture becomes smaller, as is apparent from Fig. 4.9. This result might seem counter-intuitive at first, but elucidates that in general, tagged-particle quantities like the former need not have the same qualitative variation as coherent quantities like the latter.

In the discussion of thermodynamics for mixtures, effective one-component approximations are invoked from time to time to predict the change of quantities upon mixing (see [44]). Among the popular ones are the so-called van der Waals one-fluid (vdW1) [101] or the mean density approximation (MDA) [102], treating the hard-sphere mixture as a perturbation around a pure reference system. The desired quantities in the HSM are then calculated from an effective one-component hard-sphere system with diameter  $d_x$ , given by the so-called van der Waals relation as  $d_x^3 = \sum_{\alpha\beta} x_\alpha x_\beta d_{\alpha\beta}^3$ , where  $d_{\alpha\beta} = (d_\alpha + d_\beta)/2$ . This approximation can be picked up for a calculation of the localisation lengths as well: we approximate  $r_s^c(\alpha, \delta, \hat{x}_B)$  by  $r_s^c$  of a tagged particle of size  $d_\alpha$  in a one-component system with diameter  $d_x \equiv d_x(\delta, \hat{x}_B)$ . The results of this approximation are shown in Fig. 4.10 for the  $\alpha = A$  particles and  $\delta = 0.6$  and  $0.8$  as the small filled circles. We find that it yields values that are close to an interpolation that is linear in  $x_B$  (and not  $\hat{x}_B$  as in the one mentioned above). Such an interpolation is shown by the dotted lines. It gives results that are generally worse than the ones obtained from the linear- $\hat{x}_B$  interpolation. It is expected that the vdW1/MDA breaks down with increasing size disparity, and the general trend seen in Fig. 4.10 underlines this. But one could expect that such a description applies for cases where  $\hat{x}_B$  is either small or close to unity, *i.e.* where the second species is very dilute. Indeed, the approximation for the localisation lengths inspired by the vdW1/MDA gives values that are correct up to 10% for  $x_B \lesssim 0.2$  as well as for  $(1 - x_B) \lesssim 0.2$  and generally predicts the correct trend.

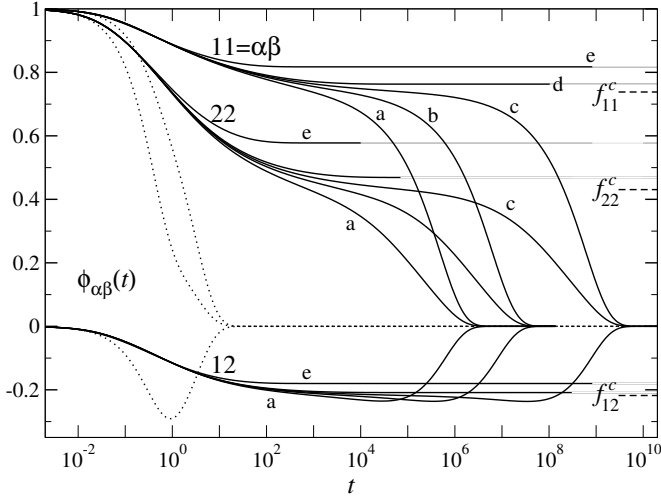


FIGURE 4.11. Matrix-normalised density correlation functions  $\phi_{\alpha\beta}(q, t) = (\mathbf{S}^{-1/2}(q)\Phi(q, t)\mathbf{S}^{-1/2}(q))_{\alpha\beta}$  for a binary hard-sphere mixture with diameter ratio  $\delta = 0.6$ , packing contribution of small particles  $\hat{x}_B = 0.2$ , and wave vector  $q = 6.2/d_A$ . The labels 11, 12, and 22 indicate the three independent matrix elements, and labels a to e correspond to total packing fractions  $\varphi = 0.518, 0.519, 0.5195, 0.52, \text{ and } 0.525$ , respectively. The dashed horizontal lines indicate the long time limit for the critical point,  $\varphi^c \approx 0.5196$ , and the dotted curves correspond to an (matrix-)exponential decay.

#### 4. Dynamics: General Features

It has been discussed above that close to a glass transition singularity, the dynamics of glass-forming systems follows an in many aspects universal scenario. This scenario has been discussed at length for one-component systems [5], and the results summarised in Sec. 3 assure that these universal results are shared by the dynamics of the discussed mixtures.

We will therefore not discuss in detail the universal aspects of the glass transition scenario in the binary HSM, involving the presence of a two-step decay with time scales that diverge as a transition point is approached. We merely demonstrate by one example what these qualitative features of the glassy dynamics are. To do so, we show in Fig. 4.11 the normalised correlation functions  $\phi(q, t) = \mathbf{S}^{-1/2}(q)\Phi(q, t)\mathbf{S}^{-1/2}(q)$  for a binary mixture with  $\delta = 0.6$  and  $\hat{x}_B = 0.2$ , at different packing fractions as indicated in the caption. As stated above, we have set  $D_\alpha^0 = 0.01/d_\alpha$ ; the wave vector is chosen as  $qd_A = 6.2$ . The solid lines correspond to the three different matrix elements of  $\phi(q)$ , and each triplet of curves that relax towards zero at roughly the same time belongs to the same packing fraction. The correspondence is also indicated by the labels a to e. One sees that upon approaching the glass transition, *i.e.* approaching a point with Perron-Frobenius eigenvalue unity, a two-step process emerges, with a plateau value given asymptotically by the critical glass form factor  $f^c(q)$ . The elements of this matrix are drawn in Fig. 4.11 as dashed horizontal lines on the right.

The power-law divergence of the relaxation time can be noted in Fig. 4.11; remember that the change in packing fraction from b to c is even smaller than that from a to b, yet the change in relaxation time is much more pronounced. To demonstrate that the glassy dynamics is anomalously slow, Fig. 4.11 also contains as dotted lines a correlation function decaying as a ‘single’ exponential,  $\phi^{(0)}(q, t) = \mathbf{S}^{-1/2}(q) \exp[-(\mathbf{S}(q) \times \tau(q))^{-1}t] \mathbf{S}^{1/2}(q)$ . By virtue of the results proven in Sec. 3.1, all functions shown in the figure are completely monotone. Note that while therefore the two diagonal elements are positive and monotonically decreasing for all times  $t$ , both needs not be true for the off-diagonal element.

Let us focus now and in the following on the general, but nonuniversal, features of the glassy relaxation in the binary HSM. To demonstrate the effects of composition changes, we investigate a horizontal cut through the transition diagram of Fig. 4.1 corresponding to fixed total packing fraction  $\varphi = 0.515$ . This value, slightly below the glass transition value for the one-component hard-sphere system, is chosen to mimic typical experimental setups (*cf.* Ref. [8]). As above, the two cases  $\delta = 0.6$  and  $\delta = 0.8$  shall be discussed as representative ones.

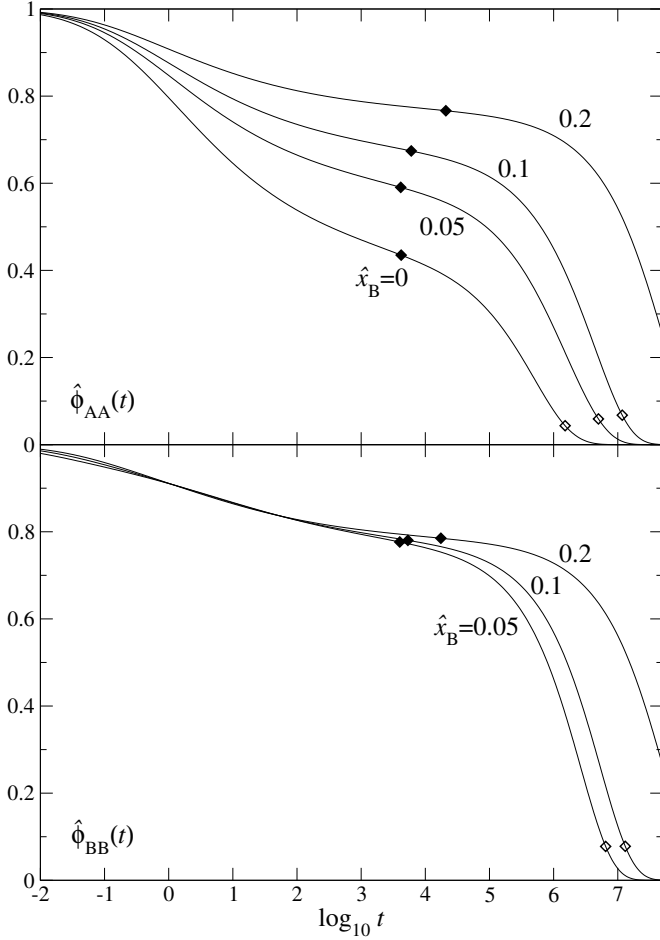


FIGURE 4.12. Normalised partial density correlation functions  $\hat{\phi}_{\alpha\alpha}(q, t) = \Phi_{\alpha\alpha}(q, t)/S_{\alpha\alpha}(q)$  for  $\alpha = A, B$  of a binary hard-sphere mixture with size ratio  $\delta = 0.8$  for fixed  $\varphi = 0.515$  and different  $\hat{x}_B$  as denoted in the figure. The wave vector is  $qd_A = 5.4$ . The unit of time here and in the following figures is chosen to set the short time diffusivity  $D_\alpha^0 = 0.01/d_\alpha$ . Filled diamonds mark the intersection of the decay curves with the plateau value  $\hat{f}_{\alpha\alpha}^c(q)$ . Open diamonds mark  $\alpha$  relaxation times defined by  $\hat{\phi}_{\alpha\alpha}(q, \tau'_{\alpha\alpha}(q))/\hat{f}_{\alpha\alpha}^c(q) = 0.1$ .

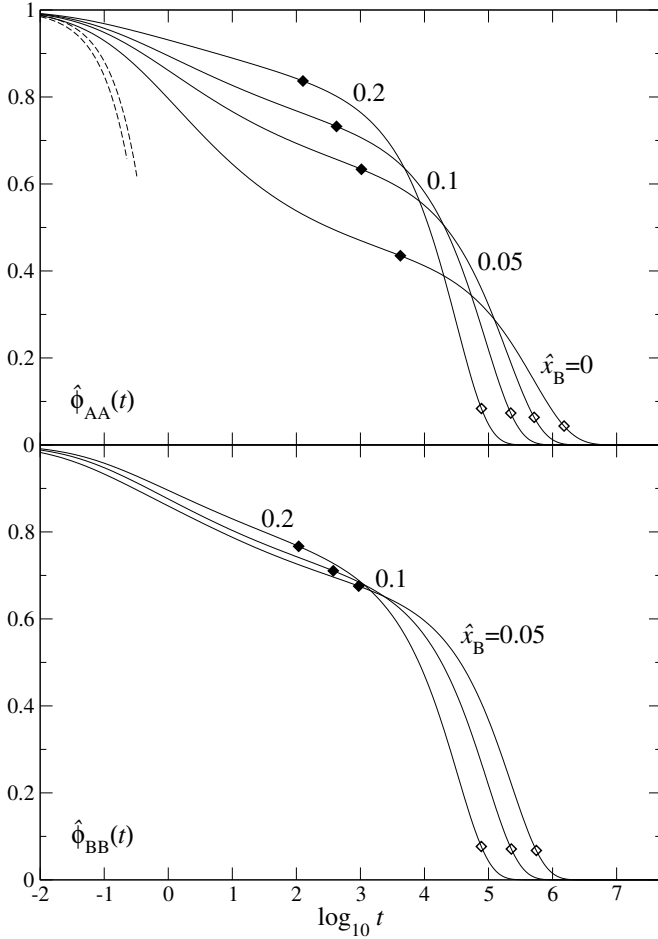


FIGURE 4.13. Normalised partial density correlation functions  $\hat{\phi}_{\alpha\alpha}(q, t)$  as in Fig. 4.12, but for  $\delta = 0.6$ . The dashed lines in the upper panel show the short-time approximation according to Eq. (4.12) for  $\hat{x}_B = 0$  and 0.2 (from left to right).

The dynamics for  $\hat{x}_B \leq 0.2$  is demonstrated for the AA and BB correlation functions by Figs. 4.12 and 4.13. We have chosen an exemplary wave vector  $q = 5.4/d_A$  somewhat below the first peak in  $\hat{f}_{AA}(q)$ ; this

corresponds roughly to the one used in the light-scattering experiment of Ref. [8]. The times  $t_\alpha(q)$  for which the correlators cross their plateau values,  $\hat{\phi}_{\alpha\alpha}(q, t_\alpha(q)) = \hat{f}_{\alpha\alpha}^c(q)$ , are marked by filled diamonds in the figures. Close to the glass transition, the correlators are close to this plateau for a large time interval; this is a manifestation of the cage effect. As can be anticipated from the discussion of Figs. 4.5 and 4.7, the plateau values increase with increasing  $\hat{x}_B$ , and the increase is more pronounced in the AA correlation function than it is in the BB one. As the distance to the transition tends to zero,  $t_\alpha(q)$  becomes independent of  $\alpha$  and  $q$  in leading order. The independence from  $\alpha$  can be seen to a good approximation from the filled diamonds in Figs. 4.12 and 4.13.

The decay of the correlators below the plateau is referred to as the ‘ $\alpha$  process’. As discussed in Sec. 3.2, a characteristic time scale  $\tau'_{\alpha\alpha}(q)$  for this decay can be defined through  $\hat{\phi}_{\alpha\alpha}(q, \tau'_{\alpha\alpha}(q)) = 0.1\hat{f}_{\alpha\alpha}^c(q)$ . These times are marked by open diamonds in Figs. 4.12 and 4.13.

For  $\delta = 0.8$ , the final relaxation time increases with increasing  $\hat{x}_B$ , reflecting the fact that for fixed  $\varphi$ , increasing  $\hat{x}_B$  corresponds to a decreasing distance to the transition, *cf.* Fig. 4.1. The scenario for  $\delta = 0.6$  is different in that respect. Here, the glass transition diagram shown in Fig. 4.1 suggests that the distance to the transition increases with increasing  $\hat{x}_B$ . Indeed, the values of  $\tau'_{\alpha\alpha}(q)$  are seen to decrease at the same time, *i.e.* the correlators show faster decay on the ‘ $\alpha$ ’ time scale upon mixing. Since the effect of increasing plateau values is present for both  $\delta$ , the correlators shown in Fig. 4.13 cross each other for some  $t_\alpha(q) < t < \tau'_{\alpha\alpha}(q)$ . Such a crossing has also been noted in experiment [8].

Again, as done in connection with Fig. 4.8, let us discuss correlation functions weighted with typical scattering amplitudes;  $\phi^m(q, t)$ , Eq. (4.6) with scattering amplitudes taken from Eq. (4.8). Fig. 4.14 shows the results for  $\delta = 0.6$  and  $\delta = 0.8$  at the same wave vector as above,  $qd_A = 5.4$ . The same qualitative picture as discussed above for the  $\hat{\phi}_{AA}$  correlator arises, albeit the increase in the plateau values is less pronounced. The reason is a destructive interference in Eq. (4.6) caused by  $\Phi_{AB}(q, t) \leq 0$ . This holds especially for  $\delta = 0.8$ , and also for smaller wave vectors. Nonetheless, some increase remains in all cases, and we argue that it is likely to be seen in a dynamical light-scattering experiment. One could be tempted to analyse such data in terms of an

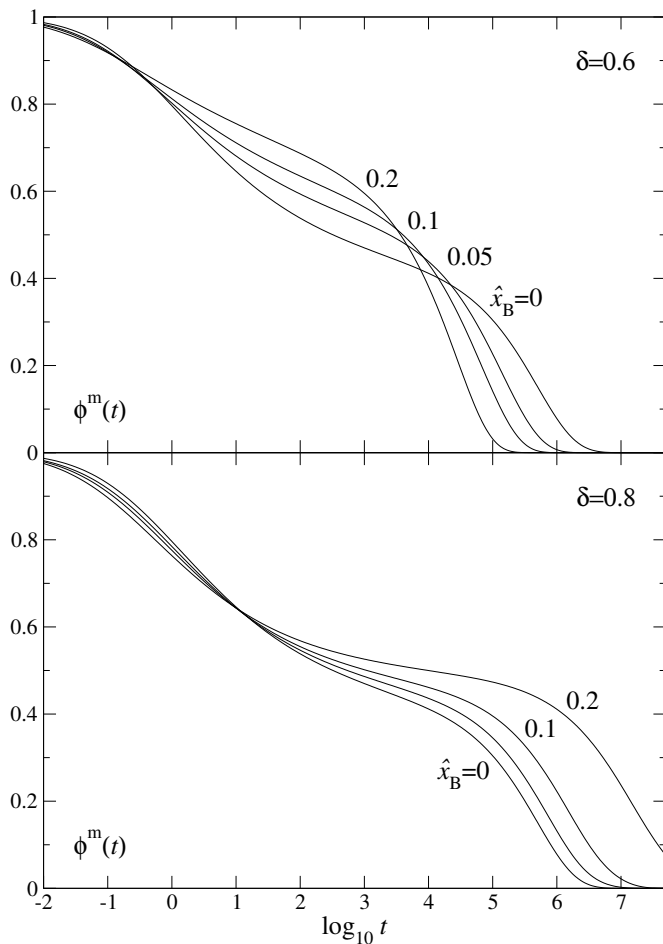


FIGURE 4.14. Sum  $\phi^m(q, t)$  of the partial density correlation functions  $\Phi_{\alpha\beta}(q, t)$  at wave vector  $qd_A = 5.4$ , weighted according to Eq. (4.6) with scattering amplitudes  $b_\alpha(q)$  as given in Eq. (4.8). The packing fraction is kept constant at  $\varphi = 0.515$ , and  $\hat{x}_B = 0, 0.05, 0.1, 0.2$  as indicated by the labels. The upper panel shows the results for size ratio  $\delta = 0.6$ , the lower one for  $\delta = 0.8$ .

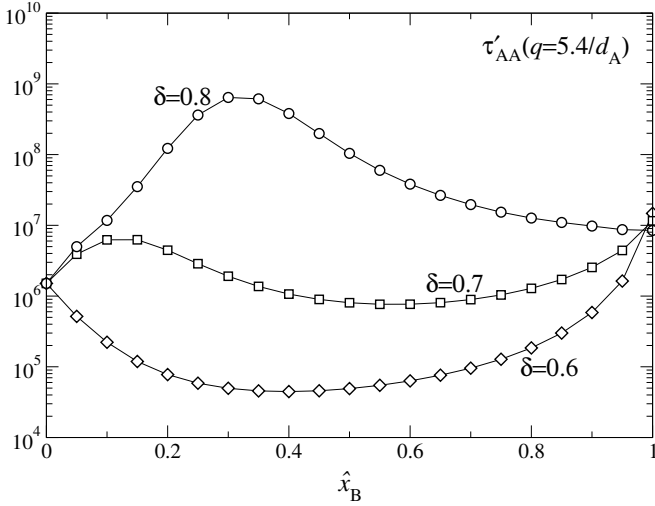


FIGURE 4.15. ‘ $\alpha$ ’ relaxation time scales  $\tau'_{AA}(q)$  defined through  $\hat{\phi}_{AA}(q, \tau'_{AA}(q)) = 0.1 \hat{f}_{AA}^c(q)$ , for  $qd_A = 5.4$ , evaluated at packing fraction  $\varphi = 0.515$  and  $\delta = 0.8$  (circles), 0.7 (squares), and 0.6 (diamonds). Lines are to guide the eye.

effective one-component model, and indeed at least for  $\delta = 0.8$  this is possible (see Sec. 5.2). Let us however repeat that the rise in the plateau values in the mixture does, contrary to what holds for one-component systems, not indicate that the system becomes mechanically stiffer upon mixing.

We now turn to a discussion of ‘ $\alpha$ ’ relaxation times  $\tau'_{\alpha\beta}(q)$ , again at  $qd_A = 5.4$ . Since the time scales are found to show the same qualitative behaviour for all three choices of  $\alpha\beta$ , let us just discuss  $\tau'_{AA}(q)$ , shown in Fig. 4.15. The figure generally corroborates the picture anticipated from the transition diagram. Since close to the transition, the ‘ $\alpha$ ’ relaxation times diverge according to  $\tau'_{\alpha\beta} \sim t'_\sigma \sim (\varphi^c - \varphi)^{-\gamma}$ , cf. Eq. (3.45), with  $\gamma > 2$ , the variations in  $\tau'_{AA}(q)$  are much more pronounced than those in  $\varphi^c$ .

Direct experimental evidence for such variation in  $\tau'_{\alpha\beta}(q)$  with the binary mixture composition comes from the DLS work of Williams and van Meegen [8], albeit only for the decrease in  $\tau'_{\alpha\beta}(q)$  at  $\delta = 0.6$  and

low  $\hat{x}_B$  concentrations. A study by Henderson *et al.* [103] seems to find the increase in  $\tau'_{\alpha\beta}(q)$  for  $\delta = 0.8$ , as will be discussed in more detail in Sec. 5.2, while the data of Ref. [86] mentioned above are taken at larger distances to the glass transition and thus show, in agreement with our expectations, no significant change in the ‘ $\alpha$ ’ time scales, except a small slowing down due to a corresponding slowing down in the short-time relaxation.

MCT predicts all ‘ $\alpha$ ’ relaxation times to be coupled. Thus the qualitative picture demonstrated in Fig. (4.15) also holds for the ‘ $\alpha$ ’ relaxation times of other experimental accessible quantities such as the dynamical viscosities or inverse diffusivities. In particular, let us discuss some results for the shear viscosity. Since colloidal suspensions are of great interest in industrial applications, a vast variety of rheological measurements on such suspensions is available. In particular, one wants to establish a high volume fraction while at the same time keeping the (shear) viscosity reasonably low as to ensure favorable flow properties. Experience has shown that this can be achieved by preparing suitable mixtures of different sized particles, since the addition of a small component to a nearly monodisperse suspension typically enhances flow (‘plasticises’), *cf.* [104–108] and references therein. Thus it is of interest to understand what combinations of size ratios and compositions will lead to a minimum in the viscosity and which not.

We plot the MCT results for the the shear viscosity of the binary HSM as functions of the composition in Fig. 4.16. In a calculation of  $\eta$  within MCT for hard-sphere systems, one has to carefully check for possible dependences on the cutoff wave vector  $q^*$ . The integrals involved have for ideal hard spheres a short-time divergence  $\eta(t) \sim t^{-1/2}$  [109] that is difficult to treat numerically. We therefore show in Fig. 4.16 also results obtained for  $\varphi = 0.515$  with a cutoff wave-vector  $q^*d_A = 119.8$  (dashed lines). The results close to the glass transition largely depend only on the long-time behavior, *i.e.*, the plateau values and ‘ $\alpha$ ’ time scales of the density correlators  $\Phi(q, t)$ . Since these values are stable for the numerical parameters used, the incorrect treatment of the short-time dynamics does not affect the results qualitatively for large enough packing fraction. We have checked that this remains true for densities as low as  $\varphi = 0.3$ , and shown the result for  $\varphi = 0.515$  as an example.

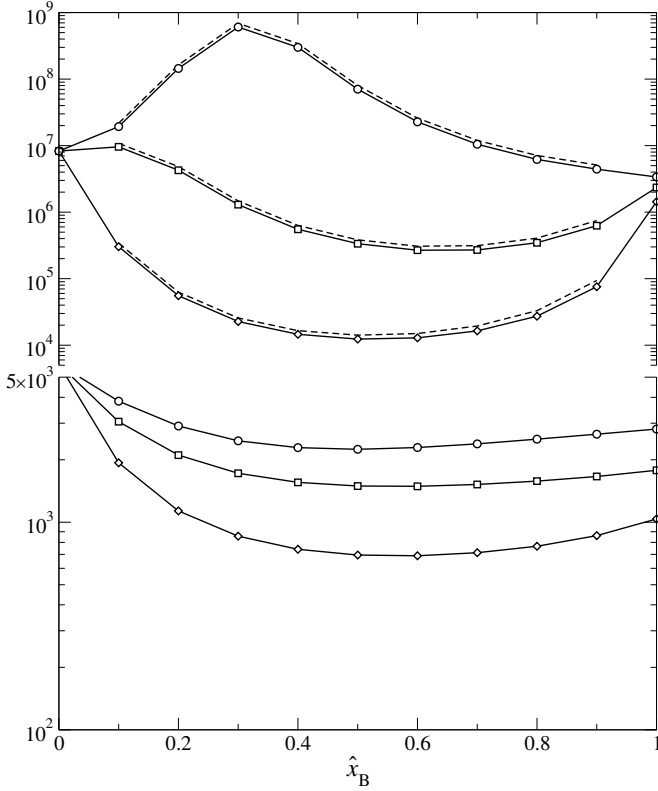


FIGURE 4.16. Shear viscosity  $\eta$  of binary HSM with packing fractions  $\varphi = 0.5$  and  $0.515$  as indicated and  $\delta = 0.8$  (circles),  $0.7$  (squares), and  $0.6$  (diamonds), as functions of the packing contribution  $\hat{x}_B$  of the smaller particles. Lines are guides to the eye. The dashed lines for  $\varphi = 0.515$  indicate results obtained with a cutoff wave vector  $q^*d_A = 119.8$  instead of  $79.8$ . All values are given in units of  $nk_B T$ .

One recognises from Fig. 4.16 a minimum in the shear viscosity for  $\delta = 0.6$  at both packing fractions that is more pronounced for higher  $\varphi$ . This just parallels the finding shown in Fig. 4.15, showing the ‘ $\alpha$ ’ time scale to become shorter. Due to the power-law divergence with  $\varphi^c - \varphi$ , the effect is bigger the lower the distance to the transition is. This

corresponds to the findings in hard-sphere like suspensions [106, 108]. In most experiments, there is a superimposed increase of the viscosity with increasing volume fraction of small particles that can render the minimum invisible. This is due to a particle size dependence of the total viscosity [106], an effect caused by hydrodynamic interactions with the suspending medium. The relative viscosity discussed here, containing the colloid-colloid contributions only, cannot account for this. Indeed, the calculated viscosity for  $\hat{x}_B = 1$  is smaller than that for  $\hat{x}_B = 0$ , due to a change of the short-time dynamics that is caused by assuming  $D_\alpha^0 \sim 1/d_\alpha$ .

The shear viscosity for  $\delta = 0.8$  also exhibits a minimum at lower packing fractions, albeit less pronounced as for  $\delta = 0.6$ . This is in agreement with experimental results that the viscosity minimum is more pronounced for smaller  $\delta$ . The minimum turns into a maximum upon increasing  $\varphi$ . This is the result of the interplay of two effects: a decreasing plateau value for the dynamical viscosity  $\eta(t)$ , *cf.* Fig. 4.9, and an increase of the ‘ $\alpha$ ’ time scale upon mixing, *cf.* Fig. 4.15. The latter is dominant close to the transition, thus the viscosity minimum turns into a maximum at a certain value of  $\varphi$ . We are only aware of a study by Greenwood *et al.* [110], where a viscosity maximum for  $\delta \approx 0.93$  and minima for smaller  $\delta$  have been found; but it is not clear in how far the data presented there can still be compared to the limit of low shear rates implicit here.

The equation for the shear viscosity in the mode-coupling approximation, Eq. (2.33) has also been derived by Nägele and Bergenholtz [61]. They build a further analytical treatment of this expression on the low-density limit of the direct correlation functions entering the vertices, Eq. (2.39). Upon further approximating  $\Phi_{\alpha\beta}(k, t) \approx \delta_{\alpha\beta} x_\alpha \exp[-k^2 D_\alpha^0 t]$  and assuming a Stokes-Einstein relation  $D_\alpha^0 \sim 1/d_\alpha$ , they get at constant packing fraction

$$(4.10) \quad \eta \sim \sum_{\alpha\beta} \hat{x}_\alpha \hat{x}_\beta \frac{(1 + x_{\alpha\beta})^4}{16x_{\alpha\beta}^2},$$

where  $x_{\alpha\beta} = d_\alpha/d_\beta$ . For a binary mixture, this expression yields a maximum of the viscosity for  $\hat{x}_B = 1/2$  whose magnitude increases with increasing  $\delta$ . It has been speculated that the minimum observed in experiment is thus due to hydrodynamic interactions. Yet our numerical solutions of the MCT equations for  $\varphi \geq 0.3$ , while neglecting HI, show

no indication of such a maximum. The low-density treatment misses the variation in  $\mathcal{S}(q)$  at high densities that leads to a compressibility maximum, *cf.* Fig. 4.9, which in turn is partially responsible for the viscosity minimum observed at lower densities. It of course also misses the variation of the ‘ $\alpha$ ’ time scale at higher densities. In addition, one can question the validity of the above expression for low densities, since it only considers the mode-coupling contribution to the viscosity. It appears that the inclusion of other effects again produces a minimum at low densities [111]. Viscosity minima have also been derived recently using an integral equation theory [112], but this theory builds upon an *ad hoc* expression for the variation of the diffusion constants with density.

Rates for homogeneous nucleation are affected by the diffusivities; at the glass transition, it ceases, and only heterogeneous nucleation prevails, as has been observed for hard-sphere like colloids [113]. This connection could be used to map out the liquid-glass state diagram in experiments on effective one-component systems [114]. Fig. 4.15 thus hints towards a possible strong dependence of homogeneous nucleation rates in binary mixtures on composition. Indeed this is observed [14], although nucleation phenomena in mixtures appear to be too complex to allow for drawing a direct connection between vanishing diffusivity (diverging relaxation time) and the cease of nucleation.<sup>1</sup> In studies of binary HSM crystallisation, deviations from the theoretically predicted equilibrium phase diagram have been found in the vicinity of equimolarity [116], attributed due to non-equilibrium effects. But the disappearance of nucleation in this study does not display the same trend with  $\delta$  and  $\hat{x}_B$  as the glass-transition lines presented above. Intriguingly, a recent molecular dynamics simulation study has observed that crystallisation of a binary HSM becomes increasingly difficult with decreasing size ratio as long as  $\delta \gtrsim 0.73$ , and for significantly smaller size ratios sets in more easily again [117]. This can be favorably compared with the trend of the diffusivities expected from Fig. 4.1.

---

<sup>1</sup>There is a fascinating variety of alloy-type crystals forming in binary hard-sphere mixtures, some even known from gem opals [115]. Little is known about the nucleation kinetics of these complex structures.

## 5. Asymptotic Description

In Figs. 4.12 and 4.13, a trend can be noticed for the relaxation onto the plateau value. This part of the relaxation, which deals with the onset of structural relaxation, displays a slowing down of the relaxation with increasing  $\hat{x}_B$  for both  $\delta$  considered here; it thus identifies effect (iii) of Ref. [8] mentioned earlier.

In principle, the relaxation in this time window is a result of both structural and transient relaxation. The latter is in a leading approximation given by

$$(4.11) \quad \Phi(q, t) = \exp[-q^2 \mathbf{D}(q)t] \mathbf{S}(q),$$

with the matrix of short-time collective diffusion constants  $\mathbf{D}(q) = (q^2 \mathbf{S}(q) \boldsymbol{\tau}(q))^{-1}$ . In particular, for a binary mixture this yields

$$(4.12) \quad \hat{\phi}_{AA}(q, t) = 1 - q^2 D'(q)t + \mathcal{O}(t^2),$$

where  $D'(q) = x(q)D(q)$  with  $x(q) = S(q)/S_{AA}(q)$ , and  $D(q)$  and  $S(q)$  are the collective diffusion constant and the structure factor of the one-component system, respectively. It has already been noticed in Ref. [8] that  $x(q) < 1$  for small  $q$ . Thus one expects a slowing down of the short-time diffusion due to mixing in the limit of small  $q$ . For the wave vector discussed above,  $qd_A = 5.4$ , the effect is small though: with  $\delta = 0.6$ ,  $\varphi = 0.515$ , one gets  $x \approx 0.82$  (0.76, 0.78) for  $\hat{x}_B = 0.05$  (0.1, 0.2). The approximations resulting from Eq. (4.12) are shown in Fig. 4.13 for  $\hat{x}_B = 0$  and 0.2 as dashed lines. One infers from the figure that the description in this case is valid only for  $\hat{\phi}_{AA}(q, t) \geq 0.98$ . Note also that  $x(q)$  is not monotonous in  $\hat{x}_B$ , while the mentioned slowing down of the short-time relaxation upon mixing is. Furthermore, at larger wave vectors, one has  $x(q) > 1$  since  $x(q \rightarrow \infty) = 1/x_A$ , yielding faster short-time diffusion upon mixing. Thus we conclude that the change in the short-time diffusion coefficients is not sufficient to explain the observed slower relaxation.

Let us therefore focus on the structural relaxation contribution, which shall be defined as discussed in Sec. 3.3. Figure 4.17 presents solutions of Eqs. (3.50) for  $\delta = 0.6$  and different  $\hat{x}_B$  at fixed  $\varphi$ , together with the solutions reproduced from Fig. 4.13. The long-time parts of corresponding curves can be scaled on top of each other, demonstrating that there the dynamics depends on the short-time behaviour only through

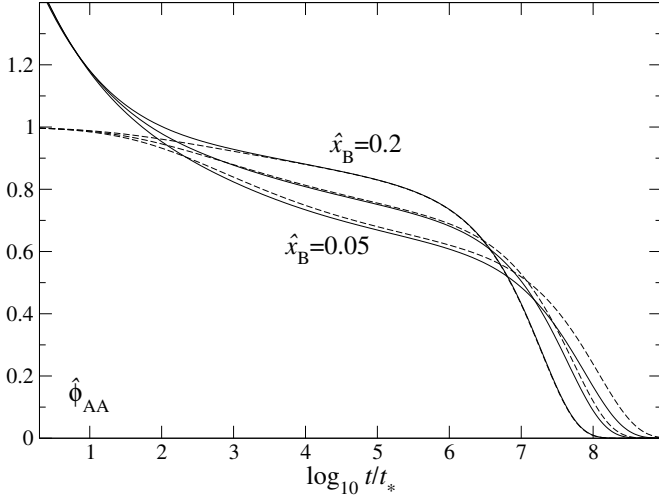


FIGURE 4.17. Structural relaxation dynamics (solid lines) as defined by Eqs. (3.50) for a binary HSM with  $\delta = 0.6$  and  $\varphi = 0.515$ , with small particle packing contributions  $\hat{x}_B = 0.2$ ,  $0.1$ , and  $0.05$  as indicated. The dashed lines are the solutions for the same parameters of the general MCT equations, Eqs. (2.21), with the time scaled to match the structural-relaxation solution at long times for  $\hat{x}_B = 0.2$ .

a scaling time  $t_0$ . The matching is demonstrated for the  $\hat{x}_B = 0.2$  curve. Instead of matching  $t_0$  and  $t_*$  independently for each  $\hat{x}_B$ , we have applied the same rescaling as used for  $\hat{x}_B = 0.2$  in all cases. The resulting offset between the solid and the dashed lines therefore demonstrates a decrease of the scaling time  $t_0(\hat{x}_B)$  with composition.

At short times, all structural relaxation curves follow the same asymptote  $t^{-1/3}$ , and one notices that they deviate from one another at roughly  $t = 10t_*$ , showing slower relaxation for larger  $\hat{x}_B$ . This demonstrates that the observed slower relaxation is a result of structural relaxation rather than transient dynamics.

A deeper understanding of the long-time relaxation close to the plateau values is provided by the asymptotic expansion discussed in Sec. 3.2.

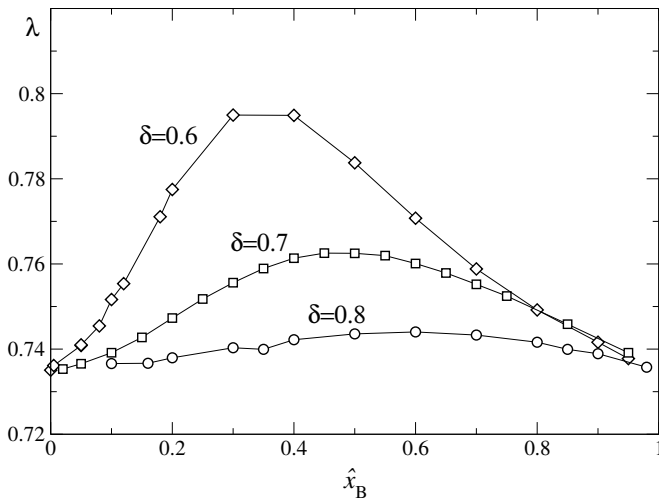


FIGURE 4.18. Exponent parameters  $\lambda$  corresponding to the points shown in the transition diagram, Fig. 4.1; symbols indicate  $\delta = 0.6$  (diamonds),  $0.7$  (squares), and  $0.8$  (circles). The lines are guides to the eye.

Remember that all parameters appearing in this expansion can be calculated given knowledge of the static structure of the system. The only exception to this is the time scale  $t_0$ . The latter is fixed by matching the long-time limit of the asymptotic solution at the critical point,  $\Phi^c(q, t) = \mathbf{F}^c(q) + \mathbf{H}(q)(t/t_0)^{-a} + \mathcal{O}(t^{-2a})$ , to the numerical solution at long times.<sup>2</sup> One gets  $t_0 = 0.4408$  ( $0.2026$ ,  $0.1385$ ) for  $\hat{x}_B = 0$  ( $0.1$ ,  $0.2$ ) and other microscopic parameters as given above.

We first investigate the variation of the exponent parameter  $\lambda$ , Eq. (3.26) as a function of the composition, shown in Fig. 4.18. The exponent parameter is larger than the value found for the pure hard-sphere system,  $\lambda(\hat{x}_B = 0) = \lambda(\hat{x}_B = 1) = 0.736$ . It exhibits a maximum smaller than  $0.8$  for  $\delta \geq 0.6$ . As a result, the critical exponent  $a$ , Eq. (3.27), decreases relative to the one-component hard-sphere value  $a = 0.311$ . In particular, we get  $\lambda = 0.752$  ( $0.778$ ) and from this  $a = 0.304$  ( $0.291$ ) for

<sup>2</sup>For technical reasons, the  $\mathcal{O}(t^{-2a})$  terms in Eq. (3.49) are also taken into account in this procedure. The resulting accuracy is still limited to about three leading digits in  $t_0$  since  $t \rightarrow \infty$  cannot easily be approached on a computer.

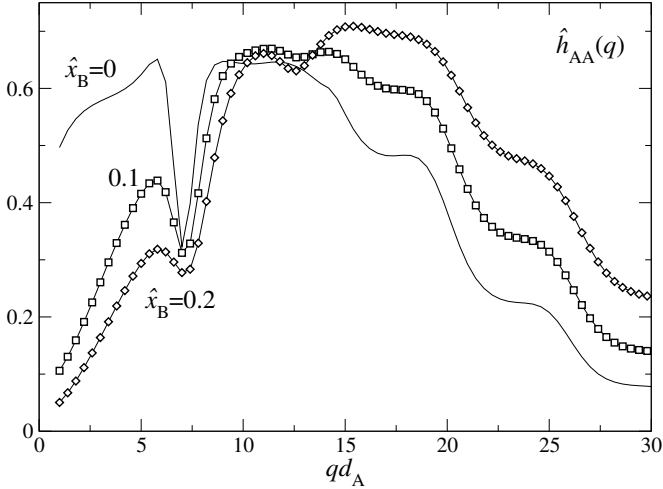


FIGURE 4.19. The normalised critical amplitudes  $\hat{h}_{AA}(q) = H_{AA}(q)/S_{AA}^c(q)$  for  $\delta = 0.6$  and  $\hat{x}_B = 0.0, 0.1,$  and  $0.2$  as indicated.

$\hat{x}_B = 0.1$  ( $0.2$ ). As a consequence, the stretching of the decay towards the plateau increases somewhat with increasing  $\hat{x}_B$  and decreasing  $\delta$ . But this effect is rather small and cannot explain the slower relaxation towards the plateau discussed above.

Figure 4.19 shows the critical amplitudes  $\mathbf{H}(q)$ , Eqs. (3.23) in the case  $\delta = 0.6$  for the AA correlator, normalised according to  $\hat{h}_{AA}(q) = H_{AA}(q)/S_{AA}^c(q)$  in order to match the representation of Figs. 4.12 and 4.13. Qualitatively the same picture arises for  $\delta = 0.8$ , albeit less pronounced. While there is no general trend valid for all  $q$ , we note that at wave vectors below the first peak in  $\hat{f}_{AA}(q)$ , here identified as the first dip in  $\hat{h}_{AA}(q)$ , the amplitudes  $\hat{h}_{AA}(q)$  decrease significantly upon increasing  $\hat{x}_B$ . Interestingly enough, the region  $qd_A \lesssim 10$  is the one accessible in dynamical light scattering experiments on colloidal systems.

The decrease of  $\hat{h}_{AA}(q)$  results, together with increasing plateau values, in a flattening of the  $\hat{\phi}_{AA}(q, t)$ -versus- $\log t$  curve within the time window that can be described by the leading-order asymptotic term, Eq. (3.49a). This effect is further emphasized since the time scale  $t_0$  decreases with

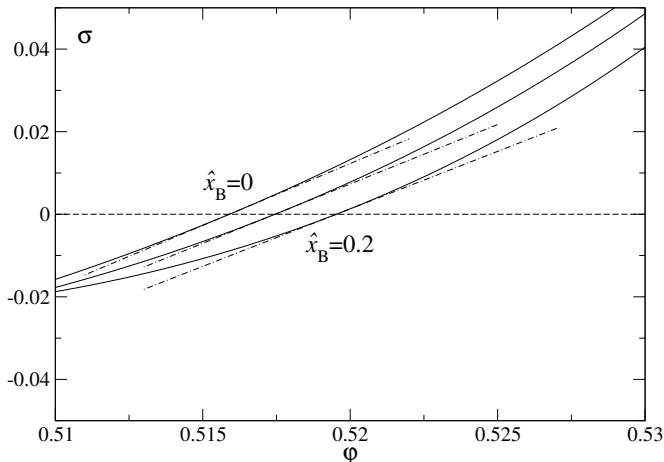


FIGURE 4.20. Distance parameter  $\sigma$ , Eq. (3.36), as a function of  $\varphi$  for binary HSM with  $\delta = 0.6$  and  $\hat{x}_B = 0, 0.1$ , and  $0.2$  as indicated by the labels. The chain-dotted lines are leading-order asymptotes,  $\sigma = C\varepsilon$ ,  $\varepsilon = (\varphi - \varphi^c)/\varphi^c$ ; values given in the text.

increasing  $\hat{x}_B$ , as noted above. The resulting slower relaxation onto the plateau can in principle be compensated by a decrease of the plateau value. In general, this is not the case, as was discussed in connection with Figs. 4.5 and 4.7. But for values around the first peak in  $S_{AA}(q)$ ,  $qd_A \approx 2\pi$ , both the increase in  $\hat{f}_{AA}^c(q)$  and the decrease of  $\hat{h}_{AA}(q)$  are rather small, *cf.* Figs. 4.7 and 4.19, so that in this case, the effect of slower initial relaxation is expected to be negligible. Indeed, this was observed in experiment (Fig. 7 of Ref. [8]), where for  $qd_A \approx 7$ , faster relaxation towards the plateau connected with a decrease in  $\hat{f}_{AA}^c(q)$  was observed. The latter decrease can be anticipated but is not resolved in the wave-vector discretisation used here. We conclude that the effect (iii) of Ref. [8] is, at least in part, explained by the change of the critical amplitudes upon mixing. At the same time, Fig. 4.19 suggests that this effect is general only for the wave-vector region of the light-scattering experiments.

Fig. 4.20 shows the distance parameter  $\sigma$  according to Eq. (3.36), evaluated for  $\delta = 0.6$  and different  $\hat{x}_B$ . The general trend is the same found

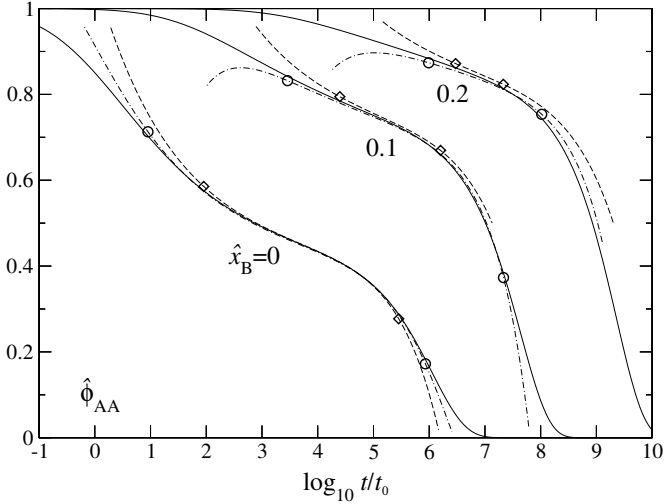


FIGURE 4.21. Asymptotic description of the normalised correlation functions  $\hat{\phi}_{AA}(q, t)$  for  $qd_A = 5.4$ ,  $\varphi = 0.515$ ,  $\delta = 0.6$  and different  $\hat{x}_B$  as indicated. The solid lines are the full solutions reproduced from Fig. 4.13, but plotted as functions of  $t/t_0$ . The time scale  $t_0$  is 0.4408, 0.2026 and 0.1385 for  $\hat{x}_B = 0$ , 0.1, and 0.2, respectively. Dashed and chain-dotted lines show the results of Eq. (3.49) up to order  $|\sigma|^{1/2}$  and  $|\sigma|$ , respectively. The diamonds (circles) mark where the asymptotic solution up to leading (next-to-leading) order deviates by 0.01 from the normalised correlator. Curves for  $\hat{x}_B = 0.1$  (0.2) have been translated along the  $t$ -axis by 2 (4) decades for clarity.

also in the study of asymptotic expansions for the one-component system [5]. Close to the transition, one can restrict  $\sigma$  to its first-order Taylor term,  $\sigma = C\varepsilon$ , which relates  $\sigma$  to the variation in external control parameters,  $\varepsilon = (\varphi - \varphi^c)/\varphi^c$  in this case. These linear laws are also shown in Fig. 4.20, with coefficients  $C = 1.545$  (1.489, 1.447) for  $\hat{x}_B = 0$  (0.1, 0.2). The values of  $C$  are all rather similar; in other words, there is (in leading order) no variation upon mixing in  $\sigma$  one would not guess from the transition diagram, Fig. 4.1.

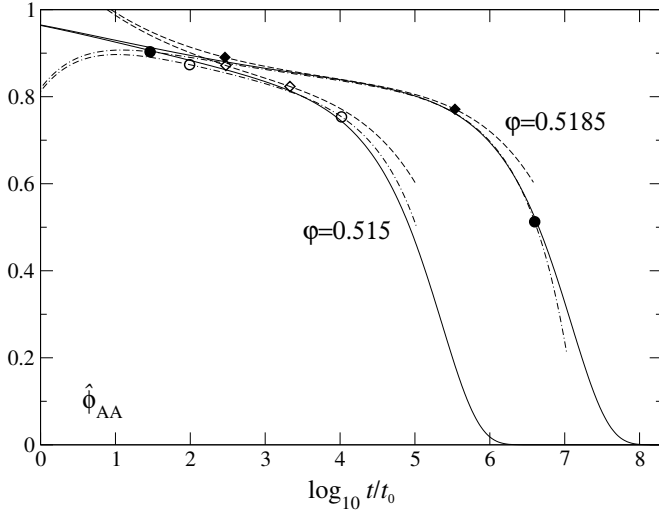


FIGURE 4.22. Asymptotic description of the normalised correlation functions  $\hat{\phi}_{AA}(q, t)$  for  $qd_A = 5.4$ ,  $\delta = 0.6$  and  $\hat{x}_B = 0.2$  at different  $\varphi$  as indicated. Lines and symbols as in Fig. 4.21; open symbols refer to  $\varphi = 0.515$  and closed ones to  $\varphi = 0.5185$ .

Let us now corroborate the above discussion of the general mixing effect by demonstrating that the asymptotic description indeed is able to describe much of the relaxation curves discussed before. To this end, we compare in Fig. 4.21 the asymptotic result with the complete solution for the  $\hat{\phi}_{AA}$  correlator. The case  $\hat{x}_B = 0$  shows a typical scenario for the one-component system. There the leading order describes over three decades in time of the solution (indicated by diamonds). This window of the analytic description is expanded by incorporating the next-to-leading order by about one decade both at short and at long times (marked by circles). For  $\hat{x}_B = 0.1$  and  $\hat{x}_B = 0.2$ , the range of validity for both the leading and the next-to-leading order shrinks; at  $\hat{x}_B = 0.2$  it is, including both orders, only about two decades. But this can be understood if one remembers that the distance from the critical point has increased by changing from  $\hat{x}_B = 0$  to  $\hat{x}_B = 0.2$  with fixed total packing fraction. We get  $\sigma = -0.0027$  ( $-0.0066, -0.011$ ) for  $\hat{x}_B = 0$  ( $0.1, 0.2$ ), *i.e.* an increase in  $\sigma$  by about a factor 4. Thus the decreasing

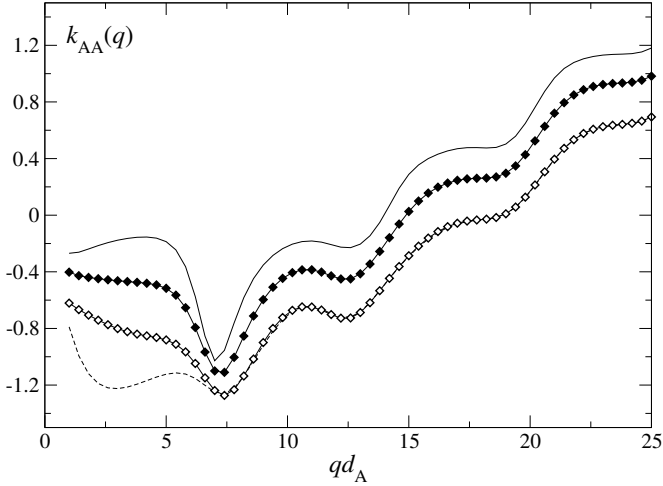


FIGURE 4.23. AA elements of the correction amplitudes  $\mathbf{k}(q) = \mathbf{K}(q)\mathbf{H}(q)^{-1}$  for a binary HSM with size ratio  $\delta = 0.6$  and compositions  $\hat{x}_B = 0$  (solid line), 0.1 (filled symbols), and 0.2 (open symbols). The dashed line shows the result for  $\hat{x}_B = 0.2$  with different normalisation,  $\tilde{k}_{AA} = K_{AA}(q)/H_{AA}(q)$ .

quality of the asymptotic description is merely due to a larger separation parameter  $\sigma$ . This shall be demonstrated explicitly by Fig. 4.22, where the  $\hat{x}_B = 0.2$  case is shown again together with a relaxation curve evaluated at higher packing fraction, *i.e.* closer to the transition. We chose  $\varphi = 0.5185$  in order to get a separation parameter,  $\sigma = -0.0028$ , that is similar in magnitude to that found for the  $\varphi = 0.515$ ,  $\hat{x}_B = 0$  case. Indeed, the ranges of validity in these two cases are similar.

Precisely speaking, the relevant quantity specifying the range of validity of the asymptotic expansion is not the size of the logarithmic time interval, but the size of the decay interval  $|\hat{\phi}_{AA}(q, t) - \hat{f}_{AA}^c(q)|$ . Figures 4.21 and 4.22 demonstrate that the asymptotic formulæ are able to describe the structural relaxation in  $\hat{\phi}_{AA}(q, t)$  towards the plateau below 0.70 (0.85, 0.90) for  $\hat{x}_B = 0$  (0.1, 0.2). This includes the regime where the effect of slower relaxation towards the plateau has been found.

For completeness, let us finally demonstrate the change of the correction amplitudes  $\mathbf{K}(q)$  upon mixing. We have checked that the values of  $\bar{\mathbf{K}}(q)$

show the same qualitative behaviour upon mixing. Fig. 4.23 shows the AA element of  $\mathbf{k}(q) = \mathbf{K}(q)\mathbf{H}(q)^{-1}$ , plotted in this way to ease comparison with the published results for the one-component system (Fig. 2 of [5]). The solid line in Fig. 4.23 shows the one-component result evaluated with the asymptotic expansion of Sec. 3.2, *cf.* Eqs. (3.24) and (3.25). This curve is qualitatively the same as the corresponding one in Ref. [5], but at large  $q$  some differences in magnitude can be seen. This is due to the fact that the used asymptotic expansions differ in their treatment of changes in  $\mathcal{O}(\sigma)$  of the structure factor. The filled and open diamonds in Fig. 4.23 demonstrate the values of  $k_{AA}(q)$  for mixtures with  $\delta = 0.6$  and  $\hat{x}_B = 0.1$  and  $\hat{x}_B = 0.2$ , respectively. For  $q$  below the first zero in the one-component  $k(q)$ , we find that the magnitude of  $k_{AA}(q)$  increases. The effect is strongest for  $qd_A \lesssim 2\pi$ . Note that in this region, the shape of the curves are normalisation-dependent. To exemplify this, let us add for  $\hat{x}_B = 0.2$  the values  $\hat{k}_{AA}(q) = K_{AA}(q)/S_{AA}(q)$ , which is the normalisation used in the discussion above. To compare with the other curves in Fig. 4.23, we plot  $\tilde{k}_{AA} = \hat{k}_{AA}(q)/\hat{h}_{AA}(q)$  as the dashed line. The two different normalisations agree very well for  $q$  larger than the first peak in the structure factor. But for small  $q$ ,  $\tilde{k}_{AA}(q)$  is significantly larger in magnitude. This again is a manifestation of the fact that the off-diagonal matrix elements of the structure factor are important for small  $q$ . The large magnitude of  $\tilde{k}_{AA}(q)$  as compared to the one-component result furthermore corroborates that the corrections to the leading order asymptotics become more important upon mixing. This agrees with the finding that the expected power-law relaxation onto the plateau in the correlators shown in Fig. 4.13 is less easily made out for higher  $\hat{x}_B$ .

## Comparison With Experiment

Having established the qualitative predictions MCT makes for the binary HSM with size ratios  $\delta \geq 0.6$ , we will in this chapter proceed with a quantitative comparison to recent dynamic light scattering experiments on colloidal suspensions of hard-sphere like particles. Since the study presented in the preceding chapter was in a large part stimulated by these experiments, a few words about the experimental setup might be in order. After that, the findings for size ratio  $\delta = 0.6$  will be presented, which constitutes the main part of this discussion. Some results, albeit of less detailed quality, are available for  $\delta = 0.8$ , and they will be discussed at the end of this chapter.

Dynamic light scattering (DLS) is a popular technique in studying colloidal suspensions. It probes fluctuations in the index of refraction of a complex fluid on a length scale of the inverse scattering vector,  $q^{-1}$ . In colloidal suspensions, these fluctuations are dominated by those caused by the motion of the colloidal particles. In the limit of single-scattering events only, the measured signal can thus be used to reconstruct their motion in terms of the density autocorrelation function of the colloidal particles.

Industrial applications set aside, one can typically adjust the solvent's refractive index to closely match the one of the suspended particles, in order to arrive at single scattering even for dense suspensions. Such index matching has been the case in the previous light scattering studies on glass-forming suspensions. On the other hand, hard-sphere like colloids consisting of a PMMA core and a stabilising surface layer have an interesting property: their refractive index can be changed to some extent by varying the temperature [118]. Even if the actual change in refractive index is minute, the resulting change in the particles' form factors  $b_\alpha(q)$  can, for nearly index-matched suspensions, easily reach

some orders of magnitude, *cf.* as an example Eq. (4.9). In Ref. [8], a change from  $T = 6^\circ\text{C}$  to  $26^\circ\text{C}$  created a variation of up to a factor of  $10^3$  in  $b_\alpha(q)$ . Still, the dynamical properties remain unchanged; only that the suspension loses index matching and becomes turbid.

DLS from turbid media has been developed in the past twenty years using so-called cross-correlation spectroscopy. The general idea is to analyse two different probe beams that are adjusted to the same scattering volume. Any scattering event within this volume will produce correlated signals in both beams. Since any further scattering that occurs to either of the two beams thereafter serves to decorrelate the two signals, one can reconstruct from the cross correlation between the two detectors the singly scattered signal. As the two incident probe beams, one can take two laser beams of different colour, hence the name two-colour dynamic light scattering (TC-DLS) [119–121]; or one adjusts a splitted laser beam to scatter into two orthogonal scattering planes, the so-called 3D-DLS [122, 123]. We refer to Ref. [124] for a review of these multiple-scattering suppression techniques.

The two-colour technique has been put into use for studying the colloidal glass transition quite recently by van Meegen and coworkers [125]. Together with the possibility of changing the particles' scattering amplitudes over a wide range, it combines to a powerful method for investigating the colloidal dynamics of the single species in a colloidal mixture, *i.e.* to extract from it the complete matrix of partial intermediate scattering functions. One needs for a binary mixture three sets of measured correlation functions  $\phi^m(q, t)$  corresponding to three independent choices of the  $b_\alpha(q)$  in Eq. (4.6). In principle, the mapping  $\Phi_{\alpha\beta}(q, t) \mapsto \{\phi^m(q, t)\}$  defined by this equation can then be inverted for the three independent  $\Phi_{\alpha\beta}(q, t)$  to give an ideally suited starting point for comparison with theory. The inversion has been carried out only recently in an outstanding experiment [8] with which we will compare our MCT results in the following.

## 1. Binary Mixtures: Melting of the Glass

Before embarking on the fits in detail, let us clarify some basic aspects of such comparisons. In principle, MCT is a parameter-free theory, once

the static structure input is known. Yet the theory is, after all, approximate, and this reintroduces a small number of qualitatively unimportant fit parameters.

Experimental data in Ref. [8] have been reported as functions of dimensionless time  $t/\hat{\tau}$ ,  $\hat{\tau} = d_A^2/(24D_A^s)$ . Here,  $D_A^s$  is the measured free (short-time) diffusion constant of the large particles. The same scaling has been applied to the theoretical curves, where, however, the treatment of the regular part of the memory kernel is incorrect and hydrodynamic interactions (HI) are neglected. The effect of the latter on the short-time diffusion has been studied extensively [126, 127]; it is usually incorporated via the hydrodynamic factor  $H(q)$ ,  $D_A^s = D_A^0 H(q \rightarrow \infty) S^{-1}(q \rightarrow \infty)$  for one-component systems. There is as yet no decisive theory for the influence of HI at high densities. They have been argued to be important even for the long-time dynamics [128], although in the MCT approach it seems natural to just attribute to them the specialties of the short-time dynamics which do not influence the dynamics on long time scales up to a common prefactor [129]. From calculations of  $H(q)$  for a one-component system [130] we estimate in this sense that a correction  $\hat{\tau}/\hat{\tau}_{\text{MCT}}$  of the order of 4 to 10 can be justified. For the fits presented below, we were able to fix this ratio to about 4.8 (6) for  $\hat{x}_B = 0.2$  and 0.1 (0.05) with  $D_\alpha^0 \propto 1/d_\alpha$ .

It is well known that the MCT prediction for the numerical value of the critical packing fraction in the hard-sphere system,  $\varphi^c \approx 0.516$ , deviates from the experimental result,  $\varphi_g \approx 0.575 \pm 0.005$  [11], by about 10%. Since the relevant parameter close to the transition is the distance to it,  $\varepsilon = (\varphi - \varphi^c)/\varphi^c$ , one allows for a shift between experimentally obtained packing fraction values and those used for the MCT calculations in such comparisons. In practice, we have treated the packing fraction as a fit parameter at first and checked then that the obtained values are indeed compatible with a simple shift. Note also that the experimental value suffers from some uncertainty in our case, since there each particle species has in itself a small inherent polydispersity. This polydispersity was about 6% for the large spheres and about 9% for the small ones; for the latter it was so high as to completely inhibit crystallisation of the corresponding one-component system [8]. While this allows for a better study of glass-transition phenomena, it also introduces some uncertainty in determining the packing contribution, since the latter

is typically gauged by comparing the crystallisation density with the computer-simulation result.

In addition, a 10% deviation in the wave vector  $q$  will be allowed for. The comparison of plateau values read off from the data with the  $\hat{f}_{\alpha\beta}^c(q)$  determined from theory suggests this. Such a small offset between experimental and theoretical  $q$  values has been already noted for (effectively) one-component hard-sphere like colloids, where it has been attributed to the above mentioned deviation in the critical packing fraction that in turn causes the peak positions in  $S^c(q)$  to be somewhat offset [131]. A comparison of MCT ‘ $\alpha$ ’ scaling functions with computer-simulation results for a one-component system showed a similar adjustment in  $q$  to be successful [132].

Note that in all the comparisons shown below, we did not perform a least-square or similar fit to the experimental data; all values for the fit parameters given are to be understood as estimates. We believe this is sufficient since we merely want to demonstrate that the theory can reproduce experimental data (semi-)quantitatively with reasonable values of the input parameters.

The numerical results of MCT are plotted on top of the experimental data of Ref. [8] in Figs. 5.1, 5.2, and 5.3 for  $\hat{x}_B = 0.2, 0.1,$  and  $0.05,$  respectively. All systems have size ratio  $\delta = 0.6,$  and the total packing fractions are varied as indicated in the captions. In all cases, the scaling of the  $t$  axis was done as explained above. The wave vector was adjusted from the experimental value of  $q^{\text{exp}}d_A = 6.0$  to  $qd_A = 5.4,$  in order to match the plateau values of the AA and AB correlators, in agreement with what was explained above.

Let us start the discussion with the AA and AB correlators. Here, satisfying agreement of the MCT curves with experiment is found over the whole experimentally accessible range, including about 6 orders of magnitude in time. Some small deviations at short times,  $t/\hat{\tau} \lesssim 1,$  can be seen and are to be expected due to the improper treatment of the short-time relaxation in MCT. Given this and the expectation that in this regime, hydrodynamic interactions could manifest themselves, the agreement of the fits even at short times is remarkably good. In the AB correlator for  $\hat{x}_B = 0.20$  and at lower  $\varphi,$  some systematic deviations can be seen for long times. They indicate that in the experiment, the coupling of the ‘ $\alpha$ ’ relaxation times of the different correlators is not as

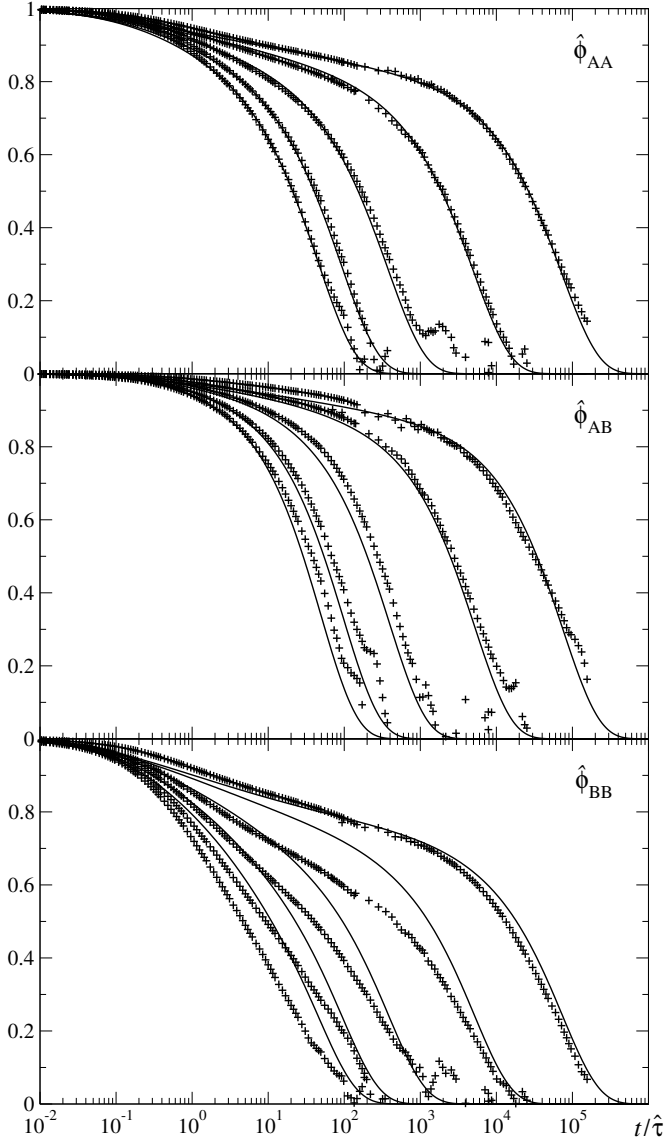


FIGURE 5.1. The normalised correlation functions  $\hat{\phi}_{\alpha\beta}(q, t) = \Phi_{\alpha\beta}(q, t)/S_{\alpha\beta}(q)$  for a binary hard-sphere mixture with  $\delta = 0.6$  and  $\hat{x}_B = 0.20$ . Crosses are experimental results from Ref. [8] for  $qd_A = 6.0$  and  $\varphi^{\text{exp}} = 0.51, 0.53, 0.55, 0.57,$  and  $0.58$  (from left to right). Solid lines are the MCT results for  $qd_A = 5.4$  and  $\varphi^{\text{MCT}} = 0.46, 0.475, 0.497, 0.51, 0.516$ .

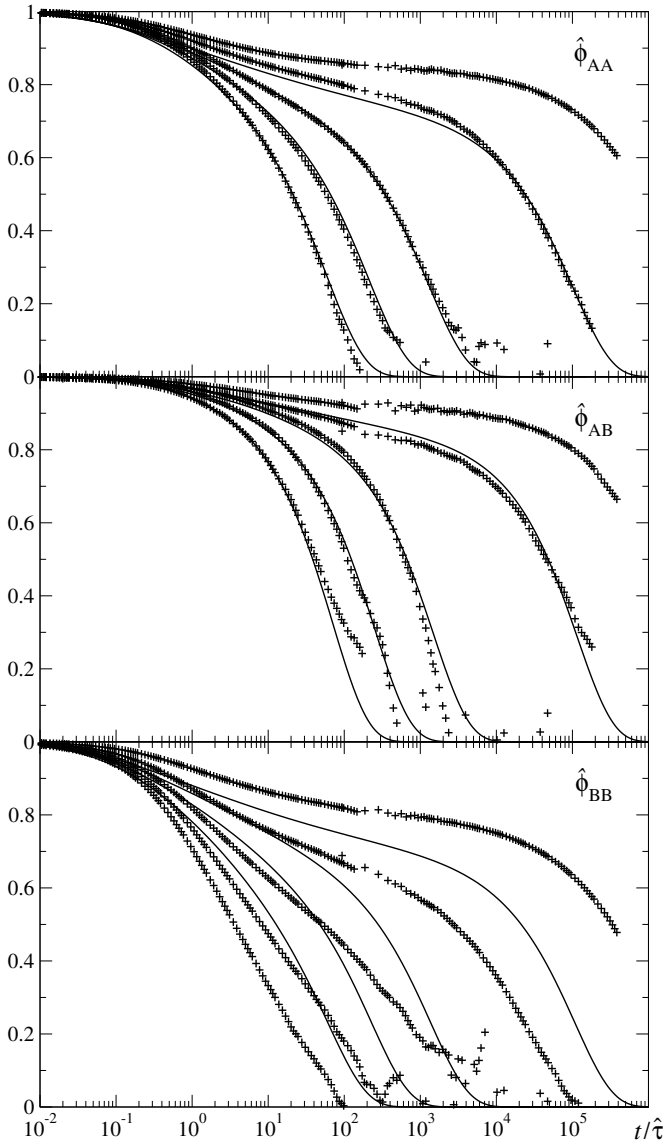


FIGURE 5.2. Experimental and MCT results for the hard-sphere mixture with  $\delta = 0.6$  and  $\hat{x}_B = 0.10$ , analogous to Fig. 5.1. Values for the packing fraction  $\varphi$  in experiment (theory) are 0.51 (0.47), 0.53 (0.49), 0.55 (0.504), 0.57 (0.515), and 0.58 (from left to right).

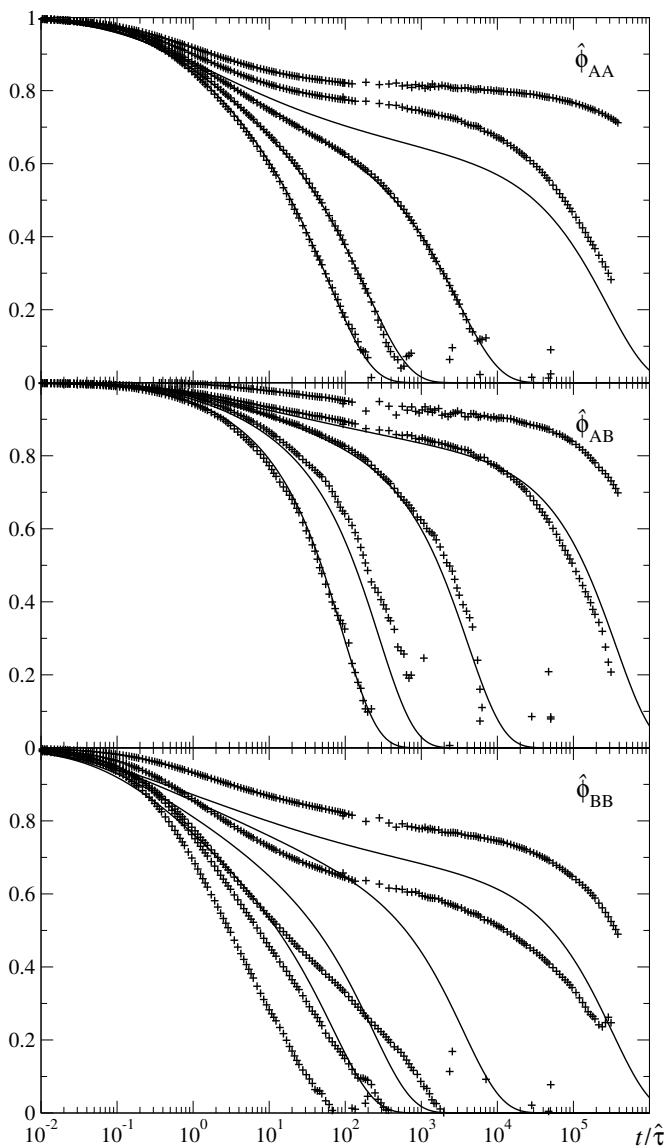


FIGURE 5.3. Experimental and MCT results for the hard-sphere mixture with  $\delta = 0.6$  and  $\hat{x}_B = 0.05$ , analogous to Fig. 5.1. Packing-fraction values  $\varphi$  in experiment (theory) are, from left to right, 0.51 (0.47), 0.53 (0.488), 0.55 (0.507), 0.57 (0.515), and 0.58.

nically fulfilled as the theory suggests. These errors show up in the AB correlator since our fit is biased to reproduce best the AA correlator for which errors should be smallest<sup>1</sup>. Closer to the glass transition, the ‘ $\alpha$ ’ time scales of the AA and AB correlators agree better in experiment, confirming the scaling prediction of MCT. We do not put too much emphasis on the mentioned deviation, since it seems to be absent for  $\hat{x}_B = 0.10$  and  $\hat{x}_B = 0.05$ , where in the latter case the decay of the AB correlator obviously shows some noise in the data.

It is remarkable that the fit quality seems to be better in the mixture containing more smaller particles, *i.e.* showing more pronounced mixing effects. Our fit becomes noticeably worse for smaller  $\hat{x}_B$ , and for  $\hat{x}_B = 0.10$  and  $\hat{x}_B = 0.05$ , we have not been able to convincingly fit the data for the highest measured packing fraction at all. The problems stem from an increasing discrepancy in the plateau values that cannot be accounted for by any reasonable adjustment of  $q$ . We will come back to this issue below.

For the BB correlator, no satisfying fit was possible in general. In the case  $\hat{x}_B = 0.2$  and  $\varphi^{\text{exp}} = 0.58$ , the agreement between experiment and MCT is again extremely good, but this is the only case among all others studied. Since the three correlation functions are not independent from one another but merely different elements of the same matrix, the deviations in the BB case deserve a more detailed investigation. This shall be carried out in the following for the  $\hat{x}_B = 0.2$  case; at the two other compositions, qualitatively the same picture arises.

Fig. 5.4 contains the same fit as in Fig. 5.1, but instead of the partial scattering functions, the measured correlation functions  $\phi^{\text{m}}(q, t)$  for three temperatures have been plotted. Each temperature belongs to a different combination of scattering amplitudes  $b_\alpha(q)$  in the weighted sum of Eq. (4.6), thus three temperatures provide enough information to extract information about the three partial correlation functions. Using Eq. (4.6) together with the scattering amplitudes taken from the experiment, we have replotted the MCT fits to give theoretical results for the different experimental temperatures. One notices again close agreement for two of the three temperatures, while the  $T = 6^\circ\text{C}$  results differ significantly. This temperature corresponds to a scattering signal that is dominated by the minority population of the small particles, as

---

<sup>1</sup>S. R. Williams, priv. comm.

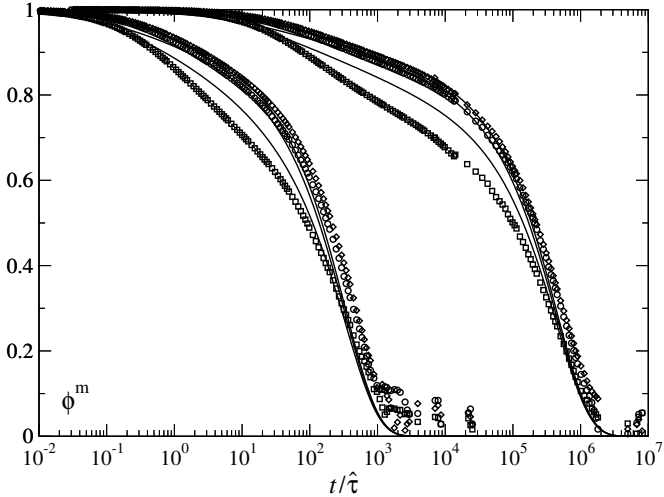


FIGURE 5.4. Correlation functions  $\phi^m(q, t)$  for the binary mixture with  $\delta = 0.6$ ,  $\hat{x}_B = 0.2$ , and  $qd_A = 6.0$  as measured in experiment, Ref. [8], for different temperatures controlling different combinations of scattering amplitudes  $b_\alpha(q)$ . Temperatures are  $T = 6^\circ\text{C}$  (squares),  $T = 14.5^\circ\text{C}$  (diamonds), and  $T = 26^\circ\text{C}$  (circles). The solid lines are the MCT fits shown in Fig. 5.1, weighted according to Eq. (4.6) with the  $b_\alpha(q)$  taken from experiment. The left set of curves refers to  $\varphi^{\text{exp}} = 0.55$ ; the right set refers to  $\varphi^{\text{exp}} = 0.57$  and has been shifted by two decades along the  $t$  axis.

can be inferred from Fig. 5.5. Fig. 5.4 allows to better judge the error of the fit than does the representation of Fig. 5.1, since it refers to actually measured intensities. Looking at a fixed  $t$ , one estimates from Fig. 5.4 a deviation of less than about 10% for the  $T = 6^\circ\text{C}$  curves. This deviation shows no significant dependence on  $\varphi$  for the cases we checked.

If one assumes the Smoluchowski description for the colloidal suspension to be valid at long times, the positive definiteness of the matrix  $\Phi(t)$ , *cf.* Sec. 3.1, imposes restrictions on its different elements. In particular, the consistency of the data with the Smoluchowski assumption can be checked by calculating the two eigenvalues  $e_\pm(q, t)$  of the  $2 \times 2$  matrix,

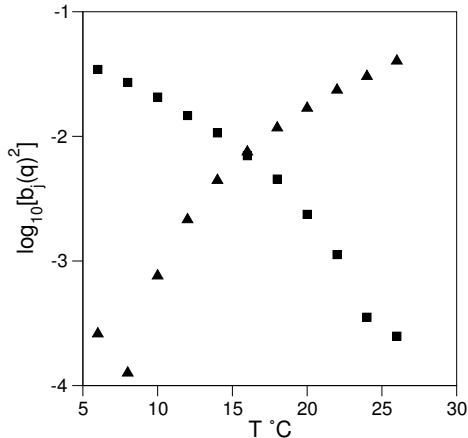


FIGURE 5.5. Single-particle form factors  $b_j(q)^2$  versus temperature corresponding to the data shown in Fig. 5.4. The wave vector is  $qd_A = 6.0$ ; triangles are for the large particles, squares for the small ones. Reproduced from Fig. 2(a) of Ref. [8].

which both need to be positive for any given time  $t$  and wave vector  $q$ . A plot of  $e_{\pm}^{\text{exp}}(t)$  for  $qd_A = 6.0$  using the experimental data for  $\Phi_{\alpha\beta}(t)$  is presented in Fig. 5.6. A calculation of these eigenvalues requires knowledge of the (unnormalised)  $t \rightarrow 0$  values  $\mathcal{S}(q)$ . In constructing Fig. 5.6, we have used the corresponding values obtained from the MCT fit, *i.e.* the Percus-Yevick result at the  $\varphi^{\text{MCT}}$  that was fitted to the  $\varphi^{\text{exp}}$  data in Fig. 5.1. We have checked that the results do not qualitatively depend on the  $\mathcal{S}(q)$  values chosen by varying the packing fraction used in the Percus-Yevick formula over the range of packing fractions shown.

One clearly notices that for long times,  $t/\hat{\tau} \gtrsim 10$ , the experimental data exhibits eigenvalues  $e_{-}^{\text{exp}}(t) < 0$ , in violation of positive definiteness of  $\Phi(t)$ . Since it is commonly believed that at such long times, the Smoluchowski equation provides the correct description of the dynamics of colloidal suspensions (*cf.* Sec. 2.1.3), this hints towards a possible experimental error as the reason for the discrepancy. Note that the violation is only of the order of 5%; it is about as large as the deviation

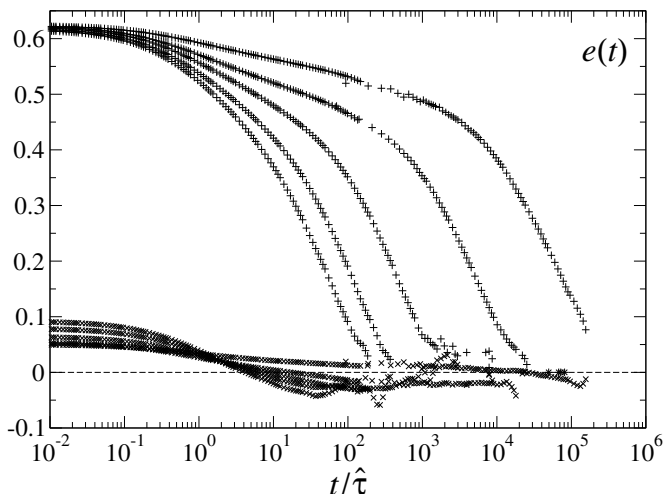


FIGURE 5.6. Eigenvalues  $e_{\pm}(t)$  of the experimentally measured matrix of partial correlation functions,  $\Phi(q, t)$ , at  $qd_A = 6.0$  and  $\hat{x}_B = 0.2$ , for packing fractions  $\varphi$  as given in Fig. 5.1. Plus signs denote the larger eigenvalue  $e_+(t)$ , crosses the smaller one  $e_-(t)$ . See text for details.

seen in Fig. 5.4 and probably well inside the error bars for the BB-dominated measurements<sup>2</sup>. Clearly, a fully detailed error analysis of the experimental data would be needed to clarify this matter further. But such analysis appears to be a formidable task on its own and has not been performed up to now.

The mapping of experimentally determined packing fractions,  $\varphi^{\text{exp}}$ , versus those used in the fits of Figs. 5.1–5.3,  $\varphi^{\text{MCT}}$ , is explored in Fig. 5.7. Within expected error margins, the data are consistent with applying a simple shift,  $\varphi^{\text{exp}} = \varphi^{\text{MCT}} + \Delta\varphi$ , with  $\Delta\varphi \approx 0.05$ . Such a shift is exemplified in Fig. 5.7 through the dashed line, and the dotted lines correspond to varying  $\Delta\varphi$  by 10%. This underlines the MCT picture that the quantity governing the dynamics close to the glass transition is mainly the distance to it, in this case ( $\varphi - \varphi^c$ ). One notices a slight trend of  $\varphi^{\text{exp}} - \varphi^{\text{MCT}}$  becoming larger for  $\hat{x}_B = 0.2$  than for the smaller

<sup>2</sup>S. R. Williams, priv. comm.

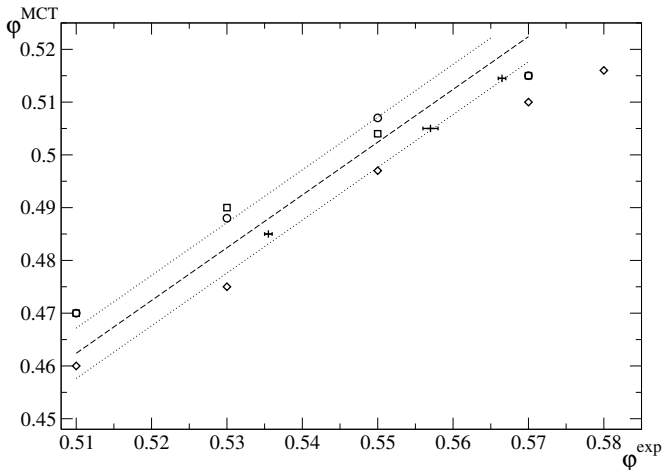


FIGURE 5.7. Mapping of  $\varphi^{\text{MCT}}$  to  $\varphi^{\text{exp}}$  values used in the MCT fits to the data of Ref. [8] presented in Figs. 5.1 (diamonds), 5.2 (squares), and 5.3 (circles). The dashed line with slope unity represents a simple shift,  $\varphi^{\text{exp}} = \varphi^{\text{MCT}} + \Delta\varphi$ , with  $\Delta\varphi = 0.0476$ ; the dotted lines indices 10% variation in  $\Delta\varphi$ . The crosses with horizontal error bars denote values used in the fits to data of Ref. [103], *cf.* Fig. 5.10.

values of  $\hat{x}_B$ . Since a free fit of  $\varphi^{\text{MCT}}$  essentially serves to reproduce the ‘ $\alpha$ ’ time scale of the experiment, this indicates that, at fixed  $\varphi^{\text{exp}}$ , the experimental ‘ $\alpha$ ’ time scale shortens faster with increasing  $\hat{x}_B$  than the one of the MCT calculations. In Sec. 4, we showed that the qualitative trend of faster decay upon mixing is reproduced within MCT; the results here suggest that the magnitude of this ‘plasticisation’ effect is even underestimated in the theory. Altogether, Fig. 5.7 reassures that the fits of Figs. 5.1–5.3 are reasonable in the sense that the qualitative changes of the relaxation times upon mixing found in the experiment are reproduced by the theory and not put in “by hand” through a fit of the packing fraction values.

Up to now, only one wave vector  $q$  has been investigated. But among the virtues of the DLS setup is the ability to vary  $q$  within the range of the first sharp diffraction peak in  $S(q)$  and below. Fig. 5.8 shows the experimental results for some wave vectors also analyzed in Ref. [8] for

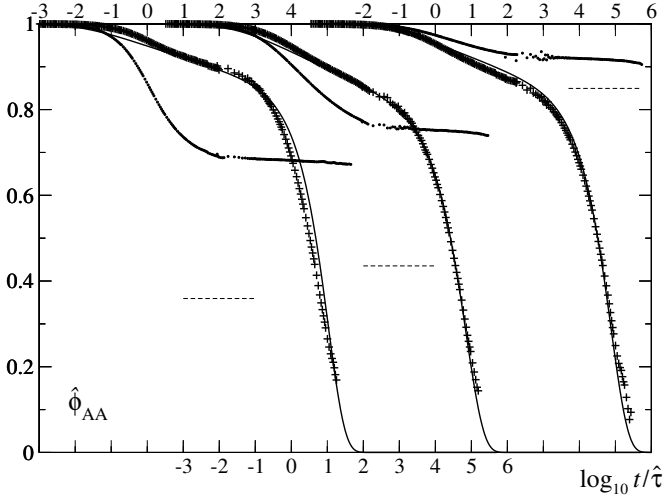


FIGURE 5.8. Plus symbols denote the experimentally measured normalised partial correlation functions  $\hat{\phi}_{AA}(q, t)$  from Ref. [8] for a hard-sphere mixture with  $\hat{x}_B = 0.2$  and  $\varphi^{\text{exp}} = 0.58$  at wave vectors  $qd_A = 3.0$  (upper left axis), 6.0 (lower axis), and 7.2 (upper right axis), from left to right. The curves for different wave vectors have been translated along the  $t$  axis by 4 decades for enhanced clarity. The solid lines are MCT fits, using  $\varphi^{\text{MCT}} = 0.515$  and  $qd_A = 3.8, 5.4,$  and  $7.0$ , respectively. Filled circles show the results of Ref. [8] for the one-component system,  $\hat{x}_B = 0$ . The dashed lines indicate the corresponding MCT results for  $f^c(q)$  in the one-component system.

the AA correlator in the  $\hat{x}_B = 0.2$  case, together with corresponding MCT fits. We have chosen the same correspondence for the packing fractions,  $\varphi^{\text{exp}} = 0.58$  and  $\varphi^{\text{MCT}} = 0.515$ , as in Fig. 5.1. The wave vector values were again allowed to deviate such that the plateau values match; we get  $qd_A = 3.8$  and  $7.0$  for the experimental values  $q^{\text{exp}}d_A = 3.0$  and  $7.2$ , respectively, *i.e.* the adjustment is again of the same size as before. The error is largest for  $qd_A \approx 3$ , which may hint towards larger deviations for small  $q$ . Note that the MCT calculations have been done on a discrete grid for the wave vectors, *cf.* Sec. 4.1. Thus, there remains

a small error of the order of  $\Delta q/2 = 0.2$  for the determination of the optimal  $q$  value in the fits.

Fig. 5.8 also shows some results for the one-component case,  $\hat{x}_B = 0$ . From the above discussed deterioration of fit quality with decreasing  $\hat{x}_B$ , one extrapolates that a similar fit for the one-component system will fail due to the measured  $f^c(q)$  being too high. This is shown in Fig. 5.8 by the filled circles, which are the experimental data for  $\hat{x}_B = 0$  from which one easily reads off plateau values  $f(q)$ . Since  $\varphi = 0.58$  is close to the experimental glass transition, one can expect that these  $f(q) \approx f^c(q)$ . They clearly are incompatible with the MCT result for  $f^c(q)$ , shown as dashed lines in Fig. 5.8. The origin of this discrepancy is likely to be the small polydispersity remaining in the larger species, as we shall discuss in the following. To begin with, let us point out that the polydisperse effective one-component systems used in experimental studies seem to be poorly specified. While from the one-component data used in the present study, one reads off  $f^c(qd=6) \approx 0.8$ , formerly published data indicates  $f^c(qd=6) \approx 0.56$  [131], in better agreement with the one-component MCT calculation, giving  $f^c(qd=6) \approx 0.56$ . But note that a small variation of  $q$  around  $qd \approx 6$  will induce large changes in  $f^c(q)$ . For a slightly larger wave vector, one extracts the values  $f^c(qd=7) \approx 0.78$  [131],  $f^c(qd=7) \approx 0.87$  [133], and  $f^c(qd=7.2) \approx 0.91$  [8] from the different experiments. Since in the experiments, due care has been taken to ensure correct averaging even over nonergodic samples, see Refs. [131, 134] and references therein, we assume that the discrepancies might be due to different particle size distributions present in the different samples. From the discussion in Sec. 4 and Fig. 4.8 in particular, one expects that polydispersity generically increases  $f^{m,c}(q)$  at small  $q$  with respect to the one-component system, assuming scattering amplitudes that vary qualitatively similar to Eq. (4.8).

To shed more light on the influence of polydispersity, consider a simplistic model for a polydisperse particle size distribution. Starting from the binary HSM, we split each of the two species' population into halves, denoted by  $A \mapsto aa'$ , and  $B \mapsto bb'$ . Now we let the diameter of the  $a'$  and  $b'$  particles shrink by  $\mu \cdot d_A$ . Thus we end up with a four-component mixture with densities and radii of the species  $n_a = n_{a'} = n_A/2$ ,  $d_a = d_A$ ,  $d_{a'} = d_A(1 - \mu)$ , and  $n_b = n_{b'} = n_B/2$ ,  $d_b = d_B$ ,  $d_{b'} = d_B(1 - \mu/\delta)$ . Here, the quantities with subscripts A and B are determined as for the binary HSM discussed above. Of interest then are the averages

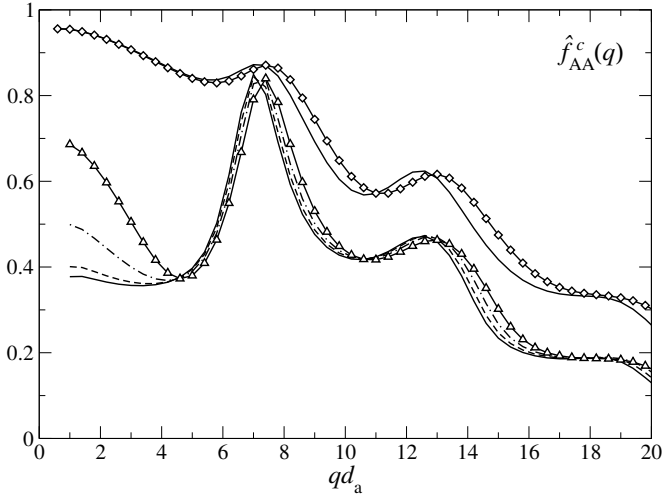


FIGURE 5.9. Solid lines are the critical glass form factors  $\hat{f}_{AA}^c(q) = F_{AA}^c(q)/S_{AA}^c(q)$  of binary hard-sphere mixtures with size ratio  $\delta = 0.6$  and packing contribution of the small spheres  $\hat{x}_B = 0$  (lower curve) and  $0.2$  (upper curve). The lines with symbols are results for a model where half of each species' particles are replaced by ones with a diameter that is smaller by  $\mu = 0.1$ , starting from the binary mixture with  $\hat{x}_B = 0$  (triangles) and  $\hat{x}_B = 0.2$  (diamonds), respectively. For the  $\hat{x}_B = 0$ , results for  $\mu = 0.02$  (dashed line) and  $\mu = 0.05$  (chain-dotted line) are also shown. See text for details.

over the new sub-species, *e.g.*  $F_{AA}(q) = \sum_{\alpha,\beta \in \{a,a'\}} F_{\alpha\beta}(q)$ . Such a representation of the continuous particle size distribution found in real polydisperse suspensions by a series of discrete peaks is quite common in the literature [95, 135–137].

Exemplary results for the simple polydispersity model are exhibited by Fig. 5.9 which plots the large particle's Debye-Waller factor at the glass-transition point,  $\hat{f}_{AA}^c(q) = F_{AA}^c(q)/S_{AA}^c(q)$ . The results for  $\delta = 0.6$  with  $\hat{x}_B = 0$  and  $\hat{x}_B = 0.2$ , shown through the solid lines without symbols, are repeated from above; they represent a monomodal respective bimodal size distribution with no polydispersity in the single species.

The change of the monomodal system's  $f^c(q)$  with increasing polydispersity parameter  $s$  is demonstrated by the dashed and chain-dotted lines, corresponding to  $\mu = 0.02$  and  $\mu = 0.05$ , respectively. Commonly, polydispersity is characterised by the giving the standard deviation  $s$  of the distribution, which evaluates to  $s \approx 0.01$  and  $s \approx 0.026$  in the two cases. Note that these are still quite small values. Still, the critical glass form factors vary notably for  $qd_a \leq 4$ . The increase in  $\hat{f}_{AA}^c(q)$  as  $q \rightarrow 0$  happens due to the same reason as discussed in connection with the binary mixture in Sec. 4. For large  $q$ , the main effect is a shift of the oscillations in  $\hat{f}_{AA}^c(q)$  to higher wave vectors due to the introduction of a smaller length in the system. They could partly, but not completely, be eliminated by taking as a unit of length the mean particle diameter,  $\bar{d} = (d_a + d_a')/2$ , instead of  $d_a$ .

Let us now turn to a discussion of the case  $\mu = 0.1$ , corresponding to  $s \approx 0.53$ , a reasonable value for colloidal glass formers. This case is shown in Fig. 5.9 for both  $\hat{x}_B = 0$  and  $\hat{x}_B = 0.2$ . Now the change of  $\hat{f}_{AA}^c(q)$  for  $\hat{x}_B = 0$  and small  $q$  is even more pronounced. Interestingly enough, the data for  $\hat{x}_B = 0.2$  show almost no change with varying  $\mu$  in this wave vector region; only for large  $q$ , the same shift of the oscillations as noted above is present. Note that the critical packing fraction shows only a slight change,  $\varphi^c \approx 0.5156$  (0.5204) for  $\mu = 0.1$  and  $\hat{x}_B = 0$  (0.2), which has to be compared to  $\varphi_0^c \approx 0.5159$  (0.5195) for  $\mu = 0$ . As expected from Fig. 4.1, the value slightly decreases for the  $\hat{x}_B = 0$  case. It decreases for the  $\hat{x}_B = 0.2$  case, due to the presence of particles with diameters  $d_\alpha < 0.65$ , which in the binary mixtures lead to the plasticising effect discussed above.

The above results suggests that in the small- $q$  region, polydispersity in the constituent species will show greater influence on the monomodal system than on the “binary” mixture. The simple model discussed here does not bring out a noteworthy change of  $\hat{f}_{AA}^c(q)$  in the region  $qd_a \approx 6$  where the light-scattering experiments discussed so far are performed. However, this could be an artefact of the oversimplified model only consisting of two discrete species per polydisperse particle type. The results shown in Fig. 5.9 have to be seen with the findings discussed in connection with Figs. 5.1–5.3 and 5.8 in mind, *i.e.* the success of the fitting procedure for the  $\hat{x}_B = 0.2$  mixture but the decreasing fit quality for smaller  $\hat{x}_B = 0.05$ . Currently, we can only speculate about its origin, but it might be due to the small polydispersity remaining in the larger

species that could present itself more drastically if not overwhelmed by the presence of a significant amount of a smaller species.

## 2. Binary Mixture: Small Size Disparity

To study polydispersity effects, Henderson *et al.* [103] collected data for two hard-sphere suspensions whose particle size distributions were unimodal in one case (system I) and bimodal, with a size ratio  $\delta = 0.8$  and relative strengths  $x_B \approx 0.2$  between the main peaks, in the other (system II). Thus these data can be taken as a test for the ‘anti-plasticising’ prediction of Sec. 4 in the small size disparity case.

To see that such an effect is indeed visible in the experimental data, let us take from Ref. [103] three data sets for each system. We have selected values of the packing fractions to match as closely as possible. Fig. 5.10 shows this data as the plus symbols (system I) and squares (system II). The highest packing fraction shown in the figure is  $\varphi^{\text{exp}} = 0.535$  for system I and 0.536 for system II. While these two values are nearly identical, the dynamics for system II is slower by about one order of magnitude than that of the one-component system. It is unlikely that the slight difference in packing fractions can account for this effect. For the two lower packing fractions, both systems exhibit decay on roughly identical time scales. This agrees with the picture suggested by the MCT results, since one is in these cases too far away from the glass transition to see the effect of changing  $\varphi^c$  upon mixing.

To corroborate the qualitative picture emerging from the data, in Fig. 5.10 we also show fits using Eq. (4.6) with scattering amplitudes from Eq. (4.8) to the system II data, and fits of a one-component calculation to the system I data. For these fits, we use wave vectors close to the first maximum in  $S(q)$ ,  $qd_A = 7.4$  for the two-component fit, and  $qd = 6.6$  for the one-component one. The size ratio for the two-component fit was chosen to be  $\delta = 0.8$ , and the volume fraction  $\hat{x}_B = 0.12$  roughly corresponds to  $x_B \approx 0.2$ . Similar to above, data are transformed to dimensionless time using  $\hat{\tau} = \bar{d}^2/(4D^s)$ , where  $\bar{d}$  is the mean diameter of the colloidal particles and we use for the MCT fits  $D^s = D_A^0$ . Again, one expects a correction of  $\hat{\tau}$  due to missing short-time effects in the theory; furthermore the systems of Ref. [103] are considerably polydisperse. Thus, the adjustment  $\hat{\tau}/\hat{\tau}_{\text{MCT}} \approx 3.7$  with  $D_\alpha^0 \propto 1/d_\alpha$  employed in the fits seems justifiable.

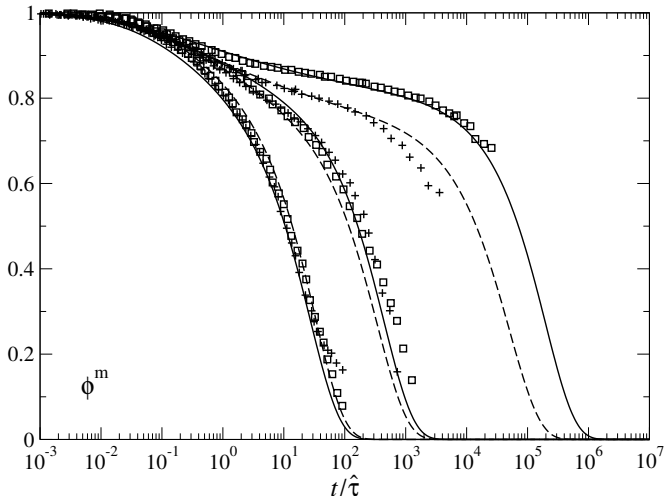


FIGURE 5.10. Correlation functions  $\phi^m(q, t)$  measured for hard-sphere like colloidal suspensions of a monomodal (plus symbols) and a bimodal size distributions (squares), at  $q$  corresponding to the first maximum in the structure factor (from Ref. [103]). Packing fractions are (from left to right)  $\varphi^{\text{exp}} = 0.535, 0.558,$  and  $0.567$  for the former, and  $\varphi^{\text{exp}} = 0.536, 0.556,$  and  $0.566$  for the latter. The dashed (solid) lines are MCT fits using a one-component (two-component) model with packing fractions  $\varphi^{\text{MCT}} = 0.485, 0.505,$  and  $0.5145$ . The two-component model assumes  $\delta = 0.8$  and  $\hat{x}_B = 0.12$  and a weighting with scattering amplitudes as given in Eqs. (4.6) and (4.8). Wave vectors are  $q = 6.6/d$  ( $q = 7.4/d_A$ ) for the one-component (two-component) fit.

One notices from Fig. 5.10 that the calculated correlators show the same qualitative trend as the data; the agreement is even semi-quantitative. Note that we did not intend to do a best-possible fit of the data, which would involve different packing fractions for the two systems. Instead we have chosen to show results for three selected values of  $\varphi$  taken equal in both systems in order to emphasize the mixing effect.

A system similar to the one just discussed, at least from the viewpoint of the theory, was studied by Bartsch and Eckert [138, 139]. Their aim

was to investigate the MCT predictions for a one-component colloidal system with a short-ranged effective attraction between the colloidal particles [A5, 72]. The effective attraction is caused by some amount of free polymer in the solvent, and in the limit of no free polymer, the colloidal particles, which are in this case cross-linked polymers, interact approximately with an  $r^{-35}$  potential [140]. We will treat this to be sufficiently close to a hard-sphere repulsion. To avoid crystallisation, a binary mixture was prepared, with size of the large particles  $d_A = 2.185$  nm, size ratio  $\delta = 0.81$ , and a particle number ratio  $N_B/N_A = 2.7$ , thus  $\hat{x}_B \approx 0.6$ . In Ref. [140], it was already anticipated that this mixture can be treated as an effective one-component system.

We have performed fits similar to the ones presented above to the data of Eckert and Bartsch. Again, the scattering amplitudes  $b_\alpha(q)$  are taken from Eq. (4.8) as a simple approximation. The wave vector of the experiment is given in Ref. [140] as “corresponding to the peak of  $S(q)$ ”; we have chosen  $q \approx 7.8/d_A$  to approximately match the first maximum of the total structure factor  $S(q) = \sum_{\alpha\beta} S_{\alpha\beta}$  in the fit. Fig. 5.11 shows the comparison of experimental data with the MCT results; the latter have been calculated using  $D_A^0 = 2.738$  m<sup>2</sup>/s. The values of  $\varphi$  used in the fits are shown in the inset. Here, the plot of  $\varphi^{\text{MCT}}$  vs.  $\varphi^{\text{exp}}$  is found to be close to a straight line,  $\varphi^{\text{MCT}} \approx a(\varphi^{\text{exp}} + b)$  with  $a \approx 0.42$  and  $b \approx 0.63$ , shown in the inset as a dashed line. This fit reasonably reproduces the decay of the correlator at the lowest three packing fractions shown. Deviations at short times,  $t < 0.01$  s, are much stronger than in the previously shown fits. Since the MCT dynamics in this time window is rather similar in all cases studied, this emphasizes a difference in the short-time relaxation between the crosslinked-polymer system studied in Ref. [139] and the PMMA colloids used by Henderson, van Meegen and coworkers [8, 103]. The origin of this difference is unclear and cannot be addressed within a theory treating both systems as ideal hard spheres. At long times, the data in Fig. 5.11 show a final relaxation also for  $\varphi^{\text{exp}} \geq 0.595$ , while the fitted MCT curves represent a glassy state relaxing to a finite  $f^{\text{m.c.}}(q)$ . This fit is in accordance with an asymptotic analysis carried out in Ref. [140], which gives a glass-transition value of  $\varphi^{\text{exp,c}} \approx 0.596$ . The data taken above this packing fraction are probably referring to nonequilibrium states in which the system is ‘ageing’, *i.e.*, the correlation functions depend both on the time difference  $t$  and the ‘waiting time’  $t_w$  that has passed since the system was prepared; as one

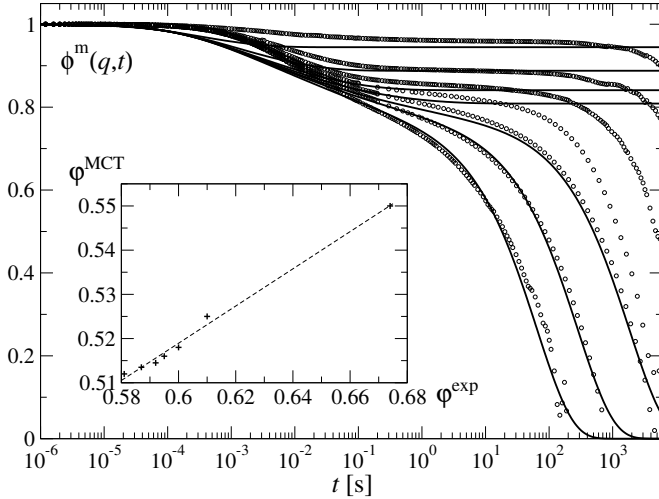


FIGURE 5.11. Correlation functions  $\phi^m(q, t)$  measured for a binary mixture of cross-linked polymer colloids characterized by  $\delta = 0.81$  and  $\hat{x}_B \approx 0.6$  (symbols, data from Ref. [140]). The wave vector corresponds to the first maximum of the measured structure factor  $S(q)$ ; packing fractions are  $\varphi^{\text{exp}} = 0.581, 0.587, 0.592, 0.595, 0.6, 0.61$  and  $0.674$ , from left to right. Solid lines are MCT results according to Eqs. (4.6) and (4.8) for  $\delta = 0.8$  and  $\hat{x}_B = 0.6$ , at  $qd_A = 7.8$  and packing fractions  $\varphi^{\text{MCT}} = 0.512, 0.5135, 0.5145, 0.516, 0.518, 0.525$ , and  $0.550$ , from left to right. The inset shows a plot of  $\varphi^{\text{exp}}$  vs.  $\varphi^{\text{MCT}}$  (plus symbols) together with a linear transformation law (dashed line),  $\varphi^{\text{MCT}} = a(\varphi^{\text{exp}} + b)$ , with  $a \approx 0.42$ ,  $b \approx 0.63$ .

lets the samples age, the final decay in the measured correlation functions shifts to still longer times, and the data more and more approach the theoretical curves<sup>3</sup>.

In data analysis of such and similar systems, one often silently assumes that “sufficiently monodisperse” systems can be analysed in terms of true one-component models. Let us demonstrate the validity of such assumption for the binary mixture with  $\delta = 0.8$  used in Ref. [140]. To

<sup>3</sup>T. Eckert, priv. comm.

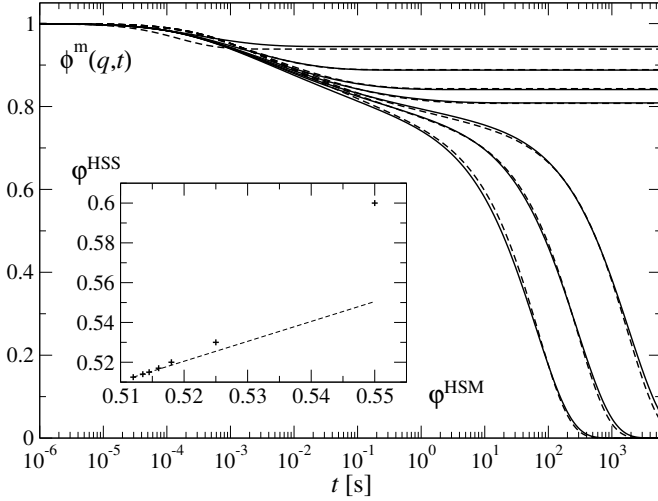


FIGURE 5.12. Solid lines:  $\phi^m(q, t)$  as fitted to the data of Ref. [140], *cf.* Fig. 5.11. Dashed lines are from a fit to the same data using a one-component hard-sphere model, with packing fractions  $\varphi = 0.5125, 0.514, 0.515, 0.517, 0.52, 0.53,$  and  $0.6$ , from left to right, and wave vector  $qd = 6.6$ . The inset shows the correspondence between packing fraction values  $\varphi^{\text{HSM}}$  and  $\varphi^{\text{HSS}}$  used for the binary mixture model and the one-component fit, respectively, as plus symbols. The dashed line in the inset represents a shift  $\varphi^{\text{HSS}} = \varphi^{\text{HSM}} + (\varphi^{\text{HSS},c} - \varphi^{\text{HSM},c})$ .

this end, we have performed a fit analogous to the one shown in Fig. 5.11 using a one-component hard-sphere model. A similar fit quality as with the binary model can be achieved, albeit with different packing fractions and using a different wave vector. In the present case, a change from  $qd_A = 7.8$  to  $qd = 6.6$  was sufficient in order to compensate for the change in plateau values on the liquid side. The difference in packing fractions can be anticipated from the change of the glass-transition packing fraction upon mixing, *cf.* Fig. 4.1. Instead of discussing the one-component fit to the data, let us show in Fig. 5.12 the comparison of the fitted one-component results (dashed lines) to the previously fit binary-mixture results (solid lines). One finds good agreement between

the two. On the liquid side, a slightly different shape in the ‘ $\alpha$ ’ relaxation regime as well as in the relaxation towards the plateau can be seen. It is due to the slight change in the exponent parameter  $\lambda$  upon mixing, as discussed in connection with Fig. 4.18, causing the mixture to show a more stretched decay. One could further improve on eliminating the small remaining differences in the plateau values on the glass side by fine-tuning the  $\varphi$  values, but we have refrained from doing so. Note that the  $\varphi = 0.6$  curve for the HSS case is at the limit of the PY approximation for the one-component structure factor; for  $\varphi \gtrsim 0.609$ , it leads unphysical input since  $g(r)$  develops negative values.

The inset of Fig. 5.12 shows the relation between  $\varphi$  values for the HSM and the one-component calculation. Below the glass transition, they agree up to a shift,  $\varphi^{\text{HSS}} - \varphi^{\text{HSM}} = \Delta\varphi \approx \varphi^{\text{HSS},c} - \varphi^{\text{HSM},c}$ , where  $\varphi^{\text{HSM},c} \approx 0.5154$  is the glass-transition point of the  $\delta = 0.8$ ,  $\hat{x}_B = 0.6$  mixture. This correspondence also holds close to but above the transition, since the relevant asymptotic parameters describing the plateau values are nearly identical. In particular one gets  $h \approx 0.46$  for the one-component system at the wave vector chosen, and  $h^m \approx 0.42$  for the HSM correlation functions shown in Figs. 5.11 and 5.12. Deeper in the glass, the leading and next-to-leading order asymptotic description of  $f(q)$  is no longer valid (*cf.* Fig. 3 of Ref. [5]), and we find the simple shift between  $\varphi^{\text{HSS}}$  and  $\varphi^{\text{HSM}}$  to work no longer. While the mere fit quality of the experimental data allows for no clear distinction between the two models, the values for  $\varphi^{\text{HSM}}$  shown in the inset of Fig. 5.12 make the binary-mixture fit appear more reasonable.

## APPENDIX A

# Numerics

Let us summarize the technical procedures behind the numerical solutions shown in this work. They are straightforward generalisations to matrices of the ones used before [56, 141].

### 1. Discretisation of the Equations of Motion

Since the MCT approximation for the memory kernel, Eq. (2.18b), works in the time-domain and is not easily Laplace-transformed, the algorithms on which the results of this work are based implement Eq. (2.21) (or alternatively Eq. (2.18)) also in the time-domain,

$$(A.1) \quad (1/\tilde{D}_\alpha^0)\dot{\Phi}_{q,\gamma\beta}(t) + q^2 S_{q,\alpha\gamma}^{-1} \Phi_{q,\gamma\beta}(t) + \int_0^t M_{q,\alpha\gamma}(t-t')\dot{\Phi}_{q,\gamma\beta}(t) = 0,$$

where a sum over  $\gamma$  is implicit and we have introduced the quantities  $M_{q,\alpha\beta}(t) \triangleq q^2 \sqrt{x_\alpha x_\beta} M_{\alpha\beta}(q, t)$ ,  $\Phi_{q,\alpha\beta}(t) \triangleq \Phi(q, t) / \sqrt{x_\alpha x_\beta}$ ,  $S_{q,\alpha\beta} = S_{\alpha\beta}(q) / \sqrt{x_\alpha x_\beta}$  and  $\tilde{D}_\alpha^0 = D_\alpha^0 / x_\alpha$ , where  $\triangleq$  stands for ‘discretised approximation to’. The result is a set of  $L = m(m+1)/2 \cdot M$  coupled integro-differential equations for an  $m$ -component mixture with wave vectors discretised to  $M$  values. We were able to solve the problem for up to  $L = 900$  on (at the time of writing) modern standard PC hardware.

Equation (A.1) is written for discrete times  $t_i = i \cdot h_d$ ,  $i \in \mathbb{N}$ , approximating integrals as Riemann sums. We will use  $f(t_i) = f_i$  as a shorthand in the following. For the time-domain convolution, an approximation is used that is particularly adapted to the problem under consideration: We split the integral at some intermediate time  $\bar{t} \in h_d \cdot \mathbb{N}$ ,  $0 < \bar{t} = \bar{i} h_d < t$ , and use partial integration in the first term to get

(dropping matrix indices)

$$(A.2) \quad \int_0^{t_i} M_q(t_i - t') \dot{\Phi}_q(t') dt' = \sum_{k=1}^{\bar{i}} \int_{t_{k-1}}^{t_k} [\partial_t M_q(t - t')] \Phi_q(t') dt' \\ + \sum_{k=1}^{i-\bar{i}} \int_{t_{k-1}}^{t_k} M_q(t') [\partial_t \Phi_q(t - t')] dt' + M_q(t - \bar{t}) \Phi_q(\bar{t}) - M_q(t) \Phi_q(0).$$

We now use the mean value theorem of calculus to pull the derivatives out of the integral. Approximation the unknown midpoints by one of their boundaries, we get with an error of  $\mathcal{O}(h_d^2 \partial_t^2 \Phi)$

$$(A.3) \quad \int_0^{t_i} M_q(t_i - t') \dot{\Phi}_q(t') dt' \triangleq \sum_{k=1}^{\bar{i}} (M_{q,i-k+1} - M_{q,i-k}) d\Phi_k \\ + \sum_{k=1}^{i-\bar{i}} dM_k (\Phi_{q,i-k+1} - \Phi_{q,i-k}) + M_{q,i-\bar{i}} \Phi_{q,\bar{i}} - M_{q,i} \Phi_{q,0},$$

where we have introduced the so-called moments

$$(A.4) \quad dF_k = \frac{1}{h_d} \int_{t_{k-1}}^{t_k} F(t') dt'.$$

The derivative in Eq. (A.1) is approximated by a differentiation of an interpolation polynomial [142],

$$(A.5) \quad \dot{\Phi}(t_i) \triangleq \frac{1}{h_d} \left( \frac{1}{2} \Phi_{i-2} - 2\Phi_{i-1} + \frac{3}{2} \Phi_i \right) + \mathcal{O}(h_d^2 \partial_t^3 \Phi).$$

With this, the discrete version of Eq. (A.1) can be written down. For given  $t = t_i$  one can, knowing the values of  $\Phi_j$ ,  $M_j$ ,  $d\Phi_j$ , and  $dM_j$  at all  $j < i$ , calculate the new value  $\Phi_i$ . Since  $M_i \equiv M_i[\Phi_i]$ , the problem to be solved is that of a set of  $L$  coupled implicit equations for  $\Phi_i$ .

Rearranging terms such, one has

(A.6a)

$$A_{q,\alpha\beta} = q^2 S_{\alpha\beta}^{-1}(q) + dM_{q,\alpha\beta,1} + 3/(2h_d D_\alpha^0) \delta_{\alpha\beta},$$

(A.6b)

$$B_{q,\alpha\beta} = \Phi_{q,\alpha\beta,0} - d\Phi_{q,\alpha\beta,1},$$

(A.6c)

$$\begin{aligned} C_{q,\alpha\beta,i} &= \sum_{k=2}^{\bar{i}} (M_{q,\alpha\gamma,i-k+1} - M_{q,\alpha\gamma,i-k}) d\Phi_{q,\gamma\beta,k} \\ &+ \sum_{k=2}^{i-\bar{i}} (\Phi_{q,\gamma\beta,i-k+1} - \Phi_{q,\gamma\beta,i-k}) dM_{q,\alpha\gamma,k} + M_{q,\alpha\gamma,i-\bar{i}} \Phi_{q,\gamma\beta,\bar{i}} \\ &- (M_{q,\alpha\gamma,i-1} d\Phi_{q,\gamma\beta,1} + \Phi_{q,\gamma\beta,i-1} dM_{q,\alpha\gamma,1}) \\ &+ (1/\tilde{D}_\alpha^0) (\frac{1}{2} \Phi_{q,\alpha\beta,i-2} - 2\Phi_{q,\alpha\beta,i-1})/h_d, \end{aligned}$$

(A.6d)

$$\Phi_{q,\alpha\beta,i} = A_{q,\alpha\gamma}^{-1} M_{q,\gamma\delta,i} B_{q,\delta\beta} - C_{q,\alpha\beta,i}.$$

which is solved by iteration.

Once the  $\Phi(q, t)$  have been determined within numerical accuracy, they can be used to calculate *e.g.* the tagged-particle correlator  $\Phi_s(q, t)$ , or the moduli and viscosities. Equation (2.23) has the same structure as Eq. (2.21), and can thus be solved with the algorithm just sketched.

The same holds for equations of structural relaxation, Eq. (3.50), as well as for the  $\beta$  scaling equation determining  $g(t)$ , Eq. (3.44), and the correction-to-scaling equation determining  $h(t)$ , Eq. (3.47). The latter equation has, alongside the wanted solution  $h(t) \sim t^{-2a}$  for  $t \rightarrow 0$ , also a homogeneous solution,  $\hat{h}(t) \sim t^{-a}$  for  $t \rightarrow 0$ . The latter has to be subtracted from the numerical solution, as was described in Ref. [75]. Common in all these equations is that their solution has an integrable divergence as  $t \rightarrow 0$ . The careful treatment of this divergence can be boiled down to a special rule calculating the ‘moments’ for  $k = 1$  and setting the corresponding initial value to unity in the above algorithm. This can easily be seen by splitting off from the integrals the ones  $\int_0^h \cdot dt$  and  $\int_{t-h}^t \cdot dt$  and applying the moment approximation to the remainder.

## 2. Calculation of Memory Kernels

The three-dimensional integrals over  $\vec{k}$  appearing in Eqs. (2.18c), (2.22a), and (2.23) are transformed to so-called bipolar coordinates: Due to isotropy, a rotation around the  $\vec{q}$  axis can be integrated out, and we can transform  $d^3k \rightarrow 2\pi \varrho d\varrho dz$  where  $\varrho$  and  $z$  are the projections of  $\vec{k}$  onto and orthogonal to  $\vec{q}$ , respectively. From these variables, we transform further to  $k = |\vec{k}|$  and  $p = |\vec{q} - \vec{k}|$ . Noting  $\varrho|\partial(\varrho z)/\partial(kp)| = (kp/q)$ , we get

$$(A.7) \quad \int \frac{d^3k}{(2\pi)^3} \cdot \equiv \frac{1}{q} \int \frac{k dk p dp}{2\pi}.$$

with both integrals on the right-hand side over  $[0, \infty[$  with the appropriate restriction  $p \in [|q - k|, q + k]$ . These integrals are discretised to an equidistant grid of  $M$  points with grid spacing  $\Delta q$  and evaluated as Riemann sums. Furthermore, we use

$$(A.8a) \quad (q\vec{k}) = (q^2 + k^2 - p^2)/2 \quad \text{and}$$

$$(A.8b) \quad (q\vec{p}) = (q^2 + p^2 - k^2)/2$$

to arrive at the discretised expression of the memory kernel,

$$(A.9a) \quad M_{q,\alpha\beta}(t) = \frac{(\Delta q)^2}{32\pi^2 q^3} \sum_{\substack{kp \\ \alpha'\beta'\alpha''\beta''}} kp V_{qkp}^{\alpha\alpha'\alpha''} V_{qkp}^{\beta\beta'\beta''} \Phi_{k,\alpha'\beta'}(t) \Phi_{p,\alpha''\beta''}(t).$$

Here, the coupling coefficients are given as

$$(A.9b) \quad V_{qkp}^{\alpha\beta\gamma} = [\delta_{\alpha\gamma} \hat{c}_{\alpha\beta}(k) \cdot (q^2 + k^2 - p^2) + \delta_{\alpha\beta} \hat{c}_{\alpha\gamma}(p) \cdot (q^2 + p^2 - k^2)].$$

For the  $q \rightarrow 0$  limits in Eqs. (2.24), (2.33), (2.34), and (2.35), the given analytic expressions can be discretised. These involve only single integrals over  $k$ ; thus the calculation is straightforward and we do not write down the result here.

## 3. Calculation of Time-Independent Quantities

The long-time limits of the correlators,  $\mathbf{F}(q) = \lim_{t \rightarrow \infty} \Phi(q, t)$ , are determined through Eq. (3.12), solved iteratively with the mapping of Eq. (3.13) that is guaranteed to converge to the correct solution, as Sec. 3.1 shows. The set of  $L$  coupled equations has been solved for

values of  $L$  up to 2000. Equation (3.23) can be solved iteratively for  $\mathbf{H}(q)$ , and a similar equation holds for  $\hat{\mathbf{H}}(q)$ . The correction amplitudes  $\mathbf{K}(q)$  and  $\bar{\mathbf{K}}(q)$  appearing in Sec. 3.2 are solutions of Eq. (3.23) with different inhomogeneities, given by Eqs. (3.24) and (3.34). They can also be solved iteratively, where after each iteration step,  $\mathbf{K}(q)$  and  $\bar{\mathbf{K}}(q)$  have to be orthogonalised according to  $\text{tr}(\hat{\mathbf{H}}(q)\mathbf{K}(q)) = 0$  and  $\text{tr}(\hat{\mathbf{H}}(q)\bar{\mathbf{K}}(q)) = 0$ .

Values for the glass-transition packing fractions  $\varphi^c$  shown in Fig. 4.1 have been determined to at least six leading digits with a bisection search for a zero in  $1 - E$ , where  $E$  is the eigenvalue of the mapping of Eq. (3.23) to noncritical points,  $\mathbf{C}[\mathbf{H}] = E\mathbf{H}$ . For the exponent parameter  $\lambda$ , typically a higher accuracy is needed; thus we have shown in Fig. 4.18 only the points where the numerically determined critical eigenvalue satisfies  $1 - E < 10^{-3}$ . For the values given in the text of Sec. 4,  $1 - E < 10^{-5}$  holds.



## APPENDIX B

# Perron-Frobenius Theorem

In this appendix, some results from a generalised Perron-Frobenius theorem for irreducible positive linear maps on  $C^*$  algebras are proven. We include this for completeness; for a more thorough and complete discussion, we refer to the mathematical literature [66]. The notation shall be adapted to the problem discussed in Sec. 3.1.

A  $C^*$  algebra is a Banach algebra with some involution satisfying  $\|a^*a\| = \|a\|^2$  for every element  $a$ ; as usual, a Banach algebra is a normed vector space where the metric induced by the norm is complete (*i.e.* where every Cauchy sequence is convergent) and where  $\|ab\| \leq \|a\|\|b\|$ . Indeed, the space of finite-dimensional matrices over  $\mathbb{C}$  is a standard example for a  $C^*$  algebra.

As in Sec. 3.1, let  $\mathcal{A}^M$  denote the  $C^*$  algebra of  $M$ -component vectors whose elements are  $m \times m$  matrices over the complex numbers  $\mathbb{C}$ .<sup>1</sup> Consider the positive linear map  $\psi$  that maps the cone of symmetric, real, positive definite elements onto itself, denoted  $\psi[a] \in \mathcal{A}_+^M$  for all  $a \in \mathcal{A}_+^M$ .

The mapping  $\psi$  shall be called ‘irreducible’ if for some positive finite  $n$ ,

$$(B.1) \quad T[y] := (1 + \psi)^n [y] \succ 0 \quad \text{for } y \succeq 0.$$

Indeed, several notions of ‘irreducibility’ exist for the general case of a  $C^*$  algebra [143, 144], but from a physicist’s point of view we can stick with the meaning “having no invariant subspaces.” If  $\psi$  is irreducible,

---

<sup>1</sup>As explained in Sec. 3.1, the matrix operators over  $\mathcal{A}$  are defined to work element-wise in  $q$ . With  $\|\cdot\|$  the maximum norm  $\|a\| = \max_q \|a_q\|$ , one directly proves  $\|ab\| \leq \max_q (\|a_q b_q\|) \leq \max_q \|a_q\| \max_k \|b_k\| = \|a\|\|b\|$  and  $\|a^*a\| = \max_q \|a_q^* a_q\| = \max_q \|a_q\|^2 = (\max_q \|a_q\|)^2 = \|a\|^2$  since the norm is always positive.

we also have that for  $y \succ 0$ ,  $\psi[y] \succ 0$  holds. Now define a mapping  $r : (\mathcal{A}_+^M, \mathbb{C}^m) \rightarrow \mathbb{R}$  by

$$(B.2) \quad r(a, v) = \min_{1 \leq q \leq M} \frac{(v|\psi_q[a]v)}{(v|a_qv)},$$

where  $q$  labels the elements of  $a \in \mathcal{A}^M$ ,  $a = (a_q)_{q=1, \dots, M}$ , and  $(\cdot|\cdot)$  is a scalar product over  $\mathbb{C}^m$ . Furthermore, set  $r(a) = \inf_{v \in \mathbb{C}^m} r(a, v) = \inf_{v \in \mathcal{S}^m} r(a, v)$ , where  $\mathcal{S}^m$  denotes the  $s$ -dimensional unit sphere, and the last equation holds since  $r(a, \lambda v)$  is independent of  $\lambda \in \mathbb{C}$ . However,  $r(a, v)$  is not necessarily continuous on  $(\mathcal{A}_+^M, \mathbb{C}^m)$ . Let us therefore define a set  $\mathcal{B} := \{b; b = T[a], a \in \mathcal{A}_+^M, \|a\| = 1\}$ . Then,  $b \succ 0$  for any  $b \in \mathcal{B} \subset \mathcal{A}_+^M$ , and  $r(b, v)$  is continuous on the closed and compact set  $(\mathcal{B}, \mathcal{S}^m)$  and thus attains its infimum with respect to  $v$ . It follows that on  $\mathcal{B}$ ,  $r(b)$  fulfills a maximum principle: since there exist some  $v_0 \in \mathcal{S}^m$  and  $q_0 \in [1, M]$  such that  $r(b) = r(b, v_0) = (v_0|\psi_{q_0}[b]v_0)/(v_0|b_{q_0}v_0)$ , we have that for any  $\varepsilon > 0$ ,  $(v_0|\{\psi_{q_0}[b] - (r(b) + \varepsilon)b_{q_0}\}v_0) \not\geq 0$ . In other words,  $r(b)$  is the maximum  $\mathbb{R}$ -number for which  $\psi[b] \succeq r(b)b$ . Furthermore, for  $a \in \mathcal{A}_+^M$  and  $b = T[a] \in \mathcal{B}$  we have  $T[\psi[a] - r(a)a] = \psi[b] - r(a)b \succ 0$ , and by the maximum principle we get  $r(b) \geq r(a)$ .

Let  $1 \in \mathcal{A}_+^M$  denote the collection of  $M$  unit matrices, *i.e.* the unit element of  $\mathcal{A}^M$ . Since  $r(1) > 0$ , the relation

$$(B.3) \quad r = \sup_{a \in \mathcal{A}_+^M} r(a)$$

defines a number  $r > 0$ . Due to the maximum principle, the supremum can be restricted to elements  $b = T[a] \in \mathcal{B}$ . But there,  $r(b)$  attains its supremum  $r$  for some extremal vector  $z \succ 0$ .

Indeed,  $r$  is an eigenvalue of  $\psi$  and equal to its spectral radius: Assume on the contrary,  $\psi[\hat{z}] - r\hat{z} \succeq 0$  but not the null element. Then  $\psi[\hat{z}] - r\hat{z} \succ 0$  for  $\hat{z} = T[\hat{z}]$  and the maximum principle implies  $r(\hat{z}) > r$  in contradiction to the definition of  $r$ . Thus,  $r$  is an eigenvalue of  $\psi$ . Suppose now there are two eigenvectors  $z, z' \in \mathcal{A}_+^M$  corresponding to  $r$  which are not scalar multiples of each other. We then can find some  $\lambda \in \mathbb{R}$  such that  $\lambda z - z' \succeq 0$  but not strictly positive to get  $T[\lambda z - z'] = (1 + r)^n(\lambda z - z') \succ 0$  in contradiction to the construction of  $\lambda$ . Thus, the eigenvalue  $r$  is non-degenerate on  $\mathcal{A}_+^M$ . Now for any  $a \in \mathcal{A}_+^M$ , define the mapping  $\sigma[a] = (1/r)z^{-1/2}\psi[z^{1/2}az^{1/2}]z^{-1/2}$ . Since  $\sigma[1] = 1$ ,  $\|\sigma\| = 1$ . Suppose  $\psi[u] = \alpha u$  with some (possibly complex)

eigenvalue  $\alpha \in \mathbb{C}$  and write  $v = z^{-1/2}uz^{-1/2}$ , which gives that  $v$  is an eigenvector of  $\sigma$ ,  $\sigma[v] = (\alpha/r)v$ . But for any eigenvalue  $\lambda$  of  $\sigma$ , we have  $|\lambda| \leq \|\sigma\|$ , and thus we get  $|\alpha| \leq r$ . We conclude that  $r$  is the spectral radius of  $\psi$ .



## APPENDIX C

# Percus-Yevick Structure Factor for Hard Spheres

The Ornstein-Zernike equation together with the Percus-Yevick closure can be solved analytically for an  $N$ -component mixture of hard spheres. This was first shown by Lebowitz [77], and later adopted by Baxter [78] to his so-called factorisation technique. In this appendix, the result shall be quoted, reformulated to give an explicit expression for the direct correlation function in wave-vector space,  $c_{\alpha\beta}(q)$ . For details, the reader is referred to the original literature.

Let  $d_\alpha$  denote the diameters of the hard spheres of species  $\alpha$ , and  $d_{\alpha\beta} = (d_\alpha + d_\beta)/2$ ,  $\bar{d}_{\alpha\beta} = (d_\alpha - d_\beta)/2$ . In brief, the solution can be written as  $\mathbf{S}(q) = \mathbf{X}^{1/2}[\mathbf{1} - n\tilde{\mathbf{c}}(q)]^{-1}\mathbf{X}^{1/2}$ , with  $X_\alpha = \delta_{\alpha\beta}x_\alpha$  the diagonal matrix of number concentrations, and  $\tilde{\mathbf{c}}(q) = \mathbf{X}^{1/2}\mathbf{c}(q)\mathbf{X}^{1/2}$ . The Baxter factorisation technique proceeds by writing

$$(C.1) \quad \mathbf{1} - n\tilde{\mathbf{c}}(q) = \mathbf{Q}^T(-q)\mathbf{Q}(q)$$

with the so-called Baxter factor function

$$(C.2) \quad Q_{\alpha\beta}(q) = \delta_{\alpha\beta} - \int_{\bar{d}_{\alpha\beta}}^{d_{\alpha\beta}} e^{iqr} Q_{\alpha\beta}(r) dr.$$

From the Ornstein-Zernike equations with the Percus-Yevick closure, a simple polynomial for  $\mathbf{Q}(r)$  results:

$$(C.3) \quad Q_{\alpha\beta}(r) = \frac{1}{2}a_\alpha(r^2 - d_{\alpha\beta}^2) + b_\alpha(r - d_{\alpha\beta}),$$

whose coefficients can be determined to

$$(C.4) \quad a_\alpha = \frac{1 - \xi_3 + 3d_\alpha\xi_2}{(1 - \xi_3)^2}, \quad b_\alpha = -\frac{3}{2} \frac{d_\alpha^2\xi_2}{(1 - \xi_3)^2},$$

with the abbreviation  $\xi_x = \frac{\pi}{6} \sum_\gamma n_\gamma d_\gamma^x$ .

Back-inserting the result and some lengthy but elementary algebra yields an explicit expression for the Fourier-transformed direct correlation function: Setting  $S_\alpha = \sin(qd_\alpha/2)$ ,  $C_\alpha = \cos(qd_\alpha/2)$ , we obtain

$$(C.5) \quad c_{\alpha\beta}(q) = -4\pi \left[ A_{\alpha\beta} \frac{S_\alpha S_\beta - C_\alpha C_\beta}{q^2} + B_{\alpha\beta} \frac{C_\alpha S_\beta + C_\beta S_\alpha}{q^3} + D_{\alpha\beta} \frac{S_\alpha S_\beta}{q^4} + \frac{4\pi}{q^4} \tilde{a}_2 \left( \frac{C_\alpha C_\beta d_\alpha d_\beta}{4} + \frac{S_\alpha S_\beta}{q^2} - \frac{C_\alpha S_\beta d_\alpha + C_\beta S_\alpha d_\beta}{2q} \right) \right],$$

with the coefficients

$$(C.6) \quad A_{\alpha\beta} = \frac{d_{\alpha\beta}(1 - \xi_3) + \frac{3}{2}d_\alpha d_\beta \xi_2}{(1 - \xi_3)^2},$$

$$(C.7) \quad B_{\alpha\beta} = \frac{1}{1 - \xi_3} - \hat{\beta}_0 d_\alpha d_\beta,$$

$$(C.8) \quad D_{\alpha\beta} = \frac{6\xi_2 + 12d_{\alpha\beta}(\xi_1 + 3\xi_2^2/(1 - \xi_3))}{(1 - \xi_3)^2},$$

$$(C.9) \quad \tilde{a}_2 = \sum_{\gamma} n_\gamma a_\gamma^2,$$

$$(C.10) \quad \hat{\beta}_0 = \frac{9\xi_2^2 + 3\xi_1(1 - \xi_3)}{(1 - \xi_3)^3}.$$

As  $q \rightarrow 0$ , all  $c_{\alpha\beta}(q)$  approach a finite negative value,

$$(C.11) \quad c_{\alpha\beta}(q) = -\frac{\pi}{6} \left[ \frac{\pi}{6} \tilde{a}_2 (d_\alpha d_\beta)^3 + 2(d_\alpha + d_\beta)^2 A_{\alpha\beta} + \frac{1}{2} (d_\alpha d_\beta)^2 D_{\alpha\beta} \right] + \mathcal{O}(q^2).$$

For the numerical calculations, a Taylor expansion up to  $\mathcal{O}(q^4)$  has been used to evaluate  $c_{\alpha\beta}(q)$  at small  $q$ . Eq. (C.11) also serves as the starting point from which the compressibility can be calculated according to Eq. (2.30). One gets

$$(C.12) \quad \frac{1}{\kappa_T(nk_B T)} = \frac{\pi \rho}{6} \left[ \frac{\xi_0}{(1 - \xi_3)^2} + 6 \frac{\xi_1 \xi_2}{(1 - \xi_3)^3} + 9 \frac{\xi_2^3}{(1 - \xi_3)^4} \right]^{-1}.$$

It is well known that by solving the OZ equations only approximately, one introduces a so-called thermodynamic inconsistency, *i.e.*, the equation of state derived along the compressibility route presented here is not consistent with the one derived from the virial expansion [44]. An

*ad hoc* interpolation has been quite successful in the one-component hard-sphere system [145], and been generalised to mixtures by Boublík [96] and Mansoori, Carnahan, Starling and Leland [97], thus called the BMCSL equation of state,

$$(C.13) \quad \frac{1}{\kappa_T(nk_B T)} = \frac{\pi \varrho}{6} \left[ \frac{\xi_0}{(1 - \xi_3)^2} + 6 \frac{\xi_1 \xi_2}{(1 - \xi_3)^3} + \frac{\xi_2^3}{(1 - \xi_3)^4} (9 - 4\varphi + \varphi^2) \right]^{-1}.$$

The accuracy of this expression has been tested against computer simulations [80].

The Baxter factorisation technique also yields a tractable expression for the pair correlation functions  $g_{\alpha\beta}(r)$ . Setting  $f_{\alpha\beta}(r) = r(g_{\alpha\beta}(r) - 1)$ , the Ornstein-Zernike equation transforms to

$$(C.14) \quad f_{\alpha\beta}(r) = -Q'_{\alpha\beta}(r) + \left[ 2\pi \sum_{\gamma} \int_{\bar{d}_{\alpha\gamma}}^{\min(r, d_{\alpha\gamma})} Q_{\alpha\gamma}(t) f_{\gamma\beta}(r - t) dt \right] \Theta(r - \bar{d}_{\alpha\gamma}) - \left[ 2\pi \sum_{\gamma} \int_{\max(r, \bar{d}_{\alpha\gamma})}^{d_{\alpha\gamma}} Q_{\alpha\gamma}(t) f_{\gamma\beta}(t - r) dt \right] \Theta(d_{\alpha\gamma} - r).$$

This integral equation can be solved iteratively: knowledge of  $f_{\alpha\beta}(r)$  in the interval  $[0, R]$  is sufficient to calculate  $f_{\alpha\beta}(r)$  for  $r \in [R, R + \Delta r]$ , and thus one proceeds along the  $r$  axis. For hard-sphere mixtures, one knows  $f_{\alpha\beta}(r) = -r$  exactly for  $r < d_{\alpha\beta}$ .



## Conclusion

In this work, the dynamics of glass-forming binary hard-sphere mixtures has been investigated using the mode-coupling theory of the glass transition (MCT). The aim was to find mixing effects that are general for certain classes of glass-forming mixtures, and to demonstrate that the results are in qualitative and, in some cases, even quantitative agreement with experiments.

In addition, we have achieved to generalise a number of exact mathematical results that hold for the MCT equations of motion and their solutions. These had been known for one-component systems, and in Sec. 3, their generalisation to mixtures and molecular systems in the so-called site-site description is presented. A major result is that, for colloidal short-time dynamics, the solutions for the density correlation functions exist and are uniquely defined, smooth functions of the external parameters for all finite times (Sec. 3.1). Their long-time limits, the so-called glass form factors, exhibit bifurcations that are identified as glass transitions. While bifurcations in general resist classification, it has been possible to prove that within MCT, only certain types of bifurcations can occur. This in turn justifies the use of asymptotic expansions of the correlation functions that are well-established for one-component systems. We have presented a generalisation of the known leading and next-to-leading order results to mixtures in Sec. 3.2.

The application of MCT to binary hard-sphere systems could identify four general mixing effects for states near ideal liquid-glass transitions. This was done in Sec. 4, where such binary mixtures have been studied for a number of size ratios and various compositions.

First, mixing suppresses intermediate-range ordering effects which leads to an increase of the compressibility and to a decrease of the moduli for

compression and shear of the glass near the transition point, shown in Fig. 4.9 (pg. 56). Thus, the arrested structure shows a softening of the elastic restoring forces upon mixing.

Second, an apparently opposite phenomenon is seen through the increase of the Debye-Waller factors, *i.e.* a stiffening of the glass with respect to spontaneous density fluctuations, see Figs. 4.5 (pg. 49) and 4.7 (pg. 52). Closely related to this is the third general mixing effect, *viz.*: a stiffening of the particles' cages, described by the decrease of the critical amplitude upon mixing, as can be seen in Fig. 4.19 (pg. 75). This leads to a slowing down of the short-time part of the glassy dynamics, *i.e.* the part dealing with the relaxation towards the plateau values. The asymptotic formulae for MCT describe this slowing down (Fig. 4.21 on pg. 77). Additionally, the localisation of tagged particles in the mixture becomes better upon mixing: Fig. 4.10 on pg. 59.

The fourth general effect upon mixing concerns the time-scale for the long-time relaxation, *i.e.* for the ' $\alpha$ ' process of the liquid. Here, two scenarios have been found, one for small size disparity between the species of the binary mixture, and one for a large size disparity, see Fig. 4.1 on pg. 42 and Fig. 4.15 on pg. 67. For small size disparity, mixing stabilises the glass state, and the ' $\alpha$ ' time scale at fixed packing fraction becomes slower. Once the size ratio is smaller than about 0.65, an entropic plasticisation effect is found: due to mixing, the glass state is destabilised, and the ' $\alpha$ ' relaxation times decrease.

These general trends explain qualitatively what has been found in recent experiments on binary colloidal hard-sphere mixtures [8], which fall into our category of large size disparity. The theory suggests to carry out similar experiments in the region of small size disparity to provide further tests of MCT.

Quantitative comparisons of the theoretical predictions with available experimental data on colloidal mixtures have been presented in Sec. 5. There, the most challenging data comes from the experiment of Ref. [8], since with this experimental setup it was possible to determine all three partial time-dependent density correlation functions of three different binary mixtures. Encouragingly, a quantitative fit to these data over many orders of magnitude in time and for several packing fractions has been possible, *cf.* Fig. 5.1 on pg. 85. Strong disagreement has, however, been found for the correlations between the minority species of smaller

spheres (*cf.* lower panel of Fig. 5.1). A further investigation of this discrepancies using rather fundamental arguments based on Sec. 3.1 showed it is quite possible that inevitable experimental uncertainties give rise to the observed disagreement (see Fig. 5.6 on pg. 91).

Other data for the small size disparity case is less detailed, but nevertheless it was possible in Sec. 5.2 to further corroborate the general findings of Sec. 4, see *e.g.* Fig. 5.10 on pg. 98. We have also presented some preliminary results concerning the change of structural quantities at the glass transition upon polydispersity (Fig. 5.9 on pg. 95). The results seem to indicate that some general polydispersity effects might exist and suggest further research in this direction.

It can be expected that the results presented here are not only applicable to colloidal suspensions, but also to glass-forming binary alloys. The formation of metallic glasses can to some extent be understood by treating the constituent atoms as hard spheres, which will then all be of similar size [146]. Our results for the long-time quantities are, up to a common time scale, not affected by the difference between colloidal and Newtonian dynamics, as was explained in Sec. 3.3. Indeed, recent computer simulation studies of  $\text{Co}_{100-x}\text{Zr}_x$  models shows a variation of the critical temperature  $T_c$  for the glass transition that is in qualitative agreement with our results, if one models the binary alloy by a hard sphere mixture with size ratio  $\delta \approx 0.78$ , calculated from the atomic radii [147]. A similar reasoning holds for computer-simulated Ni-Zr melts [22].



## List of Figures

4.1	Liquid-glass transition diagram of binary hard sphere mixtures.	42
4.2	Relative increase/decrease of the critical packing fractions.	44
4.3	Total structure factor for binary hard sphere mixtures.	45
4.4	Partial pair correlation functions for binary hard-sphere mixtures.	46
4.5	Critical glass form factors for size ratio $\delta = 0.8$ .	49
4.6	Matrix-normalised critical glass form factors for $\delta = 0.8$	51
4.7	Critical glass form factors for size ratio $\delta = 0.6$ .	52
4.8	Weighed critical form factor for a binary hard sphere mixture.	55
4.9	Elastic moduli evaluated for hard-sphere mixtures.	56
4.10	Critical localisation lengths of tagged particles.	59
4.11	Example demonstrating the glassy dynamics in a binary mixture.	61
4.12	Partial density correlation functions for $\delta = 0.8$ .	63
4.13	Partial density correlation functions for $\delta = 0.6$ .	64
4.14	Scattering-amplitude weighted density correlation functions.	66
4.15	‘ $\alpha$ ’ time scales of binary hard sphere mixtures.	67
4.16	Shear viscosities of binary hard-sphere mixtures.	69
4.17	Structural relaxation dynamics for binary hard-sphere mixtures.	73

4.18	Exponent parameters $\lambda$ as functions of mixing.	74
4.19	Normalised critical amplitudes for $\delta = 0.6$ .	75
4.20	Distance parameters $\sigma$ for size ratio $\delta = 0.6$ .	76
4.21	Asymptotic description of correlation functions for $\delta = 0.6$ .	77
4.22	Asymptotic description of correlation functions for $\delta = 0.6$ (ii).	78
4.23	Correction amplitudes $k(q)$ for size ratio $\delta = 0.6$ .	79
5.1	Fit to partial density correlators for $\delta = 0.6$ and $\hat{x}_B = 0.2$ .	85
5.2	Fit to partial density correlators for $\delta = 0.6$ and $\hat{x}_B = 0.1$ .	86
5.3	Fit to partial density correlators for $\delta = 0.6$ and $\hat{x}_B = 0.05$ .	87
5.4	Fit to experimental data with different scattering amplitudes.	89
5.5	Single-particle form factors for hard-sphere like colloids.	90
5.6	Time-dependent eigenvalues of experimental density correlators.	91
5.7	Mapping of experimental and fitted packing fraction values.	92
5.8	Fit to partial density correlation functions at different wave vectors.	93
5.9	Change of critical form factors in a polydispersity model.	95
5.10	Correlation functions for mono- and bimodal colloidal suspensions.	98
5.11	Data and fit for binary cross-linked polymer colloidal mixtures.	100
5.12	Comparison of one- and two-component fit for size ratio $\delta = 0.8$ .	101

## Publications of the Author

- [A1] M. Fuchs and Th. Voigtmann, *Philos. Mag. B* **79**, 1799 (1999).
- [A2] W. Götze and Th. Voigtmann, *Phys. Rev. E* **61**, 4133 (2000).
- [A3] W. Götze, A. P. Singh, and Th. Voigtmann, *Phys. Rev. E* **61**, 6934 (2000).
- [A4] J. Bergenholtz, M. Fuchs, and Th. Voigtmann, *J. Phys.: Condens. Matter* **12**, 6575 (2000).
- [A5] K. Dawson, G. Foffi, M. Fuchs, W. Götze, F. Sciortino, M. Sperl, P. Tartaglia, Th. Voigtmann, and E. Zaccarelli, *Phys. Rev. E* **63**, 011401 (2001).
- [A6] W. Götze and Th. Voigtmann, *Phys. Bl.* **57**, 41 (2001).
- [A7] Th. Voigtmann, *J. Non-Cryst. Solids* **307–310**, 188 (2002).
- [A8] T. Franosch and Th. Voigtmann, *J. Stat. Phys.* **109**, 237 (2002).



## Bibliography

- [1] U. Bengtzelius, W. Götze, and A. Sjölander, *J. Phys. C* **17**, 5915 (1984).
- [2] E. Leutheusser, *Phys. Rev. A* **29**, 2765 (1984).
- [3] W. Götze, in *Amorphous and Liquid Materials*, edited by E. Lüscher, G. Fritsch, and G. Jacucci (Nijhoff Publishers, Dordrecht, 1987), NATO ASI Series, pp. 34–81.
- [4] W. Götze, in *Liquids, Freezing and Glass Transition*, edited by J. P. Hansen, D. Levesque, and J. Zinn-Justin (North Holland, Amsterdam, 1991), vol. Session LI (1989) of *Les Houches Summer Schools of Theoretical Physics*, pp. 287–503.
- [5] T. Franosch, M. Fuchs, W. Götze, M. R. Mayr, and A. P. Singh, *Phys. Rev. E* **55**, 7153 (1997).
- [6] M. Fuchs, W. Götze, and M. R. Mayr, *Phys. Rev. E* **58**, 3384 (1998).
- [7] S.-H. Chong, W. Götze, and A. P. Singh, *Phys. Rev. E* **63**, 011206 (2001).
- [8] S. R. Williams and W. van Meegen, *Phys. Rev. E* **64**, 041502 (2001).
- [9] D. Frenkel, in *Soft and Fragile Matter*, edited by M. E. Cates and M. R. Evans (IOP Publishing, 2000), vol. 53 of *Scottish Universities Summer School in Physics*, pp. 113–144.
- [10] R. G. Larson, *The structure and rheology of complex fluids* (Oxford University Press, New York, 1999).
- [11] P. N. Pusey and W. van Meegen, *Nature* **320**, 340 (1986).
- [12] E. Liniger and R. Raj, *J. Am. Ceram. Soc.* **70**, 843 (1987).
- [13] E. Dickinson, S. J. Milne, and M. Patel, *Powder Technol.* **59**, 11 (1989).
- [14] S. R. Williams, I. K. Snook, and W. van Meegen, *Phys. Rev. E* **64**, 021506 (2001).

- [15] B. Bernu, J.-P. Hansen, Y. Hiwatari, and G. Pastore, *Phys. Rev. A* **36**, 4891 (1987).
- [16] J. N. Roux, J.-L. Barrat, and J.-P. Hansen, *J. Phys.: Condens. Matter* **1**, 7171 (1989).
- [17] W. Kob and H. C. Andersen, *Phys. Rev. Lett.* **73**, 1376 (1994).
- [18] W. Kob, *J. Phys.: Condens. Matter* **11**, R85 (1999).
- [19] J.-L. Barrat and A. Latz, *J. Phys.: Condens. Matter* **2**, 4289 (1990).
- [20] M. Nauroth and W. Kob, *Phys. Rev. E* **55**, 657 (1997).
- [21] W. Kob, M. Nauroth, and F. Sciortino, *J. Non-Cryst. Solids* **307–310**, 181 (2002).
- [22] A. B. Mutiara and H. Teichler, *Phys. Rev. E* **64**, 046133 (2001).
- [23] J. Horbach, W. Kob, and K. Binder, *Philos. Mag. B* **77**, 297 (1998).
- [24] J. Horbach, W. Kob, and K. Binder, *Eur. Phys. J. B* **19**, 531 (2001).
- [25] J. Horbach and W. Kob, *Philos. Mag. B* **79**, 1981 (1999).
- [26] J. Horbach, W. Kob, and K. Binder, *Chem. Geol.* **174**, 87 (2001).
- [27] J. Horbach, W. Kob, and K. Binder, *Phys. Rev. Lett.* **88**, 125502 (2002).
- [28] F. Sciortino and W. Kob, *Phys. Rev. Lett.* **86**, 648 (2001).
- [29] J. Bosse and J. S. Thakur, *Phys. Rev. Lett.* **59**, 998 (1987).
- [30] J. S. Thakur and J. Bosse, *Phys. Rev. A* **43**, 4378 (1991).
- [31] J. S. Thakur and J. Bosse, *Phys. Rev. A* **43**, 4388 (1991).
- [32] J. Bosse and Y. Kaneko, *Phys. Rev. Lett.* **74**, 4023 (1995).
- [33] Y. Kaneko and J. Bosse, *Molecular Simulation* **16**, 249 (1996).
- [34] J. Bosse and Y. Kaneko, *Prog. Theor. Phys. Suppl.* **126**, 13 (1997).
- [35] J. S. Thakur and J. Bosse, *J. Non-Cryst. Solids* **117/118**, 898 (1990).
- [36] J. Bosse and S. D. Wilke, *Phys. Rev. Lett.* **80**, 1260 (1998).
- [37] H. C. Chen, S. D. Wilke, and J. Bosse, *Phys. Rev. B* **60**, 12045 (1999).
- [38] U. Harbola and S. P. Das, *Phys. Rev. E* **65**, 036138 (2002).
- [39] U. Harbola and S. P. Das, *J. Chem. Phys.* **117**, 9844 (2002).
- [40] G. Srinivas, A. Mukherjee, and B. Bagchi, *J. Chem. Phys.* **114**, 6220 (2001).
- [41] A. Mukherjee, G. Srinivas, and B. Bagchi, *Phys. Rev. Lett.* **86**, 5926 (2001).

- [42] K. Kawasaki, Phys. Rev. **150**, 291 (1966).
- [43] J.-P. Boon and S. Yip, *Molecular Hydrodynamics* (McGraw-Hill, New York, 1980).
- [44] J.-P. Hansen and I. R. McDonald, *Theory of Simple Liquids* (Academic Press, London, 1986), 2nd ed.
- [45] U. Balucani and M. Zoppi, *Dynamics of the Liquid State* (Clarendon, Oxford, 1994).
- [46] A. Rahman, J. Chem. Phys. **45**, 2585 (1966).
- [47] J. L. Lebowitz and O. Penrose, Phys. Today **23**, 23 (1973).
- [48] N. W. Ashcroft and D. C. Langreth, Phys. Rev. **156**, 685 (1967).
- [49] C. Caccamo, Phys. Rep. **274**, 1 (1996).
- [50] H. W. Jackson and E. Feenberg, Rev. Mod. Phys. **34**, 686 (1962).
- [51] G. Nägele, Phys. Rep. **272**, 215 (1996).
- [52] P. N. Pusey, in *Liquids, Freezing and Glass Transition*, edited by J. P. Hansen, D. Levesque, and J. Zinn-Justin (North Holland, Amsterdam, 1991), vol. Session LI (1989) of *Les Houches Summer Schools of Theoretical Physics*, pp. 765–942.
- [53] W. Hess and R. Klein, Adv. Phys. **32**, 173 (1983).
- [54] G. Szamel and H. Löwen, Phys. Rev. A **44**, 8215 (1991).
- [55] M. Fuchs, Ph.D. thesis, TU München (1993).
- [56] M. Fuchs, W. Götze, I. Hofacker, and A. Latz, J. Phys.: Condens. Matter **3**, 5047 (1991).
- [57] L. D. Landau and E. M. Lifshitz, *Fluid Mechanics* (Butterworth-Heinemann, Woburn, MA, 1987), 2nd ed.
- [58] I. M. Mryglod, Cond. Matt. Phys. **10**, 115 (1997).
- [59] W. Götze and A. Latz, J. Phys.: Condens. Matter **1**, 4169 (1989).
- [60] A. Latz, Ph.D. thesis, TU München (1991).
- [61] G. Nägele and J. Bergenholtz, J. Chem. Phys. **108**, 9893 (1998).
- [62] G. Gripenberg, S. O. Londen, and O. Staffans, *Volterra Integral and Functional Equations*, vol. 34 of *Encyclopedia of Mathematics and Its Applications* (Cambridge University Press, Cambridge, 1990).
- [63] D. V. Widder, *The Laplace Transform* (Princeton University Press, Princeton, 1946).
- [64] W. Götze and L. Sjögren, J. Math. Analysis and Appl. **195**, 230 (1995).
- [65] W. Feller, *An Introduction to Probability Theory and Its Applications*, vol. II (Wiley & Sons, New York, 1971), 2nd ed.

- [66] D. E. Evans and R. Høegh-Krohn, *J. London Math. Soc.* (2) **17**, 345 (1978).
- [67] F. R. Gantmacher, *The Theory of Matrices*, vol. II (Chelsea Publishing, New York, 1974).
- [68] V. I. Arnol'd, *Russ. Math. Survey* **30**, 1 (1975).
- [69] S.-H. Chong and W. Götze, *Phys. Rev. E* **65**, 041503 (2002).
- [70] T. Gleim, W. Kob, and K. Binder, *Phys. Rev. Lett.* **81**, 4404 (1998).
- [71] T. Franosch, W. Götze, M. R. Mayr, and A. P. Singh, *J. Non-Cryst. Solids* **235–237**, 71 (1998).
- [72] W. Götze and M. Sperl, *Phys. Rev. E* **66**, 011405 (2002).
- [73] W. Götze, *J. Phys.: Condens. Matter* **2**, 8485 (1990).
- [74] W. Götze and L. Sjögren, *J. Phys.: Condens. Matter* **1**, 4183 (1989).
- [75] M. R. Mayr, Ph.D. thesis, TU München (1998).
- [76] R. K. McGeary, *J. Am. Ceram. Soc.* **44**, 513 (1961).
- [77] J. L. Lebowitz and J. S. Rowlinson, *J. Chem. Phys.* **41**, 133 (1964).
- [78] R. J. Baxter, *J. Chem. Phys.* **52**, 4559 (1970).
- [79] G. A. Martynov and G. N. Sarkisov, *Mol. Phys.* **49**, 1495 (1983).
- [80] P. Ballone, G. Pastore, G. Galli, and D. Gazzillo, *Mol. Phys.* **59**, 275 (1986).
- [81] A. Malijevský, M. Barošová, and W. R. Smith, *Mol. Phys.* **91**, 65 (1997).
- [82] S. Asakura and F. Oosawa, *J. Polym. Sci.* **33**, 183 (1958).
- [83] L. Fabbian, W. Götze, F. Sciortino, P. Tartaglia, and F. Thiery, *Phys. Rev. E* **59**, R1347 (1999), **60**, 2430(E).
- [84] J. Bergenholtz and M. Fuchs, *Phys. Rev. E* **59**, 5706 (1999).
- [85] A. P. Gast, C. K. Hall, and W. B. Russel, *J. Colloid Interface Sci.* **96**, 251 (1983).
- [86] S. I. Henderson and W. van Meegen, *Phys. Rev. Lett.* **80**, 877 (1998).
- [87] C. Lemaignan, *Acta Metall.* **28**, 1657 (1980).
- [88] J. D. Bernal, in *Liquids: Structure, Properties, Solid Interactions*, edited by T. J. Hughel (Elsevier, Amsterdam, 1965), pp. 25–50.
- [89] S. Torquato, T. M. Truskett, and P. G. Debenedetti, *Phys. Rev. Lett.* **84**, 2064 (2000).
- [90] G. D. Scott and G. J. Kovacs, *J. Phys. E* **6**, 1007 (1973).

- [91] S. Yerazunis, S. W. Cornell, and B. Wintner, *Nature* **207**, 835 (1965).
- [92] E. Zaccarelli, G. Foffi, K. A. Dawson, S. V. Buldyrev, F. Sciortino, and P. Tartaglia, *Phys. Rev. E* **66**, 041402 (2002).
- [93] A. Vrij, *J. Chem. Phys.* **71**, 3267 (1979).
- [94] L. Antl, J. W. Goodwin, R. D. Hill, R. H. Ottewill, S. M. Owens, S. Papworth, and J. A. Waters, *Colloids Surf.* **17**, 67 (1986).
- [95] A. Heymann, C. Sinn, and T. Palberg, *Phys. Rev. E* **62**, 813 (2000).
- [96] T. Boublík, *J. Chem. Phys.* **53**, 471 (1970).
- [97] G. A. Mansoori, N. F. Carnahan, K. E. Starling, and T. W. Leland, *J. Chem. Phys.* **54**, 1523 (1971).
- [98] M. Barošová, M. Malijevský, S. Labík, and W. R. Smith, *Mol. Phys.* **87**, 423 (1996).
- [99] J. M. Méndez-Alcaraz, M. Chávez-Páez, B. D'Aguzzo, and R. Klein, *Physica A* **220**, 173 (1995).
- [100] M. Fuchs, I. Hofacker, and A. Latz, *Phys. Rev. A* **45**, 898 (1992).
- [101] T. W. Leland, J. S. Rowlinson, and G. A. Sather, *Trans. Faraday Soc.* **64**, 1447 (1968).
- [102] G. A. Mansoori and J. Thomas W. Leland, *J. Chem. Soc. Faraday Trans. II* **68**, 320 (1972).
- [103] S. I. Henderson, T. C. Mortensen, G. M. Underwood, and W. van Meegen, *Physica A* **233**, 102 (1996).
- [104] P. H. Johnson and R. H. Kelsey, *Rubber World* **138**, 877 (1958).
- [105] J. S. Chong, E. B. Christiansen, and A. D. Baer, *J. Appl. Polym. Sci.* **15**, 2007 (1971).
- [106] B. E. Rodriguez, E. W. Kaler, and M. S. Wolfe, *Langmuir* **8**, 2382 (1992).
- [107] C. Chang and R. L. Powell, *J. Rheol.* **38**, 85 (1994).
- [108] T. Shikata, H. Niwa, and Y. Morishima, *J. Rheol.* **42**, 765 (1998).
- [109] R. A. Lionberger and W. B. Russel, *J. Rheol.* **38**, 1885 (1994).
- [110] R. Greenwood, P. F. Luckham, and T. Gregory, *J. Colloid Interface Sci.* **191**, 11 (1997).
- [111] N. J. Wagner and A. T. J. M. Woutersen, *J. Fluid Mech.* **278**, 267 (1994).
- [112] R. A. Lionberger, *Phys. Rev. E* **65**, 061408 (2002).
- [113] W. van Meegen and S. M. Underwood, *Nature* **362**, 616 (1993).
- [114] K. N. Pham, A. M. Puertas, J. Bergenholtz, S. U. Egelhaaf, A. Moussaïd, P. N. Pusey, A. B. Schofield, M. E. Cates, M. Fuchs,

- and W. C. K. Poon, *Science* **296**, 104 (2002).
- [115] J. V. Sanders, *Philos. Mag. A* **42**, 705 (1980).
- [116] M. D. Eldridge, P. A. Madden, P. N. Pusey, and P. Bartlett, *Mol. Phys.* **84**, 395 (1995).
- [117] T. Gruhn and P. A. Monson, *Phys. Rev. E* **64**, 061703 (2001).
- [118] G. Bryant, T. Mortensen, S. Henderson, S. Williams, and W. van Megen, *J. Colloid Interface Sci.* **216**, 401 (1999).
- [119] G. D. J. Phillis, *J. Chem. Phys.* **74**, 260 (1981).
- [120] K. Schätzel, M. Drewel, and J. Ahrens, *J. Phys.: Condens. Matter* **2**, SA393 (1990).
- [121] P. N. Segrè, W. van Megen, P. N. Pusey, K. Schätzel, and W. Peters, *J. Mod. Opt.* **42**, 1929 (1995).
- [122] E. Overbeck, C. Sinn, T. Palberg, and K. Schätzel, *Colloids Surf. A* **122**, 83 (1997).
- [123] C. Urban and P. Schurtenberger, *J. Colloid Interface Sci.* **207**, 150 (1998).
- [124] P. N. Pusey, *Curr. Opin. Colloid Interf. Sci.* **4**, 177 (1999).
- [125] W. van Megen, T. C. Mortensen, S. R. Williams, and J. Müller, *Phys. Rev. E* **58**, 6073 (1998).
- [126] C. W. J. Beenakker and P. Mazur, *Physica* **120A**, 388 (1983).
- [127] C. W. J. Beenakker and P. Mazur, *Physica* **126A**, 349 (1984).
- [128] G. Nägele and P. Baur, *Europhys. Lett.* **38**, 557 (1997).
- [129] M. Fuchs and M. R. Mayr, *Phys. Rev. E* **60**, 5742 (1999).
- [130] P. N. Segrè, O. P. Behrend, and P. N. Pusey, *Phys. Rev. E* **52**, 5070 (1995).
- [131] W. van Megen, S. M. Underwood, and P. N. Pusey, *Phys. Rev. Lett.* **67**, 1586 (1991).
- [132] A. M. Puertas, M. Fuchs, and M. E. Cates, *Phys. Rev. Lett.* **88**, 098301 (2002).
- [133] W. van Megen, S. M. Underwood, and P. N. Pusey, *J. Chem. Soc. Faraday Trans.* **87**, 395 (1991).
- [134] P. N. Pusey and W. van Megen, *Physica A* **157**, 705 (1989).
- [135] P. A. Irvine and J. W. Kennedy, *Macromolecules* **15**, 473 (1982).
- [136] R. L. Cotterman and J. M. Prausnitz, *Ind. Eng. Chem. Proc. Des. Dev.* **24**, 434 (1985).
- [137] S. K. Shibata, S. I. Sandler, and R. A. Behrens, *Chem. Eng. Sci.* **42**, 1977 (1987).
- [138] E. Bartsch, T. Eckert, C. Pies, and H. Sillescu, *J. Non-Cryst. Solids* **307–310**, 802 (2002).

- [139] T. Eckert and E. Bartsch, Phys. Rev. Lett. **89**, 125701 (2002).
- [140] T. Eckert and E. Bartsch, Faraday Discuss. **123** (2003), to be published.
- [141] W. Götze, J. Stat. Phys. **83**, 1183 (1996).
- [142] M. Abramowitz and I. A. Stegun, *Handbook of Mathematical Functions* (Dover, New York, 1970), 7th ed.
- [143] M. Enomoto and Y. Watatani, Math. Japonica **24**, 53 (1979).
- [144] D. R. Farenick, Proc. Am. Math. Soc. **124**, 3381 (1996).
- [145] N. F. Carnahan and K. E. Starling, J. Chem. Phys. **51**, 635 (1969).
- [146] A. Meyer (2002), cond-mat/0206364.
- [147] W. Paszkowicz, J. Phys. F **18**, 1761 (1988).